LUND UNIVERSITY

Charge Carrier Diffusion Induced Light Emitting Diodes

Adham, Kristi

2024

Document Version:
Publisher's PDF, also known as Version of record

Link to publication

Citation for published version (APA):
Adham, K. (2024). *Charge Carrier Diffusion Induced Light Emitting Diodes*. [Doctoral Thesis (compilation), Faculty of Engineering, LTH]. Department of Physics, Lund University.

Total number of authors:
1

LUND UNIVERSITY

PO Box 117
221 00 Lund
+46 46-222 00 00

Charge Carrier Diffusion Induced Light Emitting Diodes

KRISTI ADHAM
DEPARTMENT OF PHYSICS | FACULTY OF ENGINEERING | LUND UNIVERSITY

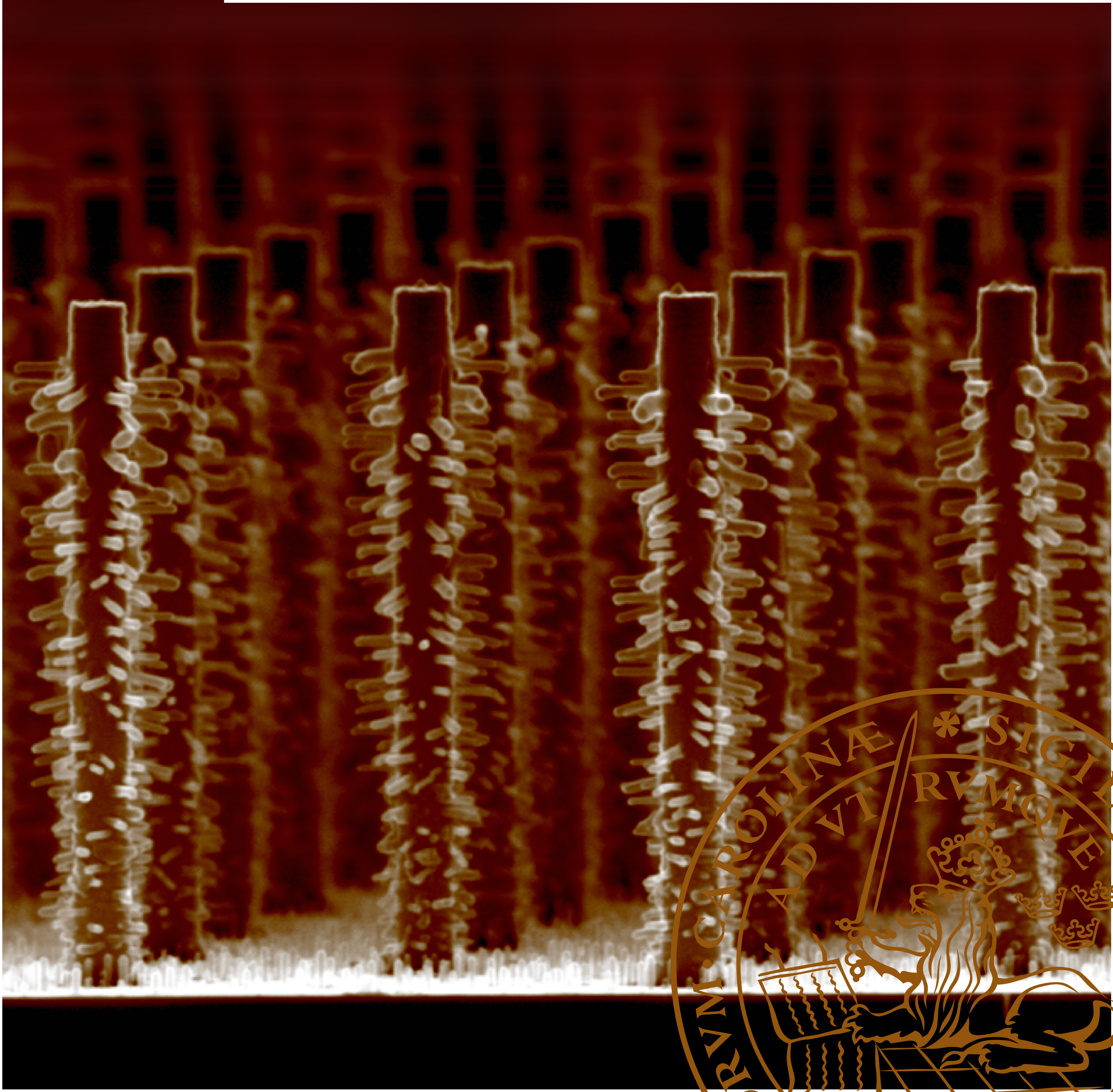

Charge Carrier Diffusion Induced Light Emitting Diodes

Charge Carrier Diffusion Induced Light Emitting Diodes

Kristi Adham

LUND
UNIVERSITY

DOCTORAL DISSERTATION

by due permission of the Faculty of Engineering, Lund University, Sweden.
To be defended on Friday September 13th, 2024, at 9:15 in Rydbergsalen,
Sölvegatan 14, Lund, for the degree of Doctor of Philosophy in Engineering.

Faculty opponent

Senior Scientist Jani Oksanen

Aalto University, Finland

Organization

LUND UNIVERSITY

Document name

DOCTORAL DISSERTATION

Date of issue September 13, 2024

Author: Kristi Adham

Sponsoring organization

Title: Charge Carrier Diffusion Induced Light Emitting Diodes

Abstract

Light emitting diodes (LEDs) have become the most efficient artificial lighting source. Their application is found in general indoor and outdoor lighting, headlights in automobiles, and displays whether it be TVs, laptops, mobile phones or smart watches. This technology is enabled by III-V semiconductors. Standard LEDs are comprised of stacked layers where the active region in the form of multi quantum wells is sandwiched between the n- and p-doped layers. This architecture however has several constraints such as a limited light extraction efficiency because of the presence of contact pads at the top and bottom of the structure, and it suffers from the phenomenon of total internal reflection.

To address these challenges, this thesis has presented a new architecture of LEDs implemented on nanowires. The structures resemble trees where the core nanowires of a high bandgap material provide the charge carriers, while the branches of a lower bandgap material act as the active region. Because of the difference in bandgap the carriers diffuse into the branches, where they recombine, and light is emitted. The dimension of the branches enables efficient light extraction overcoming total internal reflection.

In Paper I, the growth of nanotree structures is investigated by using a Au-containing solution to provide the seeds for branch growth. The successful growth of such structures is shown with a high density of branches.

In Paper II, the nanotree structures are processed into devices and a successful proof of concept of the diffusion of charge carriers from the cores to the branches is shown.

In Paper III, the structure is pushed one step further and doping is introduced in the branches and the devices are characterised to quantify its effect.

The platform opens up a new window into alternative architectures for LEDs, which promise a high efficiency and low processing cost.

Key words: Nanowire, MOVPE, III-V semiconductor, light-emitting diodes

Classification system and/or index terms (if any)

Supplementary bibliographical information

Language: English

ISSN and key title

ISBN

978-91-8039-968-5 (print)
978-91-8039-969-2 (pdf)

Recipient’s notes

Number of pages 107

Price

Security classification

Signature ______________________ Date September 13, 2024

Charge Carrier Diffusion Induced Light Emitting Diodes

Kristi Adham

LUND
UNIVERSITY

Front cover: Scanning electron microscope image of an array of nanotrees.

Division of Solid State Physics
Department of Physics
Lund University
SE-221 00 Lund
Sweden

ISBN 978-91-8039-968-5 (print)
ISBN 978-91-8039-969-2 (pdf)

Printed in Sweden by Media-Tryck, Lund University
Lund 2024

NORDIC SWAN ECOLABEL
Printed matter
3041 0903

Media-Tryck is a Nordic Swan Ecolabel
certified provider of printed material.
Read more about our environmental
work at www.mediatryck.lu.se

MADE IN SWEDEN

Kushtuar prindërve të mi dhe gruas sime!

Ju dua!

Table of Contents

Abstract iii

Acknowledgements v

Popular Science Summary vii

Populärvetenskaplig sammanfattning xi

Përmbledhje Popullore Shkencore xv

List of Publications xix

Abbreviations xxi

1 Introduction 1

2 Light Emitting Diodes 5

2.1 *pn* junction 6
2.2 Figures of Merit 11
2.3 Radiometry and Photometry 16
2.4 Diffusion Driven LEDs 19

3 Nanowire Synthesis 21

3.1 Substrate Patterning by Displacement Talbot Lithography 21
3.2 Metal Organic Vapor Phase Epitaxy 22
3.3 Electroless Deposition 26
3.4 Analysis of Nanowire Growth 32
3.5 Nanotree Structures 33

4 Processing and Characterisation of Nano-Tree LEDs 41

4.1 Device Fabrication 41
4.2 Electrical and Optical Characterisation 45
4.3 EQE, Radiometric & Photometric Characterisation 51

5 Conclusions and Outlook 61

References 63

Abstract

Light emitting diodes (LEDs) have become the most efficient artificial lighting source. Their application is found in general indoor and outdoor lighting, headlights in automobiles, and displays whether it be TVs, laptops, mobile phones or smart watches. This technology is enabled by III-V semiconductors. Standard LEDs are comprised of stacked layers where the active region in the form of multi quantum wells is sandwiched between the n- and p-doped layers. This architecture however has several constraints such as a limited light extraction efficiency because of the presence of contact pads at the top and bottom of the structure, and it suffers from the phenomenon of total internal reflection.

To address these challenges, this thesis has presented a new architecture of LEDs implemented on nanowires. The structures resemble trees where the core nanowires of a high bandgap material provide the charge carriers, while the branches of a lower bandgap material act as the active region. Because of the difference in bandgap the carriers diffuse into the branches, where they recombine, and light is emitted. The dimension of the branches enables efficient light extraction overcoming total internal reflection.

In Paper I, the growth of nanotree structures is investigated by using a Au-containing solution to provide the seeds for branch growth. The successful growth of such structures is shown with a high density of branches.

In Paper II, the nanotree structures are processed into devices and a successful proof of concept of the diffusion of charge carriers from the cores to the branches is shown.

In Paper III, the structure is pushed one step further and doping is introduced in the branches and the devices are characterised to quantify its effect.

The platform opens up a new window into alternative architectures for LEDs, which promise a high efficiency and low processing cost.

Acknowledgements

Reflecting on the past 5 years I am overcome with many thoughts and emotions. It definitely seems like a long time, but I swear it was one instant ago that I started this journey. And now it has come to its end. This journey is attributed to many people and events that have made possible me being here, and it is really difficult to pinpoint a unique moment that has made all this possible. Whenever someone asked me 12 years ago, when I was still in high school, where did I see myself in the future, circumstances made it difficult to imagine I would be where I am today, but I knew that I wanted a PhD in Physics.

First and foremost, I want to extend my deepest gratitude to my main supervisor, Magnus Borgström. Thank you for giving me the opportunity to be a part of your group, develop as a scientist and critical thinker over the past 5 years, and contribute to this exciting project. I appreciate how you always made time to meet with me and discuss the project and my endless questions. I can't recall a single time that I walked into your office and you said to come back later. You always came up with great ideas on new things to try in the lab, which motivated me to work even harder. I will always also cherish the fun conversations we had, about food, music, travel, and life in general. I also want to thank my co-supervisors Martin Magnusson and Knut Deppert. We always had interesting discussions and you provided valuable advice whenever I was banging my head against a wall.

I would like to thank the members of my group for all your help throughout the years. David, Lukas, and Enrique thank you for welcoming me into the group. To Matteo for being one of the most humorous people I know and for always making me smile even on a bad day. To Yue, I am very happy to have had you as the closest collaborator in this project. You always listened to me talk endlessly about research, new experiments, data analysis and LIFE. It has been relieving to have had someone to share the PhD burden with and you provided the best support. You are one of the best friends I've made. *Thank you for spilling wine on my carpet.* To Mariia, even though you just recently joined, we've had plenty of fun times and I wish you the best for your PhD. To Nils, for all the marvellous discussions about science, politics and economy.

I had the chance to inhabit two different offices during my 5 years. Thank you to Florinda, Elke, and David B. for providing a very warm, cosy, and fun working

environment. I remember walking the corridors of FTF a couple of weeks before joining and stumbled upon our office. There were so many posters from anime and Pokémon attached to the door that made me think “Wow this seems like an amazing office”, and what do you know, I ended up working there for 3 years and I was proven right.
To Marie and Asmita, the hosts of my new office, both of you have become best friends of mine and we have had so many amazing moments together that I can’t begin to count. Perhaps the best conversations will remain the ones we had about cars. I was very amused by the love and knowledge of automobiles you had and the endless discussions about which is best.

A special thanks to Andri! You can’t imagine what a pleasant surprise it was to have met you and become friends together. I now pass the torch of representing Albania at FTF to you!

The best for last, to Antti and Hossein. We have shared a lot together throughout these years, whether work, travelling, adventures, joyous moments, and not so joyous moments. I am very glad to have become best friends with you both. Talking about philosophy, series, not great not terrible events, our futures, and dreams. They were a constant source of motivation to be in my best mood every day.

To everyone else at FTF that made it a great workplace. I want to also thank the cleanroom staff for always being readily available to provide assistance.

To the many close friends that I have made throughout the years while living in shared corridor rooms in Belgium and Sweden. To Dhru, Joanna, Laura and Paula S. it’s been lovely getting to know you and I’m very happy that we still keep in touch and discuss our lives even after all these years. To Erik, Nahir, and Paula M. you made the time in Vildanden so memorable and enjoyable. From the evenings sitting in the kitchen and talking about everything, to the stargazing nights and all the crazy parties we had. To Lina, for being the first Swedish friend I made and all the amusing times we have spent.

I want to thank Adi, Aldo, Armela, Brikena, Ervin, Ildia, Klaudio, Pirro and Xhejms for always keeping in touch with me. It was an opportunity to feel close to home, have a fun time and discuss a myriad of topics.

I want to thank my uncle and his wife, whose contribution to my journey is of great importance to me. I will always carry in my heart the help you have given me. I am eternally grateful.

Lastly, I want to thank my parents and my wife, for being a constant source of support, encouragement and never failing to believe in me.

Popular Science Summary

Two good old friends of humanity throughout the millennia have been the oil lamp and the candle, utilised to provide artificial lighting. The utilisation of candles is so deeply connected to our perception of light that even the SI unit of the luminous intensity is named after the Latin word for candle: candela (cd). Luminous intensity is the amount of luminous power per unit solid angle emitted in a particular direction, and as the name suggests, the luminous intensity of a wax candle is about 1 cd. This amount of light is certainly too little to light our houses and streets.

In our highly industrialised world, one can only imagine what it was like to stare at the night sky several hundred or thousand years ago. A multitude of glimmering stars lighting up the night sky. Our ancestors who only had two means of lighting, the sun during the day and manmade fire at night to provide warmth and protect against the unexcepted perils of the wilderness, were certainly astonished at such sights. Nowadays it is necessary to travel to a remote location with little light pollution to enjoy the stars. That is indeed correct, we now produce so much artificial lighting that it has earned its own category of pollution. But how did we go from pitch-black nights to very bright ones? With the advancement of industry and after Edison improved the lifetime of the incandescent light bulb, high-brightness sources became accessible, and their inclusion in our everyday life ever more present.

The field of general lighting experienced many other great feats in the 20th century. Among different types of sources, one can highlight mercury vapour lamps for street lighting, neon lamp signs, metal halide lamps for indoor and outdoor lighting, high- and low-pressure sodium vapour lamps for outdoor lighting, halogen lamps, and fluorescent lamps. However, the biggest and most important advancement of the 20th century for lighting came from the semiconductor revolution. Apart from enabling the myriad of technologies that we utilise today, it opened a new door in the general lighting market. Many III-V semiconductors, a subset of semiconductors made of chemical elements from groups III and V of the chemical table, have the property to emit light once a potential difference is applied to them. III-V semiconductors can emit a specific colour if they are in a binary compound, but one can also form ternary or quaternary alloys to tune the emitted colour. These semiconductors have enabled the invention of light emitting diodes (LEDs). Compared to other sources, LEDs are more environmentally friendly as they contain no mercury, have high efficiency, have a very long lifetime on the order of tens of thousands of hours, offer the possibility of colour tunability, and compact size.

The immediate danger of climate change has enabled us to focus our attention on more sustainable and efficient sources of energy production. But how much energy is used and for what purpose is also important. Lighting contributes to roughly 20% of the global electricity usage and will keep increasing in the coming decades. Phasing out alternative lighting methods like incandescent light bulbs which waste most of the input power by outputting heat and making LED fixtures the common technology in every lighting market will contribute to a more sustainable energy usage.

Conventional LEDs are made of structures called thin films, where several materials are stacked on top of each other, each with a specific purpose. There are the layers which provide the charge carriers, the active region layers where the charge carriers recombine and emit light and the blocking layers that confine the carriers and impede them from escaping the active region. This method of stacking poses restrictions on the degrees of freedom that one has to design the active region, as it is constricted by the dimensions of the layers underneath and above it. The colour emitted from the LED is determined by the type of material used in the active region. Although the LEDs currently on the market provide high efficiency, it does not come without a caveat. In conventional LEDs, the interface between the active region and the environment imposes an important boundary condition on the light extraction efficiency because of the discontinuity of the refractive index. A semiconductor has a typical refractive index of 3 while that of air is 1. According to Snell's refraction law, this restricts the light extraction up to a critical angle, above which the light is trapped inside the semiconductor. To improve the extraction efficiency many costly tricks are performed.

In this thesis, in contrast to thin films, I have used very small structures called nanowires, which are cylindrical structures with a diameter of roughly 150 nm (about 300 times thinner than a strand of hair) and a length of 2 µm to make LEDs. My work has been focused on an alternative LED architecture and overcoming total internal reflection. Nanowires provide an excellent platform to address both challenges. The primary material that I have focused on is the ternary gallium indium phosphide (GaInP) which has a tuneable emission from infrared to green depending on the content of Ga and In in the material. I have designed structures resembling trees (Figure 1), where the branches play the role of the active region and carriers are injected into the branches by means of diffusion. Having a diameter on the order of 10-50 nm, light generated inside the branches can be completely extracted from the semiconductor without suffering from total internal reflection.

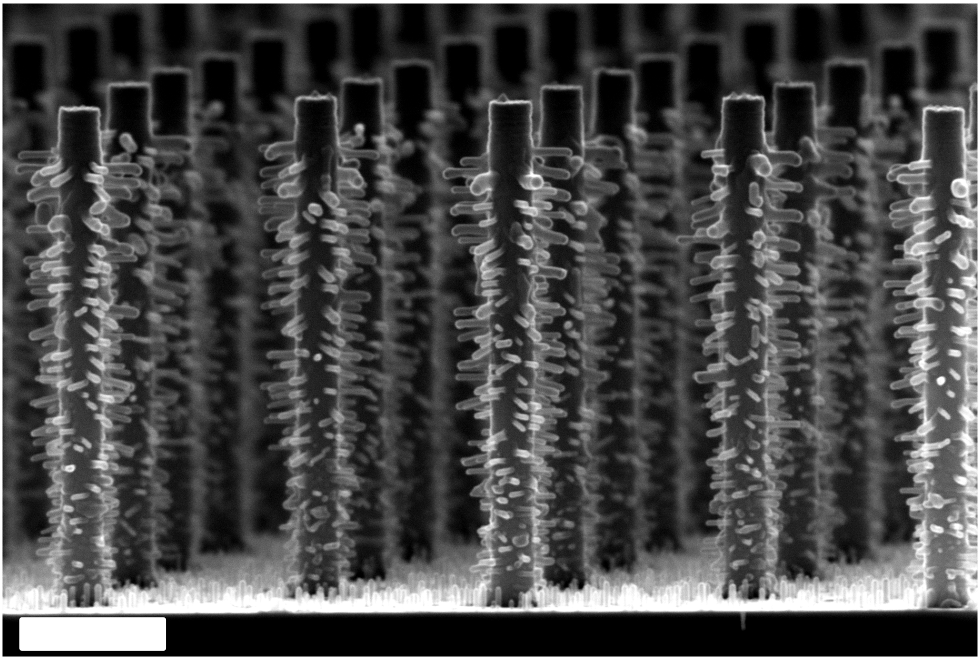

Figure 1: A scanning electron microscope image of the nanotree array. The scale bar is 500 nm.

I have worked both on the fabrication of the tree structures and the characterisation of the LEDs. One starts from a bare substrate, defines a regular array of gold particles and grows the GaInP stems with the assistance of the gold particles. A second round of gold particles is deposited to grow the GaInP branches. Because they are so small, to observe the structures instead of light microscopes we make use of scanning & transmission electron microscopes. Processing steps in the cleanroom are undertaken to convert the grown structures into functional LED devices. In Figure 2, you can see a picture of myself, dressed in protective garments prior to some chemical work in one of the many processing steps.

Lastly, the LEDs are characterised and I have measured their emission spectrum, radiation pattern and efficiency. Thousands of nanotrees are connected in parallel in a full device. The LEDs made in this work can be tuned to emit bright white light, creating a pathway for solid state white LEDs based solely on semiconductors.

Figure 2: A picture of myself in the cleanroom, dressed in protective garments to perform chemical work.

Populärvetenskaplig sammanfattning

Två av mänsklighetens gamla vänner genom årtusendena har varit oljelampan och stearinljuset, som används för att ge artificiell belysning. Användningen av ljus är så djupt kopplad till vårt samhälle att även SI-enheten för ljusstyrka är uppkallad efter det latinska ordet för ljus: candela (cd). Ljusstyrka är mängden ljusstyrka per rymdvinkelsenhet som avges i en viss riktning, och som namnet antyder är ljusstyrkan för ett vaxljus cirka 1 cd. Denna mängd ljus är otillräcklig för att lysa upp våra hus och gator.

I vår högt industrialiserade värld kan man bara föreställa sig hur det var att stirra på natthimlen för flera hundra eller tusen år sedan. En mängd glittrande stjärnor som lyser upp natthimlen. Våra förfäder hade bara två ljuskällor: solen under dagen och den konstgjorda elden på natten för att ge värme och skydda mot vildmarkens oförutsedda faror, blev verkligen förvånad av natthimlen. Nuförtiden är det nödvändigt att resa till en avlägsen plats med lite ljusföroreningar för att kunna njuta av stjärnorna. Vi producerar nu så mycket artificiell belysning att den har fått sin egen kategori av förorening. Men hur gick vi från becksvarta nätter till ljusa? Med industriella framsteg och efter att Edison förbättrade livslängden för glödlampan, blev källor med hög ljusstyrka tillgängliga, och deras inkludering i vårt vardagliga liv blev allt mer närvarande.

Användandet av allmänbelysning avancerade under 1900-talet. Bland olika typer av ljuskällor kan kvicksilverånglampor för gatubelysning, neonlampor skyltar, metallhalogenlampor för inomhus- och utomhusbelysning, hög- och lågtrycksnatriumånglampor för utomhusbelysning, halogenlampor och lysrör nämnas. 1900-talets största och viktigaste framsteg för belysning kom genom halvledarerevolutionen. Förutom att möjliggöra den myriad av teknologier som vi använder idag, öppnade den en ny dörr på marknaden för allmänbelysning. Många III-V-halvledare, en undergrupp av halvledare gjorda av kemiska element från grupperna III och V i den kemiska tabellen, har egenskapen att avge ljus när en spänning läggs på dem. Dessa typer av halvledare har möjliggjort uppfinningen av ljusemitterande dioder (LED). Jämfört med andra källor är lysdioder mer miljövänliga eftersom de inte innehåller något kvicksilver, har hög verkningsgrad, mycket lång, erbjuder möjlighet till färgjustering, och kompakt storlek.

Den omedelbara faran med klimatförändringar har gjort det möjligt för oss att fokusera på mer hållbara och effektiva källor för energiproduktion. Men hur mycket energi som går åt och till vilket syfte är också viktigt. Belysning bidrar till ungefär 20% av den globala elanvändningen och den kommer att fortsätta öka under de kommande decennierna. Att fasa ut ineffektiva belysningsmetoder som glödlamporna och göra LED-armaturer till den vanliga tekniken på varje belysningsmarknad kommer att bidra till en mer hållbar energianvändning.

Konventionella lysdioder är gjorda av strukturer baserade på lager av olika material som odlats ovanpå varandra. Det finns skikten som tillhandahåller laddningsbärarna, de aktiva regionskikten där laddningsbärarna rekombinerar och avger ljus och blockerande skikt för att begränsa bärarna och hindra dem från att fly det aktiva området. Denna staplingsmetod innebär begränsningar i hur man kan designa den aktiva regionen med avseende på lagren under och ovanför den. Färgen som avges från lysdioden bestäms av typen av material som används i det aktiva området. Även om de lysdioder som för närvarande finns på marknaden ger hög effektivitet, kommer det inte utan ett problem. En halvledare har ett typiskt brytningsindex på 3 medan det för luft är 1. Detta begränsar ljusextraktionen till en kritisk vinkel enligt Snells brytningslag, bortom vilken ljuset fångas inuti halvledaren. För att förbättra ljusemission används många kostsamma knep i dagens industriella tillverkning.

I den här avhandlingen har jag, till skillnad från tunna filmer, använt mycket små strukturer som kallas nanotrådar, som är cylindriska strukturer med en diameter på ungefär 150 nm (cirka 300 gånger tunnare än ett hårstrå) och en längd på 2 μm för att göra en ny sort av lysdioder. Mitt arbete har varit fokuserat på en alternativ LED-arkitektur och att övervinna total intern reflektion. Nanotrådar är en utmärkt plattform för att möta båda utmaningarna. Det primära materialet som jag har fokuserat på är den ternära galliumindiumfosfiden (GaInP) som kan emittera från infraröd till grön beroende av sammansättningen av Ga och In i materialet. Jag har designat strukturer som liknar träd (Figur 1), där grenarna spelar är den aktiva regionen och ström injiceras i grenarna med hjälp av diffusion. Med en diameter i storleksordningen 10-50 nm kan ljus som skapas inuti grenarna inte fångas i materialet och total intern reflektion elimineras.

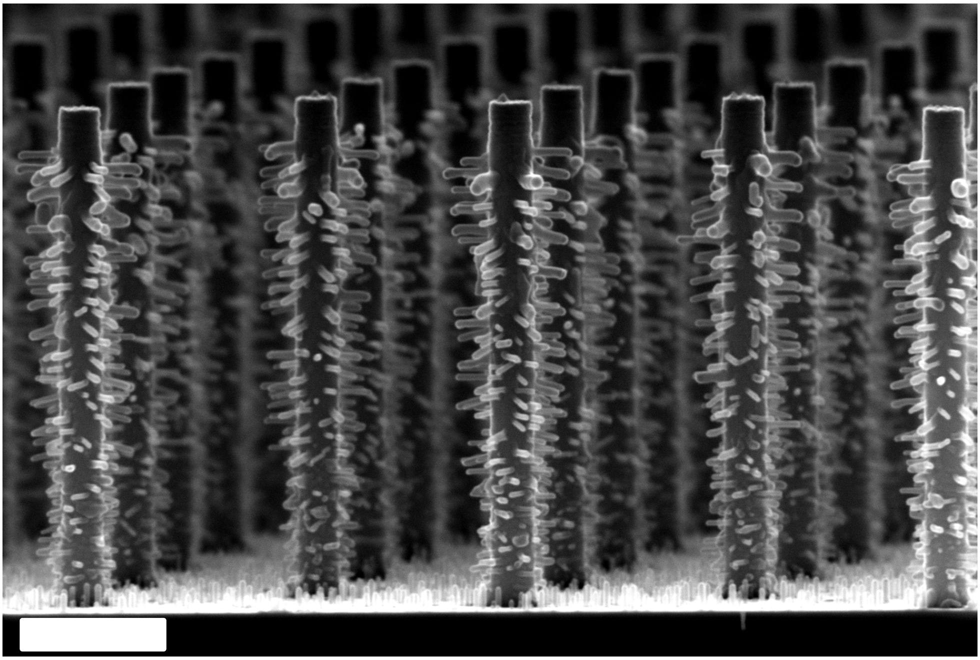

Figur 1: En svepelektronmikroskopbild av nanoträden. Skalstången är 500 nm.

Jag har arbetat både med tillverkningen av trädstrukturerna och karakteriseringen av lysdioderna. Man utgår från ett substrat, definierar en regelbunden samling av guldpartiklar och odlar GaInP-stammarna med hjälp av partikelassisterad odling. En andra omgång av guldpartiklar deponeras sedan på stammarna för att kunna odla GaInP-grenarna. Eftersom de är så små använder vi svep- och transmissionselektronmikroskop för att observera strukturerna istället för ljusmikroskop. För att fabricera funktionella LED-enheter utförs bearbetning i renrummet. I figur 2 kan du se en bild på mig, klädd i skyddskläder inför kemiskt arbete i ett av de många bearbetningsstegen.

Slutligen är lysdioderna karakteriserade och jag har mätt deras emissionsspektrum, strålningsmönster och verkningsgrad. Tusentals nanoträd är parallellkopplade i en ljusdiod. Ljusdioderna som tillverkas i det här arbetet kan ställas in för att avge vitt ljus, vilket skapar en väg för vita lysdioder baserade enbart på halvledare.

Figur 2: En bild på mig själv i renrummet, klädd i skyddskläder för att utföra kemiskt arbete.

Përmbledhje Popullore Shkencore

Dy miq të mirë të njerëzimit, gjatë mijëvjeçarëve, kanë qënë llamba e vajgurit dhe qiriu, të përdorur për të përftuar ndriçim artificial. Përdorimi i qirinjve është i lidhur kaq thellësisht me perceptimin tonë të dritës, saqë dhe njësia SI për intensitetin ndriçues është e emërtuar pas fjalës Latine për qiriun: candela (cd). Intensiteti ndriçues është sasia e fuqisë ndriçuese e emetuar për njësi këndi të ngurtë në një drejtim të caktuar, dhe siç kuptohet nga emërtimi, intensiteti ndriçues i një qiriu është rreth 1 cd. Kjo sasi drite është pa dyshim mjaft e ulët për të ndriçuar shtëpitë dhe rrugët tona.

Në botën tonë tejet të industrializuar, mundet vetëm të imagjinojmë se si mund të ketë qënë të vështroje qiellin gjatë natës, disa qindra, ose mijëra vjet më parë. Një mizëri yjesh të shndërritshëm që ndriçonin qiellin. Paraardhësit tanë, të cilët kishin vetëm dy mënyra ndriçimi: atë të diellit gjatë ditës dhe zjarrin gjatë natës, i cili ofronte gjithashtu edhe ngrohtësi dhe mbrotje ndaj rreziqeve të paparashikuara, padyshim ishin të mahnitur ndaj pamjeve të tilla. Në ditët e sotme, është e nevojshme të udhëtohet në vende të izoluara, me pak ndotje dritore për të shijuar yjet. Është e vërtetë, ne tashmë prodhojmë aq shumë ndriçim artificial, saqë ka fituar kategorinë e vet të ndotjes. Por si shkuam nga netë tërërisht të errëta në mjaft të ndritshme? Me zhvillimin e industrisë, si dhe pasi Edisoni përmirësoi jetëgjatësinë e llambës inkandeshente, burimet me ndriçim të lartë u bënë lehtësisht të gjendshme, dhe përfshirja e tyre në përditshmërinë tonë, gjithnjë e më e pranishme.

Lëmia e ndriçimit të përgjithshëm kaloi bëma të tjera të mëdha gjatë shekullit të 20-të. Midis burimeve të ndryshme mund të përmendim llambat me avull mërkuri për ndriçimin e rrugëve, llambat e neonit për tabelat dhe reklamat, llambat me halid metali për ndriçim të brendshëm dhe të jashtëm, llambat me avull natriumi me shtypje të ulët dhe të lartë për ndriçim të jashtëm, llambat halogjene dhe llambat fluoreshente. Por përparimi më i madh dhe më i rendësishëm i shekullit të 20-të për ndriçimin erdhi nga revolucioni i gjysmëpërçuesve. Përveç se mundësoi shumëllojshmërinë e teknologjive që përdorim në ditët e sotme, hapi një portë të re në tregun e ndriçimit të përgjithshëm. Shume gjysmëpërçues III-V, një nënklasë e gjysmëpërçuesve të përbërë nga elementë kimikë të grupit të III dhe V të tabelës së Mendelejevit, kanë veçorinë që të emetojnë dritë kur aplikohet një diferencë potenciale. Gjysmëpërçuesit III-V mund të emetojnë një ngjyrë specifike në qoftë se përbërja është binare, por gjithashtu ngjyra mund të akordohet duke formuar aliazhe treshe ose katërshe. Këto lloje gjysmëpërçuesish kanë mundësuar shpikjen e diodave që emetojnë dritë (diodat LED). Në krahasim me burimet e tjera, diodat LED janë më miqësore për mjedisin pasi nuk përmbajnë mërkur, kanë rendiment të lartë, jetëgjatësi mjaft të gjatë në rendin e dhjetëra mijëra orëve, ofrojnë mundësinë e akordimit të ngjyrës, dhe kanë madhësi kompakte.

Rreziku i menjëhershëm i ndryshimeve klimatike, na ka mundësuar të përqëndrojmë vëmendjen tonë në burime të prodhimit të energjisë që janë më të qëndrueshme dhe efikase. Por si përdoret kjo energji dhe për çfarë qëllimi ka gjithashtu rendësi. Ndriçimi përbën 20% të përdorimit botëror të elektricitetit dhe do vazhdojë të rritet në dekadat e ardhshme. Heqja graduale e metodave alternative të ndriçimit, si llambat inkandeshente të cilat e harxhojnë fuqinë hyrëse duke e çliruar atë si nxehtësi, dhe kthimi i pajisjeve LED në teknologjinë standarde në çdo treg ndriçimi, do të kontribuojë në përdorimin e një enegjie më të qëndrueshme.

Diodat tradicionale LED përbëhen nga struktura të quajtura filma të hollë, ku një sërë materialesh janë të vendosur sipër njëri tjetrit, secili me një qëllim të caktuar. Një LED përbëhet nga shtresat që ofrojnë ngarkesat elektrike, shtresat e zonës aktive (ku ngarkesat rikombinohen për të përftuar dritë) dhe shtresat bllokuese (për të kufizuar ngarkesat dhe penguar ato që të largohen nga zona aktive). Kjo metodë mbivendosjeje limiton gradët e lirisë në dizenjimin e zonës aktive, pasi është e kufizuar nga dimensionet e shtresave poshtë dhe sipër saj. Ngjyra e emetuar nga dioda LED përcaktohet nga lloji i materialit të përdorur në zonën aktive. Edhe pse diodat LED që gjenden momentalisht në treg kanë një rendiment të lartë, ky rendiment nuk vjen pa një disavantazh. Në diodat e zakonshme LED, ndërfaqja midis zonës aktive dhe mjedisit të jashtëm, vendos një kushtëzim të rendësishëm në efikasistetin e nxjerres së dritës, për shkak të pavazhdueshmërisë së treguesit të përthyerjes. Një gjysmëpërçues ka një tregues përthyerje zakonisht rreth 3 kurse treguesi i ajrit është 1. Kjo gjë kufizon nxjerrjen e dritës deri në një kënd kritik, sipas ligjit të përthyerjes së Snellit, për vlera mbi të cilin drita mbetet e bllokuar brenda gjysmëpërçuesit. Për të përmirësuar efikasitetin e nxjerrjes kryhen mjaft hile të kushtueshme.

Në këtë tezë, në krahasim me filmat e hollë, unë kam punuar me struktura mjaft të vogla të quajtura nanofije, të cilat janë struktura cilindrike me një diametër përafërsisht 150 nm (rreth 300 herë më të holla se një fije floku) dhe një gjatësi prej 2 µm, për të prodhuar diodat LED. Puna ime ka qënë e përqëndruar në një arkitekturë alternative për diodat LED, si dhe tejkalimin e pasqyrimit të plotë të brendshëm. Nanofijet mundësojnë një platformë të shkëlqyer për t'iu drejtuar të dyja këtyre sfidave. Materiali kryesor në të cilin jam përqëndruar është kombinimi tresh fosfat kallaj galiumi (GaInP) i cili ka një emetim të ndryshueshëm nga infra të kuqe në jeshile në varësi të sasisë së Ga dhe In në material. Kam dizenjuar struktura që u ngjasojnë pemëve (Figura 1), ku degët luajnë rolin e zonës aktive dhe ngarkesat injektohen në degë nëpërmjet difuzionit. Duke patur një diametër të rendit të 10-50 nm, drita e prodhuar brenda degëve mund të nxirret tërësisht jashtë gjysmëpërçuesit pa u kushtëzuar nga pasqyrimi i plotë i brendshëm.

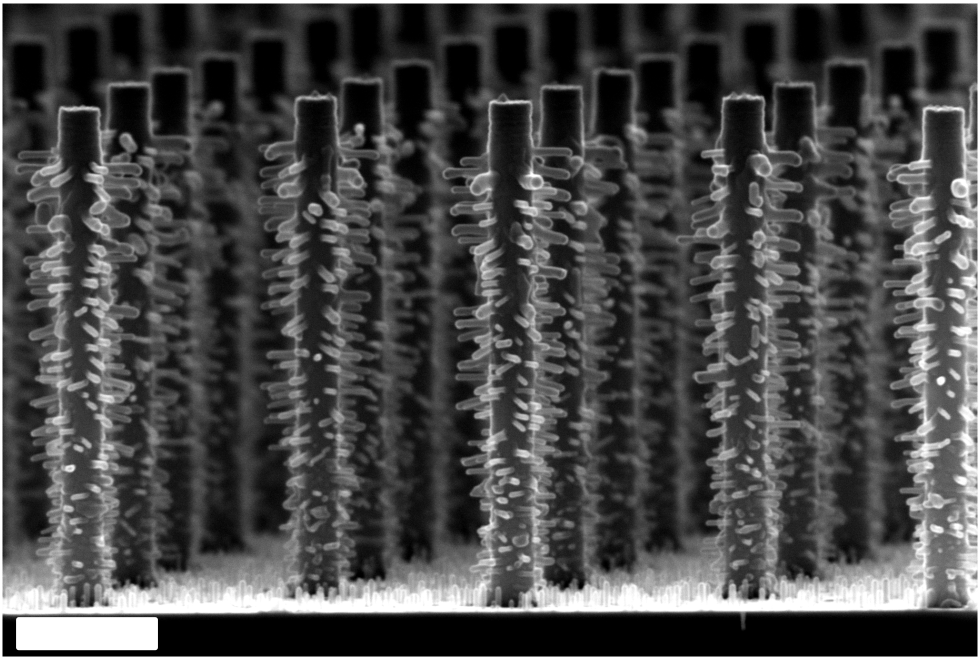

Figura 1: Një imazh me mikroskop elektronik i arradhës së nanopemëve. Shkalla është 500 nm.

Unë kam punuar si në prodhimin e strukturave të nanopemëve, ashtu edhe në karakterizimin e diodave LED. Fillohet nga një substrat i pastër, më pas përcaktohet një arradhë e rregullt me grimca ari, dhe rriten trungjet prej GaInP me ndihmesën e grimcave të arit. Më pas depozitohet një raund i dytë grimcash ari për të rritur degët prej GaInP. Për të vështruar strukturat, për shkak se janë aq të vogla, në vend të mikroskopëve me dritë, përdorim mikroskopë me elektrone të llojit skanimi dhe transmetimi. Për të shndërruar më pas strukturat e rritura në pajisje funksionale LED, ndërmerren hapa përpunimi në dhomën e pastër. Në Figurën 2, mund të shihni një foto timen, të veshur me rroba mbrojtëse përpara se të kryej punë kimike në një prej hapave të shumtë të përpunimit.

Së fundmi, diodat LED karakterizohen dhe kam matur spektrin e tyre të rrezatimit, veçoritë e rrezatimit në drejtime të ndryshme dhe rendimentin e tyre. Mijëra nanopemë janë të lidhura në paralel në një mostër. Diodat e prodhuara në këtë punë, mund të akordohen që të emetojnë dritë të shndërritshme të bardhë, duke i hapur rrugë krijimit të diodave LED që emetojnë dritë të bardhë të bazuara vetëm në gjysmëpërçues.

Figura 2: Një fotografi e imja në dhomën e pastër, i veshur me rroba mbrojtëse për të kryer punë kimike.

List of Publications

I. **Growth of branched nanowires via solution-based Au seed particle deposition**

K. Adham, Y. Zhao, L. Hrachowina, D. Alcer, R. Wallenberg, and M. T. Borgström

Materials Research Express **2023**, 10 (8), 085003

I synthesised the nanowires, planned and carried out the Au deposition experiments, and synthesised the branches. I analysed the data and I was the main responsible for writing the paper.

II. **Direct band gap white light emission from charge carrier diffusion induced nanowire light-emitting diodes**

Y. Zhao*, K. Adham*, D. Hessman, and M. T. Borgström

*These authors have contributed equally to this work

(Manuscript Submitted)

I jointly planned the experiments. I shared responsibility for the synthesis of the nanotrees and the fabrication of the devices and I measured the electroluminescence spectra and radiation pattern. I performed the integrating sphere measurements to evaluate the efficiency of the devices. I have analysed the data, participated in the discussion of the results and wrote part of the paper.

III. **Characterization of n-doped branches in nanotree LEDs**

K. Adham, Y. Zhao, P. Kivisaari, and M. T. Borgström

(Manuscript Submitted)

I planned the experiments, synthesised the nanotrees, fabricated the devices and measured the electroluminescence spectra, and carried out the temperature dependent measurements. I performed the integrating sphere measurements to evaluate the efficiency of the devices. I have analysed the data, participated in the discussion of the results and I was responsible for writing the paper.

Publications not included

The following publications are not included because they are considered to be outside the scope of this thesis:

IV. **Spectrally Tunable Broadband Gate-All-Around InAsP/InP Quantum Discs-in-Nanowire Array Phototransistors with a High Gain-Bandwidth Product**

H. Jeddi, B. Witzigmann, K. Adham, L. Hrachowina, M. T. Borgström, and H. Pettersson

ACS Photonics **2023**, 10, 6, 1748-1755

V. **Enhanced LWIR response of InP/InAsP quantum discs-in-nanowire array photodetectors by photogating and ultra-thin ITO contacts**

H. Jeddi, K. Adham, Y. Zhao, B. Witzigmann, F. Römer, M. Bermeo, M. T. Borgström, and H. Pettersson

Nanotechnology **2024**, 35, 215206

VI. **Accessing the Phonon Dispersion of Nanowires**

V. G. Hinojosa, I. Mediavilla, K. Adham, Y. Zhao, A. H. Romero, L. Wirtz, A. Bosak, M. T. Borgström, D. A. Chaney, and J. Serrano

(Manuscript in Writing)

Abbreviations

Al	aluminium
Al_2O_3	sapphire
ALD	atomic layer deposition
AlGaInP	aluminium gallium indium phosphide
AlN	aluminium nitride
AR	augmented reality
ArF	argon fluoride
AsH_3	arsine
Au	gold
BOE	buffered oxide etch
C_2H_5	ethyl
CAD	computer-aided design
CCDI	charge carrier diffusion induced
CCT	correlated colour temperature
CH_3	methyl
CMOS	complementary metal-oxide-semiconductor
CRI	colour rendering index
Cu	copper
DEZn	diethylzinc
DHJ	double heterojunction
DI H_2O	deionised water
DIL	dual in-line
DTL	Displacement Talbot Lithography
DUT	device under test
EDX	energy dispersive X-ray spectroscopy
EL	electroluminescence
EQE	external quantum efficiency
GaAs	gallium arsenide
GaAsP	gallium arsenide phosphide
GaInP	gallium indium phosphide
GaInN	gallium indium nitride
GaN	gallium nitride
GaP	gallium phosphide
H_2	hydrogen

H_2S	hydrogen sulphide
$HAuCl_4$	chloroauric acid
HCl	hydrochloric acid
In	indium
In_2O_3	indium trioxide
InAsSb	indium arsenide antimonide
InP	indium phosphide
IQE	internal quantum efficiency
IR	infrared
ITO	indium tin oxide
KI	potassium iodide
LED	light emitting diode
µLED	micro light emitting diode
OLED	organic light emitting diode
LEE	light extraction efficiency
MFC	mass flow controller
Mg	magnesium
MO	metal-organic
MOVPE	metal-organic vapour phase epitaxy
NW	nanowire
P	phosphorus
P_2O_5	phosphorus pentoxide
pc-wLED	phosphor-converted white LED
PCB	printed circuit board
PH_3	phosphine
QD	quantum dot
MQW	multi quantum well
RIE	reactive ion etching
SEM	scanning electron microscope
Si	silicon
SiC	silicon carbide
SiO_x	silicon oxide
SiO_2	silicon dioxide
SMU	source measure unit
SRH	Shockley-Read-Hall
SSL	solid state lighting
TEGa	triethylgallium
TEM	transmission electron microscope
TESn	tetraethyltin
Ti	titanium
TMAl	trimethylaluminium
TMIn	trimethylindium

TTBS	tri(tert-butoxy)silanol
UV	ultraviolet
VLS	vapour-liquid-solid
VR	virtual reality
WZ	wurtzite
XRD	X-ray diffraction
ZB	zincblende

1 Introduction

捧げよ！捧げよ！心臓を捧げよ！
全ての犠牲は今この瞬間の為に！
人類を栄光あれ！

Global warming has become the most pressing issue to tackle, affecting the lives of everyone on Earth and further progress and innovation is necessary if we intend to still be around in the foreseeable future. The use of finite resources such as fossil fuels (natural gas, coal) as the main source of energy worldwide has put our livelihoods in danger with their harmful impact on the environment [1]. An important stepping stone to phase out the usage of fossil fuels and address climate change is the Paris Agreement of 2016, which aims to limit the average global temperature to a 2 °C increase compared to pre-industrial levels [2]. Thus, the search for more efficient energy sources and the reduction of our carbon footprint is of utmost importance. Semiconductor technology developed in the last 80 years is an important foundation in overcoming this challenge [3]. Research and development has been carried out in the area of power generation, with efforts being directed to advance technology and utilise renewable sources such as solar power using solar panels and wind power using wind turbines.

On the other hand, apart from power generation, we are also faced with the search for new solutions to reduce our daily power consumption. Lighting, which is a big part of all of our lives in all its various forms, accounts for about ~20% of the total electricity usage and it is expected to increase even further in the coming decade, contributing substantially to our emissions [4, 5]. The history of the lighting industry has experienced great leaps of advancements, going from candles to oil lamps to incandescent bulbs to fluorescent bulbs and currently to solid state lighting (SSL) represented by light emitting diodes (LEDs). Compared to all the previous technologies, LEDs are the most efficient ones since the light emission is accompanied by very little heat loss, while incandescent bulbs lose about 90% of their energy consumption in the form of heat [6, 7]. Figure 1.1 illustrates a visual comparison of the luminous efficacy between an incandescent light bulb, a fluorescent one and an LED. The EU has made great strides in giving companies and researchers further motivation to advance LEDs. Several milestones can be noted, such as: the 2012 ban on incandescent bulbs, the 2021 new guidelines on LED efficiency, where the most efficient LEDs on the market at the time, were downgraded to only a C ranking, and the 2023 ban on fluorescent lighting. The effects of such regulations are already noticeable. Signify (former Philips), the world leader in lighting, has already released on the market white LEDs with an efficacy of 210 lm/W, fulfilling the new A-ranking efficiency requirement of the guideline [8]. In the last 10 years, Nobel Prizes in Physics and Chemistry, namely the one in 2014 and 2023 have been awarded to LEDs and materials that enable such devices. The first one was given to the invention of the blue LED, an invention which revolutionised the field in the 1990s, and the second prize was given to quantum dots (QDs). The application of LEDs on the other hand is not limited to general lighting only. The landscape of applications includes backlighting in displays, signalling, horticulture, and self-emissive displays. With the advent of micro LEDs (µLEDs), which is an up-and-coming technology due to its many advantages [9-11], augmented reality/virtual reality (AR/VR) applications have also received a lot of attention.

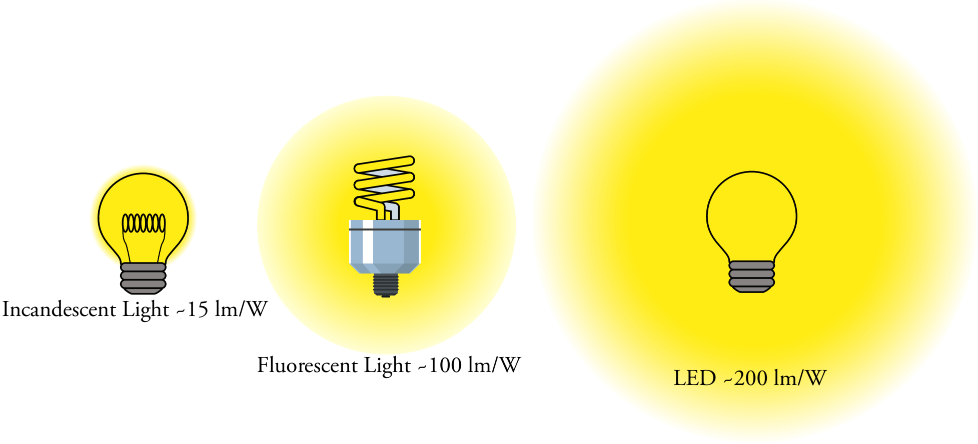

Figure 1.1: A comparison of the luminous efficacy between three different types of light sources. An incandescent light bulb (*left)* has an efficacy of approximately 15 lm/W, a fluorescent light bulb (*centre)* has an efficacy of about 100 lm/W and record LEDs (*right)* that can be found on the market have an efficacy of around 200 lm/W. The yellow halo surrounding each light source provides a visual representation of their luminous efficacy.

The most abundant and widely used semiconductor, silicon (Si), while being the cornerstone of the field of electronics, is not an adequate material to act as an LED due to its indirect bandgap and that its bandgap of 1.1 eV is not within the visible spectrum [12]. The field of III-V semiconductors (semiconductors which are made of elements from the groups III-A and V-A of the chemical table), with material combinations such as aluminium gallium indium phosphide (AlGaInP), gallium phosphide (GaP), gallium nitride (GaN) and gallium indium nitride (GaInN), has revolutionised the field of SSL [13-15]. On the other hand, the benefits of III-V semiconductors come with the disadvantage of high material costs since the wafer comprises most of the LED's device volume while the active region is only a fraction of it. A Si substrate would be the cheapest solution to the problem, but the differences in lattice constant and thermal expansion coefficient between Si and the III-V materials lead to the formation of defects at the interface which reduces the efficiency of the device. The most commonly used substrates to grow GaInN materials nowadays are sapphire (Al_2O_3) and silicon carbide (SiC), even though there is a large lattice mismatch between GaInN and the chosen substrate [16].

Nanowires (NWs), a geometry with a high aspect ratio where the length is at least one order of magnitude higher than the diameter, have been under intense research over the last 20 years [17-41]. This geometry holds great promise in the field of photonics and optoelectronics and has become attractive to the field of SSL. The development of NW growth has shown that they grow preferentially along the ⟨111⟩B direction and substrates of the same crystal direction are used to grow vertical NWs. Efforts have been made to integrate NWs with Si for electronic applications, by growing them on Si(111) substrates. By employing different techniques, such as selective area growth, vertical NWs have been grown on Si(100),(110) and (112) [42, 43]. For display applications, Si would be the desirable substrate of choice to grow these structures on, in order to reduce costs and because of the complementary metal-oxide-semiconductor (CMOS) compatibility [9].

In this thesis, an alternative architecture for making LEDs is being pursued. III-V NWs have demonstrated the potential to develop tandem junction solar cells [39, 44], as well as having applications in the field of photodetectors [45-47] and LEDs [48-51]. Due to their small footprint, these structures can also be grown on substrates where a large lattice mismatch occurs due to their effective radial strain relaxation [52, 53]. Compared to planar structures, NWs are also advantageous because they consume less source material without suffering a loss in efficiency. In vertical chip µLEDs, the grown thin film needs to be etched to form individual pixels. NWs offer a potential solution as another advantage of NW lies in the fact that one does not etch the structures to form the µLEDs and thus avoids side wall damage, which decreases the efficiency of the structures.

The bulk of this thesis is focused on realising LEDs using the novel concept of charge carrier diffusion induced (CCDI) injection. Compared to the standard planar LEDs, we have aimed to adopt the novel CCDI LED concept, developed at Aalto University. Their work [54] is focused on thin film structures where the active region of the LED is grown on top of a *pn* junction. When a potential difference is applied, the carriers are injected into the active region by bi-polar diffusion where they recombine and emit light. We have adopted this concept in NW structures. In the work presented here, the NWs are being grown in a tree-like structure. In this structure, at first core *pin* NWs are grown, which have a certain bandgap depending on the material composition that is grown. Afterwards, on the sidewalls of the NWs, branches of a semiconductor material with a lower bandgap are grown. The branches, with a lower bandgap than the core, play the role of the active region. Upon applying a bias, the charge carriers can be injected into the branches by diffusion due to the bandgap difference. In the branches, the charge carriers can then be efficiently recombined and emit light.

To pave the way for such a work, we first studied the growth of indium phosphide (InP) branches on InP core NWs. This material combination although the simplest, allowed us to study the parameter space for branch growth. We developed, characterised, and took control over depositing particles along the NWs' length by using a gold (Au)-containing solution, which enables the branch growth. By varying different parameters during the deposition, we obtained an estimation of the limitations of branch growth, their density, length, diameter, and distribution. The continuation of the work was followed by the ternary system gallium indium phosphide (GaInP). In the ternary material, the bandgap can be controlled by changing the atomic percentage of Ga and In. We grew GaInP NWs with a large bandgap and subsequently grew InP and GaInP branches of different compositions. We successfully showed operational LEDs with two distinctive peaks coming from the cores and the branches. In our latest study, we have introduced doping in the branches and characterised the new structures.

The thesis is structured as follows:

Chapter 2 introduces the physics of the *pn* junction, the field of LEDs, its figures of merit and the motivation for this work.

Chapter 3 introduces substrate patterning, NW growth, NW sidewall decoration with Au particles to grow the branches and the results from InP-InP core-branch growth.

Chapter 4 describes the processing steps to go from as-grown NWs to ready-to-measure devices. The LEDs grown and characterised are of GaInP-GaInP core-branch composition. The main results of the LED structures are presented such as their emission spectrum, radiation pattern and efficiency.

Chapter 5 summarises the work done in the thesis and provides an outlook on the future of these structures as a potential new LED architecture.

2 Light Emitting Diodes

> *It is often said that men are ruled by their imaginations; but it would be truer to say they are governed by the weakness of their imaginations.*
> *– Walter Bagehot*

The beginning of the LED journey can be traced back to Henry Round in 1907 [55], when he was experimenting with SiC detectors and noticed that the SiC crystal was emitting light when passing current through it [56]. The first detailed investigation of the electroluminescence process in SiC was carried out in 1923 by Oleg Losev [57, 58]. The invention of III-V semiconductors brought a lot of attention due to their property of being optically very active. In the 1950s, the infrared (IR) LED was demonstrated, together with the first visible LED made of GaP [59]. The next important step in the evolution of the field was the invention of alloy semiconductors such as ternary structures where one combines three different materials to form the semiconductor, examples of which, among others, are gallium arsenide phosphide (GaAsP), and GaInP [60]. This opened up the possibility of colour tuning by changing the alloy composition. The last piece of the puzzle was the invention of an efficient blue source.

By the 1980s, green and red LEDs were already well established, but blue LEDs were facing problems, which inhibited the mixing of all 3 primary colours to make white light. This challenge was overcome at the end of the 1980s by Amano, who realised the first operational p-doped GaN with magnesium (Mg) as a dopant, together with the first blue LED based on a *pn* GaN [61]. With the existence of the three primary colours now available, white sources can be made, albeit the market adoption of white sources has mostly relied on phosphor-converted white LEDs (pc-wLED). This technology relies on utilising a phosphor which absorbs high-energy photons and emits photons in the visible spectrum. One can distinguish between two types of pc-wLED: the first kind utilises a material emitting in the ultraviolet (UV). A phosphor material absorbs the UV light and emits a broad spectrum from blue to red. The second kind starts from a material which emits in the blue, usually GaN or InGaN and a yellow phosphor. The yellow phosphor absorbs the blue light and converts it into yellow, the combination of both is then perceived as white by our eyes. In these kinds of LEDs, there is always some loss in efficiency due to the conversion of photons from a higher to a lower energy, named Stokes shift [55, 62]. Another option as mentioned above, and the preferable one for the future of the industry is the combination of elemental blue, green and red to produce white light and various combinations within the visible spectrum [63, 64]. Figure 2.1 illustrates the three types of combinations to achieve white light. The utilisation of the three primary colours, although preferable, has been held back for a long time. Firstly, because of what is known as the green gap, where green LEDs suffer from lower efficiencies compared to red and blue. In 2014 and later in 2018, Osram published significant advancements in the efficiency of green LEDs with efficacies up to 307 lm/W [65], substantially reducing the green gap. Secondly, efficient red LEDs are made in AlGaInP instead of GaN which increases the complexity of integrating it into a single lamp or display.

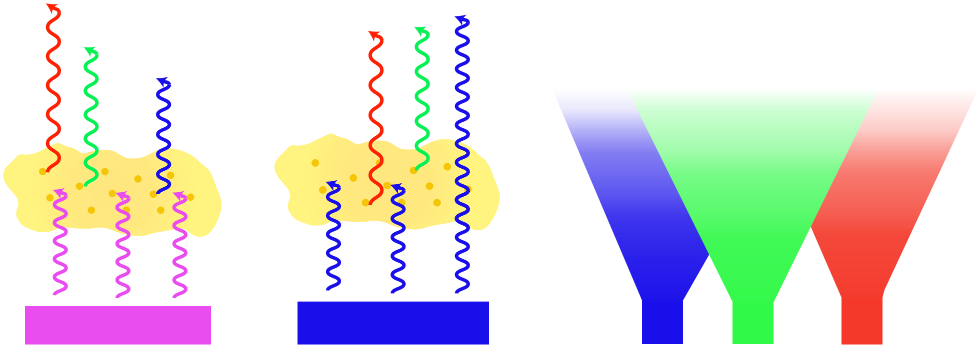

Figure 2.1: Three different kinds of structures that can be used to produce white light. The first two kinds are by utilising pc-wLEDs, either by producing UV light which is absorbed by a phosphor material and down converted to white light (*left*), or by producing blue light which is partially absorbed by a phosphor and down converted to yellow light (*centre*). The third kind is to use elemental blue, green and red LEDs, the mixture of which is perceived as white (*right*).

The first part of this chapter has provided a short historical development of the field of LEDs. However, there has still not been a description as to what is a semiconductor and an LED. How does it work? What is doping and the *pn* junction and why are they important? How does one define and calculate quantities like the efficiency, radiant power, luminous power, radiance, and luminance? The following sections will provide a description of these keywords, their importance and how they are calculated.

2.1 *pn* junction

In this section, some of the fundamental properties of a semiconductor that are relevant to this thesis will be discussed. Semiconductors, which form the infrastructure of the electronics industry, can be found in a broad range of devices that we use in our daily lives, such as LEDs, cameras, TVs, and computer chips among others [66]. A semiconductor has properties which lie in the range between a conductor like copper (Cu) and an insulator like silicon dioxide (SiO_2). The property used in literature to differentiate between these three types of materials is either the conductivity of the material or the bandgap, the energy difference between the valence and conduction band. In a metal this energy difference is zero, and the bands overlap, while in an insulator the energy difference is on the order of above 4 eV [67, 68]. The bandgap energy for semiconductors varies from around 0.1 eV in indium arsenide antimonide (InAsSb), all the way up to 6.2 eV in aluminium nitride (AlN), making it possible to excite carriers from the valence to the conduction band by means of light, thermal energy or by applying an electric field. When an electron gets excited from the valence band to an empty state in the conduction band, it will create a vacancy in the valence band which behaves as a positively charged particle, named a hole. To calculate the statistical distribution of charge carriers in a semiconductor in equilibrium, the Fermi energy and Fermi statistics come into play. In a semiconductor, the Fermi level is defined as the energy position with an occupation probability of an electron of 50%. In an intrinsic semiconductor, which has not been manipulated in any way to create a charge imbalance in it, this level lies close to the middle of the bandgap. An intrinsic semiconductor is not very interesting for applications. One would like to be able to alter the properties of the material, such as the conductivity, which in practice is done by a process called doping. By doping a semiconductor, one alters the charge carrier concentration. The dopants are atomic impurities which are added to the material. Depending on the dopant that is added, it can have more or fewer electrons than the starting semiconductor, thereby either increasing the number of free electrons or holes. When the density of electrons or holes is tuned, the Fermi level shifts closer to the conduction or valence band, respectively. If a dopant contributes by adding free electrons to the material it is known as a donor, and the material is called n-doped, while if the dopant increases the hole concentration it is known as an acceptor and the material is p-doped. In Figure 2.2 the three different types of semiconductors are shown along with the Fermi level.

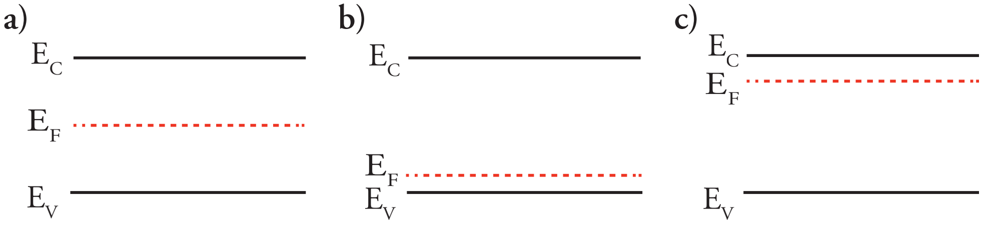

Figure 2.2: a) An intrinsic semiconductor with the Fermi level located close to the middle of the bandgap. b) A p-type semiconductor with the Fermi level located close to the valence band energy level. c) An n-type semiconductor with the Fermi level located close to the conduction band energy level.

We now turn our attention to the combination of a p- and n-doped semiconductor which forms the basis of a diode and consequentially of an LED [69]. By combining these two types of semiconductors, we form a metallurgical junction between them. Once the junction is formed, the electrons from the n-region will diffuse towards the p-region and holes will diffuse towards the n-region. The diffusion of carriers leaves behind positively charged donor atoms and negatively charged acceptor atoms in the n- and p-region, respectively. This charge accumulation on both ends leads to the formation of an electric field, also called the built-in field and the region is called depletion region (W) since no mobile carriers are found in it. A variation of the *pn* junction is the *pin* junction, where between the p- and n-region, an intrinsic region is also made. The intrinsic region changes the width of the depletion region and the strength of the built-in electric field. Figure 2.3 shows a *pn* and *pin* junction with their respective depletion regions highlighted.

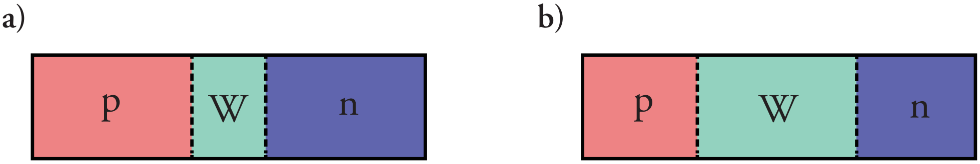

Figure 2.3: a) A semiconductor *pn* junction. b) A semiconductor *pin* junction with a wider depletion region W.

The discussion until now has assumed that the diode is in equilibrium, i.e., no external bias is applied. It is instructive to provide a treatment of a biased diode. One can distinguish between two cases, by applying a forward or a reverse bias to the junction. Below, we will discuss the case of forward biasing a *pn* junction. To facilitate the discussion, two band diagrams are shown in Figure 2.4, for the junction under equilibrium, and under forward bias. Without any externally applied bias and in thermal equilibrium, the Fermi level along the structure is at the same energy, which creates a bending of the conduction and valence band, since the conduction and valence bands have a different distance to the Fermi level in the regions. The conduction band in the p-segment is higher than in the n-segment (Figure 2.4 (a)), which the electrons see as a potential barrier they cannot get over, which is called the built-in potential (V_{bi}). The built-in potential depends on the bandgap of the p- and n-region as well as the respective doping levels.

On the other hand, once a potential difference is applied between the p- and n-regions, the system is no longer in equilibrium and the Fermi level is no longer constant. What happens during an applied bias is a splitting of the Fermi level and the appearance of quasi-Fermi levels, E_{Fn} and E_{Fp} for electrons and holes respectively, the difference of which is equal to the applied bias (V) (Figure 2.4 (b)). In the case of forward biasing, the applied potential difference reduces the band bending in the system. The decrease of the potential barrier also leads to the reduction of the depletion region, making it easier for electrons to diffuse in the p-region and holes to diffuse in the n-region.

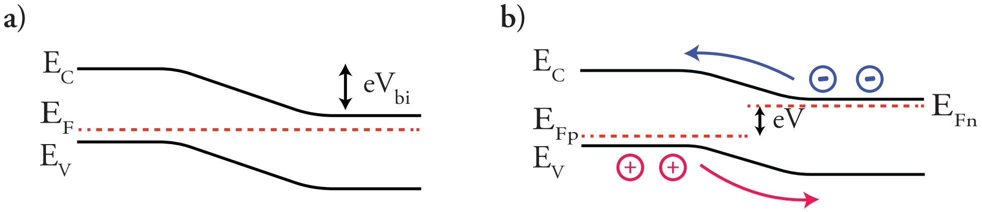

Figure 2.4: a) A *pn* junction in equilibrium with the built-in energy highlighted as eV_{bi}. b) A *pn* junction under forward bias. The applied bias decreases the built-in energy by eV and facilitates the flow of electrons and holes.

A major application of the *pn* junction is the LED. In principle, the idea of an LED is the same as forward biasing a *pn* junction. When a positive potential difference is applied, the injected carriers recombine with each other. This recombination between electrons and holes leads to light generation, the colour of which depends on the bandgap of the semiconductor material. Even though the principle is straightforward, not every semiconductor material can be used as an LED. What makes the difference and limits the available options of choice is the type of bandgap of the semiconductor. The bandgap of a semiconductor can be divided into two categories: indirect and direct bandgap. In an indirect bandgap, the maximum of the valence band and the minimum of the conduction band are separated by a momentum difference, while in direct bandgap materials, they are aligned (see Figure 2.5).

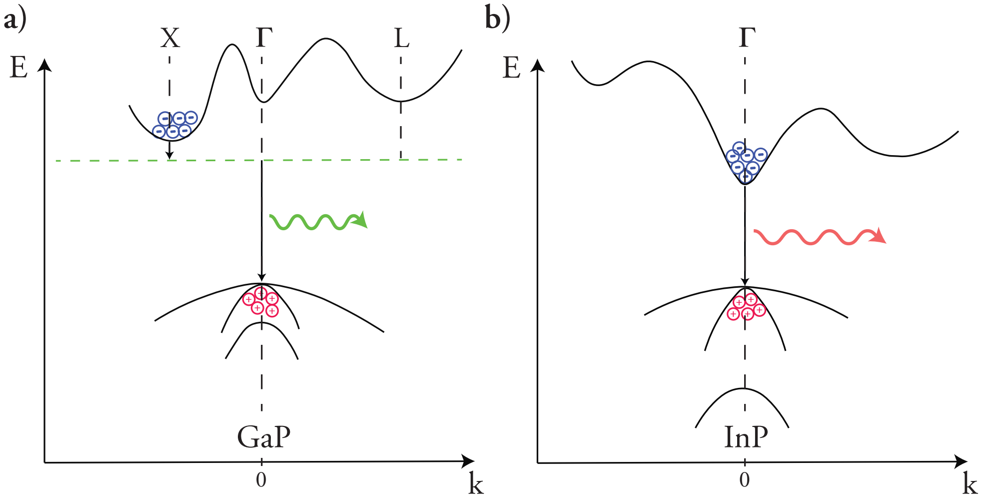

Figure 2.5: a) The band structure of GaP is depicted, which is an indirect semiconductor. The bottom of the conduction band and the top of the valence band are not aligned, and a phonon is needed as an intermediate particle to enable an electron-hole recombination. b) The band structure of InP, which is a direct bandgap material, where an electron and hole can easily recombine and emit a photon. The x-axis represents momentum (k) and y-axis energy. Γ, X and L represent the different valleys.

Photons cannot be efficiently generated in indirect bandgap materials because an interaction with a phonon is also needed to fulfil the conservation of momentum requirement. On the other hand, in direct bandgap semiconductors the electron and hole recombine under the same momentum and no phonon is required, making the light emission process more efficient [70]. This is also the reason why LEDs emit light with very little heat generation. If we take the most widely used semiconductor in industry, Si, it has an indirect bandgap and cannot be used to emit light efficiently, but a recent breakthrough has made it possible to have a direct bandgap of SiGe alloy by modifying the crystal structure from cubic to hexagonal in NW structures [71].

A homojunction LED which consists of the same material both in the n- and p-region does not produce the highest efficiency as the generated photons can be reabsorbed by the semiconductor. To increase the efficiency, the double heterojunction (DHJ) was developed. In this structure, the n- and p-region comprise of a high bandgap material, and the active layer, made of a lower bandgap material, is sandwiched in-between. The active layer is generally composed of multiple nominally intrinsic quantum wells (MQW). By using a DHJ, one creates potential barriers for the carriers such that they can be confined in the active region and recombine efficiently. Another advantage of the structure is that the light is no longer absorbed by the wide bandgap material since the emitted light has an energy smaller than its bandgap.

Apart from the desired recombination of electrons and holes to produce light, other mechanisms are also involved which decrease this efficiency. Three recombination mechanisms take place in a semiconductor which can be separated into radiative and nonradiative recombination. During radiative recombination, as already mentioned, an electron and hole produce a photon upon recombination, while in nonradiative recombination such as Shockley-Read-Hall (SRH) or Auger recombination, heat is produced instead. The SRH mechanism involves the recombination of an electron or hole with an impurity energy level located within the bandgap. This impurity level could be created from defects, or from the impurities introduced to dope the material. The Auger recombination is a three-particle interaction mechanism. Once a recombination event occurs, the energy released is immediately absorbed by another electron or hole, which is sent into a higher energy state. To make an efficient LED the radiative recombination needs to be maximised. A general formula of the total recombination rate can be written as [72, 73]:

$$R = R_{\mathrm{SRH}} + R_{\mathrm{Rad}} + R_{\mathrm{Aug}} = \left(\frac{A}{n + p + 2n_{\mathrm{i}}} + B + C(n + p)\right)(np - n_{\mathrm{i}}^2) \qquad (2.1)$$

where R_{SRH} is the SRH recombination rate, R_{Rad} is the radiative recombination rate, R_{Aug} is the Auger recombination rate, and A, B, and C are recombination constants. In Figure 2.6 the various recombination possibilities in a semiconductor are shown.

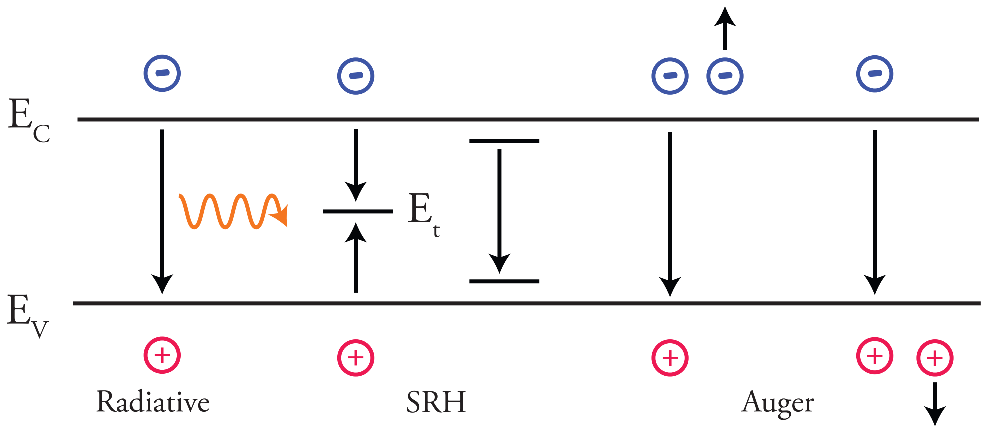

Figure 2.6: Various recombination processes in a semiconductor. Radiative recombination of an electron from the conduction band with a hole in the valence band which leads to a photon emission. SRH recombination of an electron and a hole to a deep trap level, or between a donor and an acceptor state. Auger recombination, where the energy released from an electron-hole recombination is transferred either to another electron or hole.

2.2 Figures of Merit

In the previous section, we established the inner workings and mechanisms that lead to light emission. Although one would want only radiative recombination to occur in an LED, the existence of defects, be they inside the crystal or at its surface, leads to having a combination of both radiative and nonradiative processes occurring simultaneously during the operation of the LED. In this section and the next, we are going to make use of the fact that we are not working with an ideal behaviour and utilise it to define and describe how an LED is quantified and how we extract the useful quantities which are also commonly found in the product descriptions.

Output spectrum

The first characteristic that one looks at in an LED is the emission spectrum. It provides information on whether the LED is a single colour and the wavelength of emission, or if it is a broadband emission and how much each part of the spectrum contributes to the total light output. Figure 2.7 shows the spectrum of a commercial green LED strip (a) and of white light emission of an organic LED (OLED) display found on mobile phones (b).

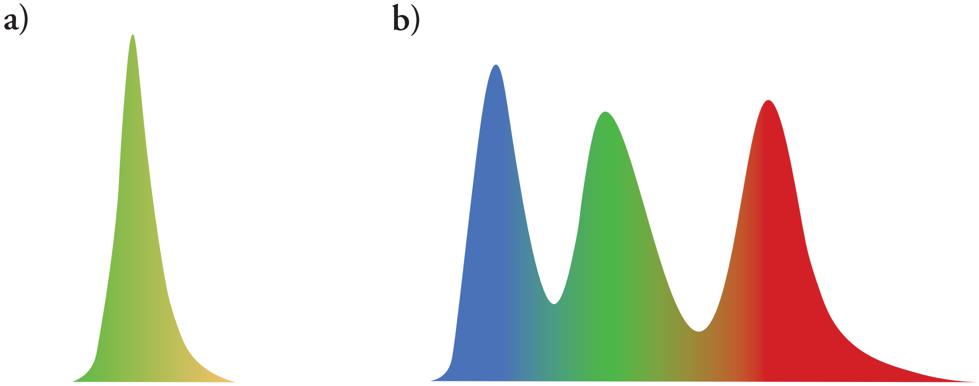

Figure 2.7: a) Emission spectrum of a commercial green LED strip light from waveform lighting [74]. b) White emission spectrum from a display found on commercial mobile phones.

The straightforward way of thinking about light emission is that the energy of the emitted photon is the same as that of the bandgap, but this is not the whole story as the electrons (holes) are not located at the bottom (top) of the conduction (valence) band but have a distribution in energy [75].

There can be a recombination event where the electron and hole energy are close to the bandgap energy, or a slightly energetic electron recombines with a hole and vice versa. These processes contribute to the emission energy being different from the bandgap energy. The spontaneous emission rate has the form [69]:

$$I(\nu) \propto \nu^2 (h\nu - E_g)^{\frac{1}{2}} \exp\left(-\frac{h\nu - E_g}{kT}\right) \tag{2.2}$$

where $h\nu$ is the photon energy, E_g is the material bandgap, k is the Boltzmann constant, and T is the operating temperature.

Internal quantum efficiency

Considering that not all the injected carriers contribute to light emission, we can define the internal quantum efficiency (IQE) as the number of injected carriers that lead to luminescence. The quantity is a product of the injection efficiency, which is the ratio of the electron current with the total injected current, and the radiative efficiency, which is the number of radiative recombination events compared to the total recombination events. Depending on the material system, different IQE levels can be achieved. Blue GaN can achieve a very high IQE, on the order of 90% [76, 77], while phosphor materials have an IQE which generally reaches up to 70% [78]. It can be written in formula form as [55]:

$$IQE = \frac{J_n}{J_n + J_p + J_{Rec}}\left(\frac{R_r}{R_r + R_{nr}}\right) = \frac{\frac{P_{internal}}{h\nu}}{\frac{I}{e}} \tag{2.3}$$

where J_n, J_p, and J_{Rec}, are the electron, hole and recombination current, respectively, R_r, and R_{nr} are the radiative and nonradiative recombination rates, $P_{internal}$ is the internal power generated in the LED per second, $h\nu$ is the photon energy, I is the injected current and e is the electron charge.

Light escape cone

Every material is characterised by an intrinsic property which is the index of refraction. The index of refraction determines the degree of light bending towards or away from the normal of the plane when light crosses over the boundary of two mediums with different refractive indices, such as semiconductor-air. III-V semiconductors tend to have a high refractive index [79], and this leads to a limited amount of light being emitted from LEDs. Based on Snell's law:

$$n_1 \sin\theta_1 = n_2 \sin\theta_2 \tag{2.4}$$

light traversing from a high refractive index medium n_1 to a lower one n_2, is refracted away from the normal of the plane and can only do so up to a critical angle, after which $\theta_2 = 90°$ and the light is completely reflected, giving the name total internal reflection. Since air has $n_2 = 1$, then $\theta_{crit} = \arcsin(1/n_1)$. In practical devices, this gives rise to an escape cone and since the emitted photons have random directions, only the portion emitted within this cone contributes to illumination. Figure 2.8 shows the total reflection of a light ray and the highlighted escape cone. Considering the small emission angle obtained because of the high refractive index difference between the semiconductor and air, the emitted power is approximately given by:

$$\frac{P_{out}}{P_{internal}} \approx \frac{1}{4}\theta_{crit}^2 \approx \frac{1}{4}\frac{n_2^2}{n_1^2} \tag{2.5}$$

where P_{out} is the power emitted in air. Taking as an example the standard GaN blue LEDs, a material which has a refractive index of about 2.5, the ratio in equation 2.5 becomes 1/25, or in other words 96% of the generated light remains trapped in the GaN.

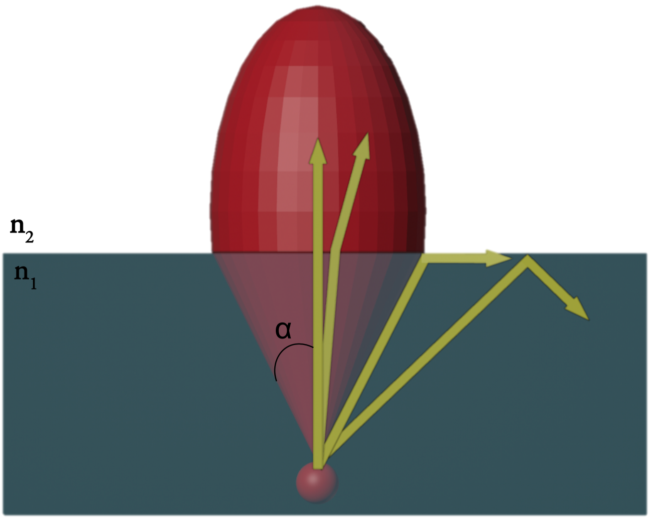

Figure 2.8: A point source inside the semiconductor emitting light. The yellow arrows indicate the light path and the refraction at the semiconductor-air interface. After the critical angle (α), total internal reflection occurs, defining an escape cone, depicted in red.

Various methods have been used to enhance the light extraction efficiency (LEE), such as changing the shape of the LED to spherical or conical [80, 81], applying antireflection coatings [82], photonic crystals [83-85], pentagon structure [86], metallic gratings [87-90]. In NWs, this limitation can be completely overcome. Theoretical simulations have shown that as the NW diameter decreases, light extraction improves, due to the electric field leaking out from the NW. Once the diameter is thin enough (~50 nm and below), the generated light gets completely extracted [91].

External quantum efficiency

Apart from the light being generated in the active region, it needs to be extracted from the semiconductor. This makes for a very important parameter in any LED device: the external quantum efficiency (EQE), which is the ratio of the number of photons emitted per second with the number of injected carriers in the structure. It represents the fraction of generated light which is emitted from the device and can be written as [75]:

$$EQE = IQE \cdot LEE = \frac{\frac{P_{\mathrm{LED}}}{h\nu}}{\frac{I}{e}} \tag{2.6}$$

where P_{LED} is the emitted power per second from the LED. The main reasons that the internal and external efficiencies differ from each other are attributed to several loss mechanisms such as reabsorption in the structure, reflection losses and total internal reflection.

Materials

LEDs can be constructed from a wide range of materials. It can be separated into the categories of organic materials represented by OLEDs and inorganic materials such as III-V semiconductors and perovskites. OLEDs have become a very mature technology and have received wide range adoption in the market over the last decade with TVs and mobile phone screens receiving the highest integration [92-94]. The most used materials however in the realm of inorganic materials are III-V semiconductors. This combination of materials is about crystals formed with chemical elements from groups III and V of the periodic table. In Figure 2.9, a plot of the different III-V material combinations and their respective lattice constant and bandgap energy is shown. The solid or dashed black lines connecting two different binary materials show that the ternary combination of them has a direct or indirect bandgap, respectively. Focusing on the material combination used in this work, the combination of InP and GaP is connected with a black line up to ~70% Ga [95, 96]. For Ga content higher than this, going up to pure GaP, there is a $\Gamma - \mathrm{X}$ transition and the bandgap becomes indirect, even though the latter has been used to make green LEDs by use of alloying with N, or by altering the crystal structure from zincblende (ZB) to wurtzite (WZ) in NW form leading to direct bandgap GaP [97-99].

To determine and tune the bandgap and lattice constant of a ternary material, we make use of Vegard's law, in equations 2.7 and 2.8, in which the lattice constant/bandgap depends on the lattice constants and atomic percentages of the binaries.

$$a_{Ga_xIn_{1-x}P} = x \cdot a_{GaP} + (1-x) \cdot a_{InP} \tag{2.7}$$

$$E_{g_{Ga_xIn_{1-x}P}} = x \cdot E_{g_{GaP}} + (1-x) \cdot E_{g_{InP}} \tag{2.8}$$

Apart from ternary materials, quaternary combinations can also be produced. In such a structure, one can independently vary the lattice constant and bandgap of the material, allowing one to achieve lattice matched structures and tune the wavelength of emission. One such example is AlGaInP [100], which is an industry standard for making red LEDs, lattice matched to gallium arsenide (GaAs) substrates [101, 102].

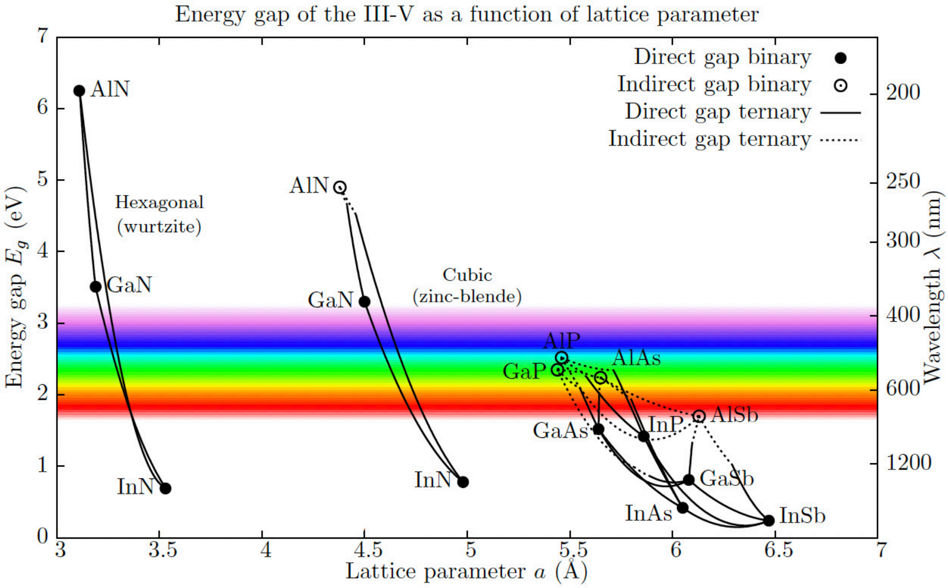

Figure 2.9: III-V semiconductor bandgap energy and their respective lattice parameter. The plot shows binary III-Vs which have either a direct bandgap (solid dots) or an indirect bandgap (hollow dots). The lines, either solid or dashed, connecting two binary compositions indicate a ternary combination which has a direct or an indirect bandgap, respectively. Figure reproduced with permission from [103]. License: ©2013, Miguel Ángel Caro Bayo - http://creativecommons.org/licenses/by-nc-nd/3.0/.

2.3 Radiometry and Photometry

We have covered the fundamentals of evaluating quantities like the IQE and EQE, but there are many more parameters that one looks for in an LED. Although deeply connected to IQE and EQE, when one searches an LED datasheet, these values are rarely what is reported. Instead, the power consumption in Watts (W), the power emitted by the light source in lumen (lm), correlated colour temperature (CCT) and colour rendering index (CRI) are reported. CCT is a parameter found in labels of white LED sources. It describes the temperature a black body would have, were it to emit light with the same chromaticity as the white LED source. The CRI of a white source describes the ability of the source to reproduce accurately the colours of an illuminated source such that they appear natural. CRI is calculated in comparison to a reference source. For sources with a CCT below 5000 K, a Planckian radiator is used as a reference with the same CCT as the source [104].

This section will describe the important quantities that are necessary for an in-depth understanding of a light source [105]. Depending on the intended application a certain range of values is desired. We begin with the description of radiometric quantities.

These parameters study a source based on the amount of optical radiation emitted. To aid in the visualisation of the concepts the reader is referred to Figure 2.10 (a)-(d).

(a) The first parameter is the radiant power (Φ). This quantity describes the amount of energy emitted per unit time in every direction by a light source and it is measured in W.

(b) The second quantity is the radiant intensity (I). It describes the amount of radiant power that passes through a unit of solid angle in a certain direction and it is measured in Watts per steradian (W/sr).

The last two quantities are radiance and irradiance. The nomenclature can sometimes be slightly confusing, so it is important to understand the difference between the two.

(c) Radiance (R) is a property of the emitting source. It describes the amount of radiant power emitted from a source with an elementary area dA which propagates through a solid angle $d\Omega$ in a given direction and forms an angle θ with the area dA. The definition can be related to the radiant intensity since $dI = d\Phi/d\Omega$, and in the case of a Lambertian emitter where the radiant intensity has a cosine dependence, the radiance is constant independent of the viewing angle. The unit of radiance is $W/sr{\cdot}m^2$.

(d) Irradiance (E) on the other hand is the amount of radiant power that falls on a surface with area A and is measured in W/m^2. Traditionally irradiance was often called intensity, but it is no longer used.

Radiometric quantities describe any emitting source irrespective of the emission wavelength. The human eye on the other hand is not capable of probing the entire electromagnetic spectrum. We can detect a very small portion, namely between 380 to 700 nm. Furthermore, the sensitivity of our eyes is not uniform across the visible spectrum. Our eyes are most sensitive in the green, with the peak sensitivity at 555 nm. Photometry is a subcategory of radiometry where one characterises a source with respect to the responsivity of our eyes. In analogy to the four quantities described above for radiometry, there are four photometric quantities, namely: luminous flux measured in lm, luminous intensity measured in candela (cd), luminance measured in cd/sr, and illuminance measured in lm/m^2. The conversion between radiometric and photometric quantities is done by the eye responsivity function V_λ and the factor $K = 683$ lm/W, which is the maximum value of V_λ at 555 nm. Table 2.1 provides a summary of the radiometric and photometric quantities, and equation 2.9 shows a formula for converting a radiometric quantity to a photometric one.

$$\alpha = K \int_{380\,nm}^{700\,nm} \beta(\lambda) V_{\lambda}(\lambda) d\lambda \tag{2.9}$$

where α represents any photometric quantity and $\beta(\lambda)$ represents the spectral component of the analogous radiometric quantity.

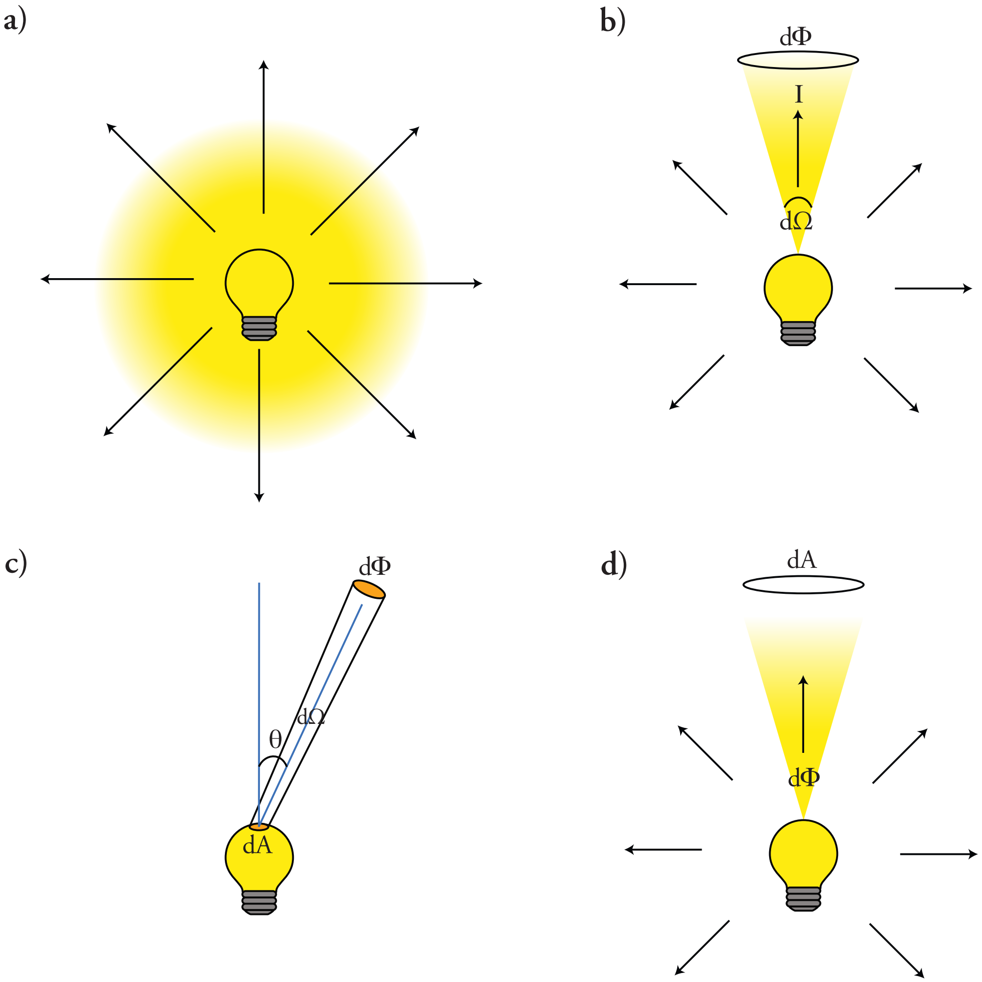

Figure 2.10: a) A light source emitting radiant power uniformly in every direction. b) The radiant intensity of a source is defined by the ratio of the radiant power (*d*Φ) and solid angle (*d*Ω). c) The radiance of a source is the ratio of the radiant intensity and the area of the source (*dA*). θ is the angle between *dA* and the position where the radiant intensity is measured. d) Irradiance describes the amount of radiant power falling on a surface area (*dA*).

Table 2.1: A summary of the radiometric and photometric quantities.

Radiometric Parameters			Photometric parameters	
Quantity	Equation	Unit	Quantity	Unit
Radiant Power	Φ	W	**Luminous Power**	lm
Radiant Intensity	I = dΦ/dΩ	W/sr	**Luminous Intensity**	lm/sr = cd
Radiance	R = I/dA·cosθ	W/sr·m^2	**Luminance**	cd/m^2 = nits
Irradiance	E = dΦ/dA	W/m^2	**Illuminance**	lm/m^2 = lux

2.4 Diffusion Driven LEDs

In section 2.1, the use of the DHJ to improve the efficiency of LEDs was introduced. This structure has been in use over the last 60 years and is by now considered the industry standard. The active region in such structures is a MQW, where the layers are so thin that electron transport is quantised in at least one direction, which enhances the carrier recombination by confining them. There are however disadvantages to using this structure, such as (i) having to make contacts on the top and bottom of the device which limits the amount of the extracted light, (ii) the high refractive index of the active region compared to air, leading to total internal reflection, and (iii) challenges in fabricating nanostructures with this device geometry [106]. About 10 years ago, a new concept to design LEDs was developed where the active region is located outside of the *pn* junction. Two different device architectures have been successfully demonstrated experimentally. In the first one, a buried MQW stack was grown, followed by the growth of the n- and p-doped regions. Under a bias, the carriers preferentially go towards the MQW by bi-polar diffusion because of its smaller bandgap which acts as a sink for the carriers [107]. The demonstration of this proof of concept led to the development of a surface QW LED. In this second architecture, an InGaN QW is located on top of a GaN *pn* junction and upon applying a bias, light is emitted from the QW [54]. The experimental confirmation of these two designs led to the concept of diffusion driven LEDs. In this architecture, the carriers diffuse towards a lower bandgap region located outside the *pn* junction. The design makes it possible to avoid having any contact on top of the active region. Their measurements resulted in strongly blue emitting light.

Following the approach of diffusion driven LEDs, one can think of implementing them into NWs. An interesting structure that can be used for this purpose is a tree structure. High bandgap *pin* NWs can be grown, followed by branch growth with a lower bandgap. Once a bias is applied, the injected carriers can diffuse towards the branches and recombine. The branches having a thin diameter allow the light to be emitted efficiently. In Figure 2.11 (a) a schematic of the concept is shown, along with a scanning electron microscope (SEM) image of InP cores with InP branches (Figure 2.11 (b)). In order to prepare these structures, several steps have to be carried out. The process starts with the patterning of the substrate with catalytic metal particles by Displacement Talbot lithography (DTL). Then the NWs are grown, followed by the deposition of new Au particles on the sidewalls and the growth of branches out of them. The process is finalised by fabricating devices. In the next chapter, the main points of NW synthesis will be discussed.

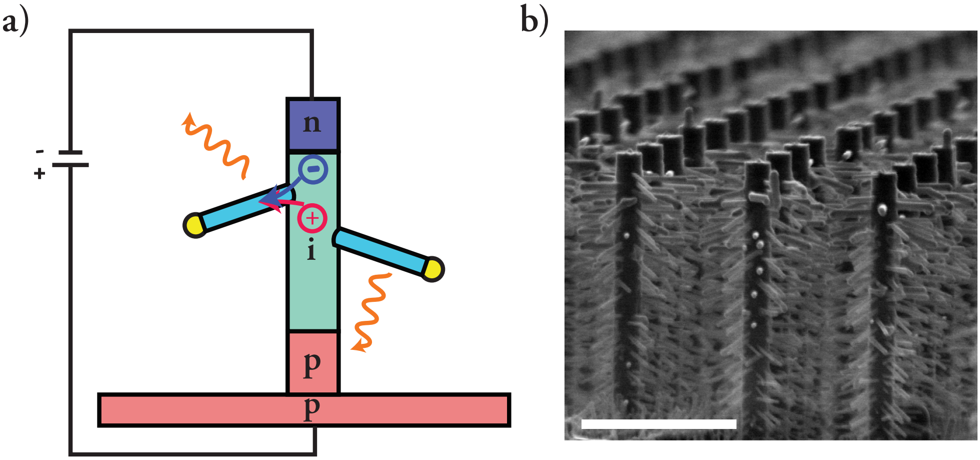

Figure 2.11: a) A schematic of a nanotree LED with a high bandgap core and lower bandgap branches. Upon the application of a voltage bias, the carriers diffuse into the branches and recombine to emit light. b) Cross-section SEM image of a nanotree array. The scale bar is 1 µm.

3 Nanowire Synthesis

> *Once there was an explosion, a bang which gave rise to life as we know it. And then, came the next explosion. – Hideo Kojima*

This chapter is going to delve into NW and NW-branch growth. To do so, the step-by-step procedure is going to be discussed. First, we are going to discuss DTL which enables the growth of regular NW arrays. Then we are going to discuss NW growth via metal-organic vapour phase epitaxy (MOVPE). Finally, a section is dedicated to the discussion of electroless deposition which serves to decorate NWs with Au particles and the subsequent branch growth.

3.1 Substrate Patterning by Displacement Talbot Lithography

To make LED devices based on NWs, thousands of NWs should be connected in parallel to increase the light output power. Achieving this high density of NWs is done through substrate patterning, where one creates a periodic pattern covering the entire substrate. In this work we have used a lithography method, DTL, to create the periodic pattern. The technique is based on the Talbot effect, discovered in 1836 [108]. Upon illumination of a periodic grating with a monochromatic collimated light, a three-dimensional diffraction pattern is generated which is repeated after a certain period, called the Talbot period, resulting in a self-image of the grating [109]. However, the standard Talbot effect has a limited depth of field, requiring very precise placement of the substrate away from the grating. In DTL this limitation is overcome by continuously displacing the substrate over at least one Talbot length in the perpendicular direction with respect to the mask. This movement results in an integration of the diffraction pattern intensity in the axis perpendicular to the mask and ensures a reliable transfer of the pattern [110-112]. The substrates used in this work are 2” wafers. The wafer is covered by a double-layer resist, wherein the bottom layer is a lift-off resist, and the top layer is a deep UV sensitive resist. The technique uses an argon fluoride (ArF) laser which emits at 193 nm, part of the UV spectrum, to image the pattern from a phase shift mask onto the photoresist. The phase-shift mask used to define the pattern has a hole size of 120 nm and a pitch of 1 µm, fabricated on quartz. After the exposure, the photoresist is developed, followed by a Au evaporation step and lift-off to remove the excess Au. The final structure is a periodic array of Au particles. In Figure 3.1 (a), a top view of the wafer after development is shown. The inner circle defines the hole size after exposure which can be changed by varying the exposure dose

[26], while the outer circle defines the size of the undercut, since during development, the lift-off resist is etched isotropically in the radial direction. The undercut is necessary to facilitate the lift-off process after Au evaporation. The faint and small circles that form a hexagon, visible between the primary holes, arise because of the secondary diffraction effect once the exposure dose is too high [113]. In this work, their appearance has not given any contribution as they are not fully developed and thus do not form a pathway for the Au particles to deposit on the wafer. It must be noted that the hole size inspected on the SEM after the lithography step is not fully accurate as the electron beam influences the resist and the hole expands. A more accurate measurement is after Au evaporation. Figure 3.1 (b) shows a top view SEM image of the wafer after Au evaporation and lift-off.

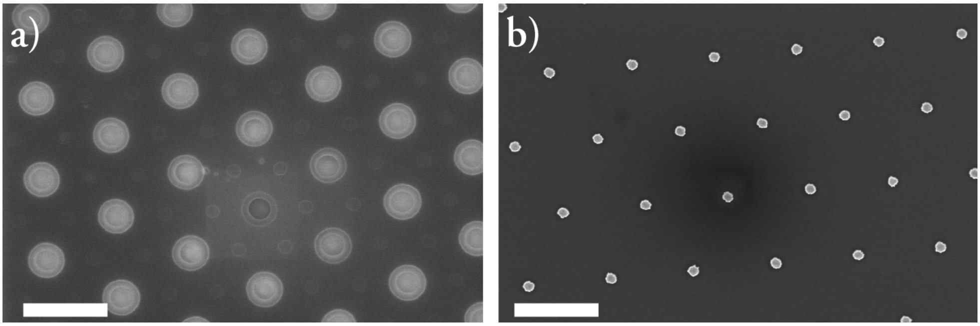

Figure 3.1: a) Top view SEM image of the photoresist after development. b) Top view SEM image of the wafer after lift-off, decorated with Au particles. The scale bar is 1 µm.

3.2 Metal Organic Vapor Phase Epitaxy

The two main approaches followed to create nanostructures are the top-down and the bottom-up approach. In the top-down approach, one starts from a bulk substrate and constructs complex structures by performing various lithography steps (photolithography or electron beam lithography) and using etching techniques such as reactive ion etching (RIE) [114]. The method, although very successful can become time-consuming depending on the processing steps necessary and can be restricted in the flexibility of what one can achieve. Furthermore, etching processes such as RIE are quite aggressive and lead to surface roughness of the structure, which depending on the application that one aims for, can become a limitation. In the bottom-up approach on the other hand one starts from a substrate and deposits new material on it to form the desired structure. The bottom-up approach is the chosen method in this work by growing NWs on a substrate. The technique used in this thesis to grow NWs is MOVPE. Through many years of development and sophistication, it is an extremely mature technique to grow high quality III-V semiconductors. In MOVPE, the desired precursors are supplied to the growth front in the gas phase where they afterwards incorporate in the crystal. At least one of the precursors supplied to grow the crystal is a metal-organic (MO) compound. Typically for III-V semiconductors, the group III source is an MO precursor. In an MO, the metallic component is bound to organic molecules. One can take as an example the case of indium (In) which is bound to three methyl groups $(CH_3)_3$, forming trimethylindium (TMIn) and Ga which is bound to three ethyl groups $(C_2H_5)_3$ forming triethylgallium (TEGa). Group II and IV precursors such as diethylzinc (DEZn) and tetraethyltin (TESn) used to dope the NWs are also supplied as MOs [23]. The group V used in this thesis are hydride gases such as phosphine (PH_3) and arsine (AsH_3) stored in pressurised liquid bottles.

Figure 3.2 provides a simplified schematic of the Aixtron 200/4 MOVPE used in this work. The group III and dopant precursors are generally in liquid state at room temperature, except for TMIn which is in solid state. They are stored in bubblers which have an inlet and outlet to let the carrier gas enter inside the bubbler and transport the precursor material to the growth chamber via the outlet. Inside the bubbler, there is a thermal equilibrium between the vapour pressure of the MO and its liquid/solid. The bubblers are immersed in a bubbler bath to control the temperature. The bubbler bath contains a water/glycol mixture. Hydrogen (H_2) is used as the carrier gas and the flux with which it is sent into the bubbler is controlled with mass flow controllers (MFCs). The H_2 flowing inside the bubbler saturates with the precursor molecules. The H_2 flow together with the pressure and the temperature in the bubbler control the amount of the MO flux supplied to the reactor, according to equation 3.1:

$$\Phi_{\mathrm{MO}} = \frac{p_{\mathrm{MO,vap}}}{p - p_{\mathrm{MO,vap}}} \Phi_{\mathrm{H_2}} \tag{3.1}$$

where p is the pressure in the bubbler, $\Phi_{\mathrm{H_2}}$ the H_2 flux and $p_{\mathrm{MO,vap}}$ is the equilibrium vapour pressure of the precursor, which is calculated from the empirical formula in equation 3.2:

$$p_{\mathrm{MO,vap}} = 10^{a-\frac{b}{T}} \cdot \frac{1013.25}{760} \tag{3.2}$$

where T is the temperature of the bubbler, a and b are tabulated constants depending on the source and the conversion factor is to calculate the vapor pressure in mbar instead of mmHg. The total flow sent into the reactor is 13 L/min and the reactor pressure is 100 mbar. By dividing the MO flow by the total flow in the reactor, the molar fraction χ (equation 3.3 & 3.4) is calculated which is the more relevant parameter to look for when attempting to reproduce experiments.

$$\chi_{\mathrm{MO}} = \frac{\Phi_{\mathrm{MO}}}{\Phi_{\mathrm{Tot}}} \tag{3.3}$$

Since the group V precursors are supplied in gaseous form, their molar fraction is the ratio of the input flow to the total flow.

$$\chi_{\mathrm{Hyd}} = \frac{\Phi_{\mathrm{Hyd}}}{\Phi_{\mathrm{Tot}}} \tag{3.4}$$

Inside the growth chamber, the substrate on which the NWs grow is placed on top of a graphite susceptor which in our setup is heated by IR lamps to the desired growth temperature. At the backside of the reactor chamber the exhaust is located, which sends the unused and by-product gases to a scrubber to prevent the release of harmful substances to the environment.

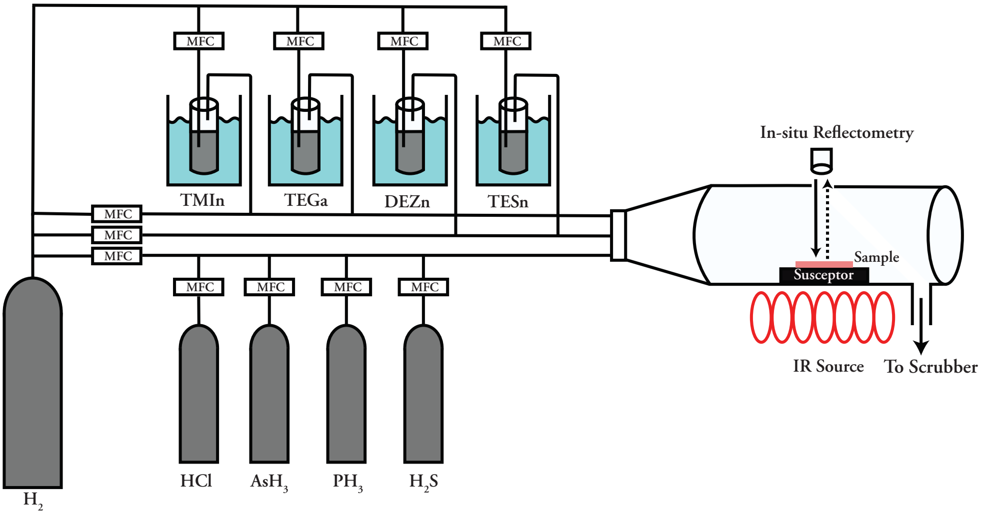

Figure 3.2: A simplified schematic of the Aixtron 200/4 MOVPE used in this work to grow NWs.

3.2.1 Vapour-Liquid-Solid Growth of Nanowires

NWs are elongated structures, which are typically grown via the vapour-liquid-solid (VLS) mechanism. The first use of particle-assisted growth of NWs is attributed to Wagner and Ellis, who reported the growth of Si whiskers by using Au seed particles [115]. They were often reported as whiskers since the structures grown by them were several micrometres long. The VLS method, as the name suggests, has three phases contributing to the growth. Once the precursors are introduced to the growth front and pyrolyze at elevated temperatures (vapour phase), they will start alloying with the Au seed particle on the substrate. The NW growth process is a complex one, where many reactions occur simultaneously, leading to the formation of intermediate species. Furthermore, the presence of several precursors along with their radicals and the presence of the substrate affects the pyrolysis rate of the precursors. The gaseous precursors which are sent in the reactor pyrolyze at elevated temperatures, breaking their organic bonds and releasing the group III and V precursors which then incorporate into the crystal [116]. Pyrolysis can occur in the gas phase and one talks about homogeneous pyrolysis. Most of the pyrolysis, especially in the low temperature regime used for kinetically limited growth, occurs close to surfaces and then one talks instead of heterogeneous pyrolysis. Furthermore, being a low-pressure reactor, the mean free path of the molecules increases and reduces the probability of homogeneous pyrolysis. Reality is of course never that simple, and during growth both types of pyrolysis occur. In the case of InP NW growth, we have used TMIn and PH_3 as the In and phosphorus (P) sources, respectively. In is the material which forms an alloy with Au [117, 118]. The Au particle acts as a catalyst for the decomposition of the precursors by locally reducing the chemical potential and becoming a sink for particle accumulation [119]. At the typical growth temperature, the Au is solid. By increasing the concentration of the precursors inside the Au seed an alloy is formed, and the melting temperature is reduced. At a sufficient concentration of the precursors alloyed with the Au and if the growth temperature is above the eutectic point, a melt is obtained (liquid phase). The eutectic point is found in the phase diagram [120]. When growing InP, the ternary phase diagram Au-In-P should be considered. However, this ternary phase diagram is not known. The solubility of P in Au can be neglected for the typical growth temperatures of InP NWs at 440 °C [121], and therefore it is sufficient in a first approximation to consider only the Au-In phase diagram. Further addition of precursor material leads to a saturation of the Au particle with precursor. Eventually, supersaturation is reached, and the excess material is expelled underneath the Au particle, precipitating, where crystal nucleation proceeds in a layer-by-layer growth (solid phase). Group III atoms like In are typically physisorbed on the growing NW sidewall or incorporated via the seed particle, while group V incorporate via the triple phase boundary as they have negligible solubility in Au. Figure 3.3 shows a simplified schematic of the NW growth process. In Figure 3.3 we can see molecules of TMIn and PH_3 being supplied to the growth front. The TMIn and PH_3 pyrolyze and release methyl and hydrogen radicals, respectively. A general reaction can be written as:

$$In(CH_3)_3 + PH_3 \rightarrow InP + 3CH_4$$

The growth conditions such as temperature and V/III ratio [28, 29], along with the diameter of the NWs [32] affect their crystal structure. In NW form, apart from the normally occurring ZB crystal phase in the bulk, they also exhibit the WZ crystal phase [117, 122, 123]. The formation of different crystal structures can also lead to changes in the bandgap of the material. For example, InP has a bandgap of 1.34 eV in ZB and 1.42 eV in WZ [124], and as mentioned earlier WZ GaP even transitions to a direct bandgap material [125, 126]. Doping is also a factor strongly influencing the crystal structure by changing the surface energy during growth [17, 18, 40, 127].

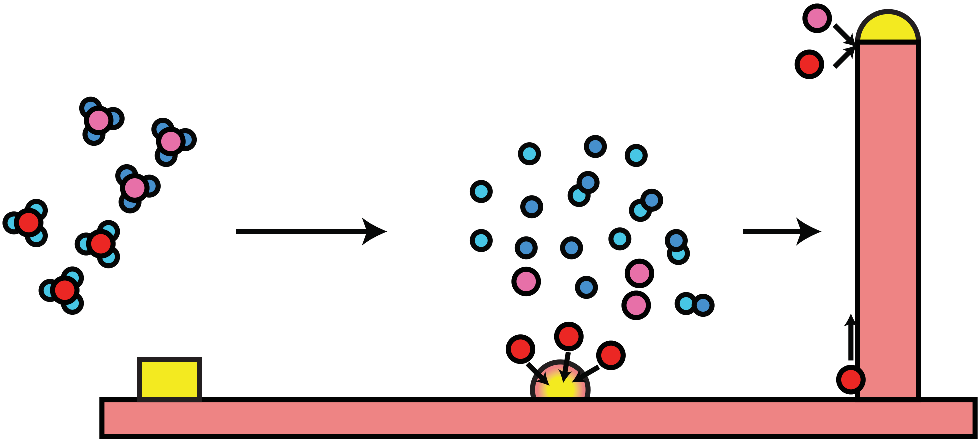

Figure 3.3: A schematic of the VLS growth to grow NWs. The initial Au seed particle is in solid form. Upon introduction of the precursor material, they pyrolyze at elevated temperatures, releasing the group III (red) and V (purple) atoms through a series of chemical reactions. The group III atoms start alloying with the Au seed. By increasing the concentration of the group III inside the Au and at elevated temperatures above the eutectic point, it turns into a liquid. The released radicals such as CH_3 and H can interact with each other and form intermediate compounds. After supersaturation is reached in the Au particle, the NW starts growing and new material is incorporated either by surface diffusion through the sidewalls of the NW or via the triple phase boundary.

3.3 Electroless Deposition

Metal deposition on a substrate has long been investigated to provide surface coatings. A common method to achieve this goal is electrodeposition, where a conductive substrate is immersed in the aqueous solution of a metal and upon application of an electric current, the metal is deposited on the conductive substrate [128]. However, apart from electrodeposition, an important method with numerous applications in the fields of material enhancements [129-131], and electrical interconnects is electroless deposition [132]. The technique has been used since 1835 by von Liebig to perform silver plating and in 1844 by Wurtz to perform nickel plating [133]. The description of the underlying phenomena and the term electroless plating was given much later, in 1947 by Riddel and Brenner [134]. Electroless deposition allows for the plating of noble metals on the surfaces of less noble metals and semiconductors by immersing the desired substrate to be plated into a bath of an aqueous solution containing ions of the noble metal without the application of an electric current [135]. During the deposition process, a redox reaction occurs in the bath. The ions of the noble metal interact with the substrate and get reduced, while the substrate itself becomes oxidised [136-142]. The process can be summarised by the two following reactions:

$$M^{n+} + ne^{-} \rightarrow M^{0}$$
$$Sub^{0} \rightarrow Sub^{n+} + ne^{-}$$

where *M* represents the metal initially in an oxidation state n, which receives n electrons and becomes reduced to a zero-oxidation state, and *Sub* represents the substrate which releases n electrons and becomes oxidised to a state n. This reaction leads to particles of the noble metal to form on the substrate surface. The method does not require complicated equipment to perform a metal deposition. Although the phenomenological principle is simple to explain and understand, the solutions themselves can be quite complex as apart from the metal ions and the reducing agent, very often pH adjustment additives and oxide etchers are needed to maintain a continuous deposition [143-146]. In Papers I-III, electroless deposition is utilised to deposit Au particles on the sidewalls of the core NWs. These Au particles act as seeds to then grow the branches. The Au-containing chemical used in this work is chloroauric acid ($HAuCl_4$). The acid is in solid form at room temperature and is dissolved in deionised water (DI H_2O), creating an aqueous solution. The sample with NWs, which plays the role of *Sub*, is then immersed in the solution. In the case of InP NWs, once the electroless deposition process begins, Au^{3+} is reduced to Au^{0} and deposited on the NW sidewalls, followed by the formation of indium trioxide (In_2O_3) and phosphorus pentoxide (P_2O_5). Figure 3.4 depicts a graphical representation of the deposition process. This method is cost and time-efficient as compared to other deposition methods, such as aerosol deposition which has been used in the past to grow branches [147-149]. Another advantage of the method compared to aerosol deposition is the deposition of particles along the entire core length, whereas in the deposition of the aerosol particles the electric field distribution and interaction with the NW array makes it such that particles are mostly deposited close to the tip of the cores [150].

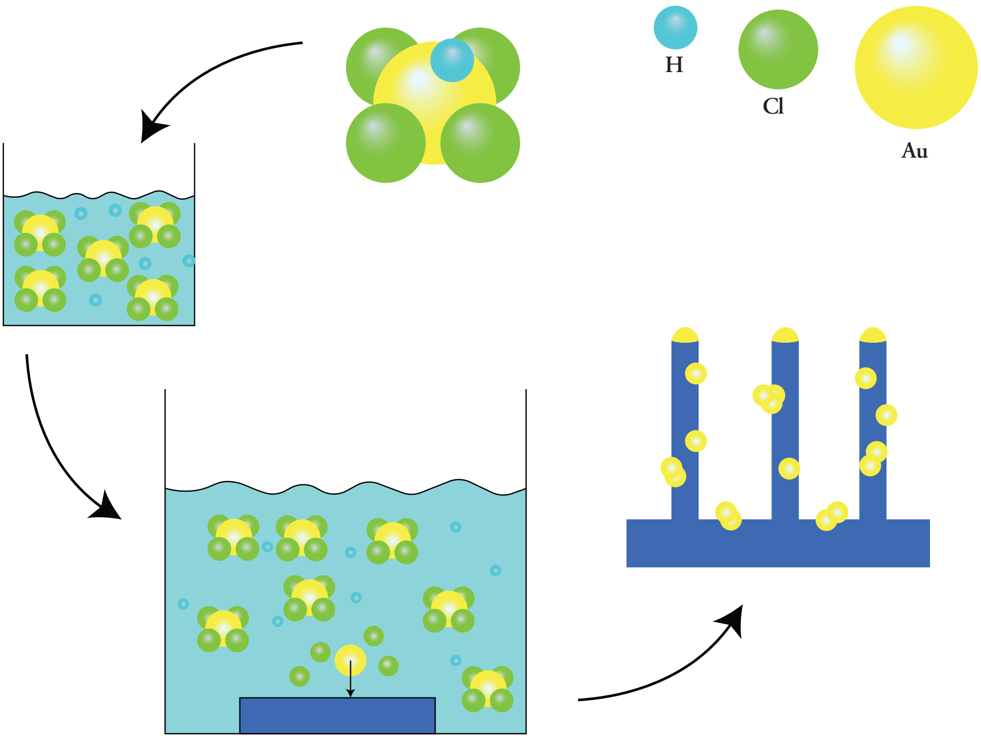

Figure 3.4: A schematic of the process evolution in electroless plating. The Au precursor, $HAuCl_4$, is dissolved in DI H_2O, where the chemical splits apart in ions of H^+ and $AuCl_4^-$. The Au salt is afterwards divided into Au^{3+} and 4 Cl^- ions. Upon the immersion of the sample, the Au ions are reduced on the sample and the sample is oxidised. The last drawing of the schematic shows a zoom in of the sample which contains NWs and the Au reduction occurring on both the NWs and substrate.

In Paper I, in the first part, the tuning of the Au deposition on the NWs was studied by varying three parameters: i) the temperature of the solution, ii) the concentration of the solution, iii) the deposition duration i.e., the time the sample stays immersed in the solution.

We turn our focus first on the temperature variation. While keeping the concentration at a constant value of 1 mM, a temperature series from 20 – 80 °C in steps of 20 °C was performed for various deposition times. In Figure 3.5 (a)-(d) the series for 1 minute deposition time is shown in the SEM images. Starting at room temperature, the deposition provides fine particles which are distributed along the entire core NW length. By increasing the temperature, the size of the particles increases while at the same time decreasing the density of the deposition compared to room temperature. A higher temperature accelerates the electroless deposition reaction [135]. The increase in temperature leads, apart from an accelerated deposition rate, to a change in the effective concentration of the solution. Considering the water-based nature of the solution, water desorption occurs at an increased rate when increasing the temperature close to the boiling point of water. This reduction in water content changes the effective concentration of the solution.

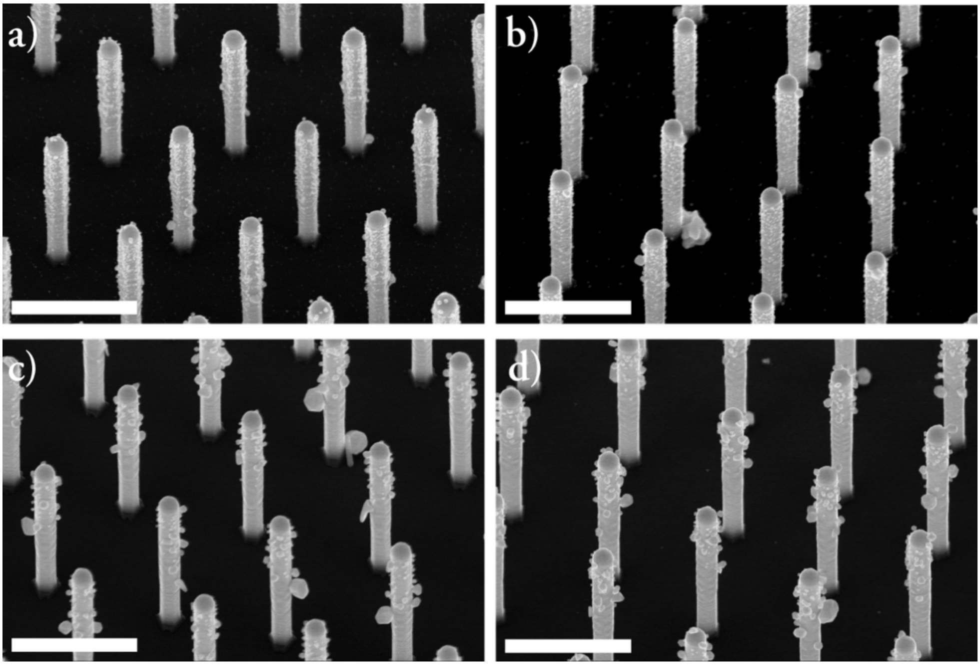

Figure 3.5: Representative SEM images of the temperature variation of the Au deposition. a) 20 °C, b) 40 °C, c) 60 °C, d) 80 °C. The scale bar is 1 µm.

Moving our attention to the second parameter, we are going to discuss now the variation of the solution's concentration. In this parameter study, the temperature was kept at a constant of 18 °C and the deposition time was fixed at 30 s, while the concentration of the solution was varied. The concentrations of the solution were 0.25, 0.5, 1, 2 and 4 mM. Figure 3.6 (a)-(e) shows the SEM images of the deposition results for the entire concentration series. This variation provides important observations: (i) the distribution of particles along the NW length changes with concentration, (ii) unless the concentration is increased to 4 mM the number of particles deposited on the NWs is similar between the different concentrations, (iii) changing the concentration, the size of the deposited Au particles changes. Comparing between the different SEM images, the 0.25 mM solution provides deposition of Au particles distributed primarily on the upper half of the NWs and increasing the concentration results in a more uniform spreading of the particles. Although for up to the 2 mM solution the number of particles deposited is similar, the same cannot be said in the case of the 4 mM solution, where the particle deposition is observed to have dropped considerably. Apart from the deposition on the sidewalls of the NWs, the particles also deposit on the substrate. With an increase in the concentration of the solution, more particles form on the substrate, and their size increases. This explains the observed results in the experiments, in which we attribute the decreased number of particles that form on the NWs from the 4 mM solution to the increased number of particles that form on the substrate instead. Using the 0.25 mM solution leads to the smallest deposited particles, with a diameter of ~5-10 nm and the 4 mM solution has the biggest deposited particles, ~20-30 nm. It is also noticeable that the risk of forming agglomerations of Au particles increases with an increase in concentration. Similarly, this behaviour resembles that of depositing at a high temperature, which as previously discussed leads to a higher effective concentration and formation of bigger particles.

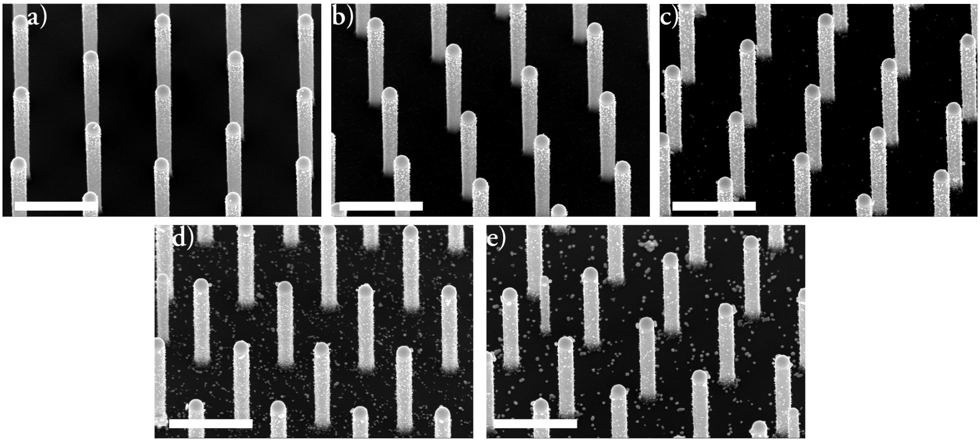

Figure 3.6: Representative SEM images of the concentration variation of the Au deposition. a) 0.25 mM, b) 0.5 mM, c) 1 mM, d) 2 mM, e) 4 mM. The scale bar is 1 µm.

To further study the parameter space and increase the control over the deposition, the time of sample immersion in the solution was varied while keeping a constant concentration of 1 mM and temperature of 18 °C. The variation can be classified into a short timescale and a long timescale. In the short timescale, the deposition times studied were 1, 5, 10, 15, 20 and 30 s, while in the long timescale, the deposition was varied from 1 to 10 min in steps of 1 min. Figure 3.7 (a)-(d) shows representative SEM images of depositing Au from a 1 mM solution on the NWs for 1 s, 10 s, 2 min and 10 min, respectively. An interesting result is that the timescale of the initial Au nucleation is below 1 s, as even this short time proceeds with a high coverage of the sidewalls. Increasing the time leads to more particles being deposited and to the appearance of larger Au droplets formed by the agglomeration of the particles. This process seems to reach a saturation point after 2 min, after which the observed agglomerates do not become more frequent. The formation of the bigger particles can be a form of Ostwald ripening in which small particles diffuse to form larger particles and space is being freed up for new Au droplets to deposit, but the occurrence of this mechanism in electroless deposition is still an open question [151, 152]. In our case, the results do not indicate Ostwald ripening as the droplets do not become much bigger with time. Another possibility is that most of the NW sidewalls are covered with particles, but some nuclei are much smaller than what can be observed in the SEM. A complete coverage would lead to a halt of the redox reaction and no further deposition of Au to occur [153].

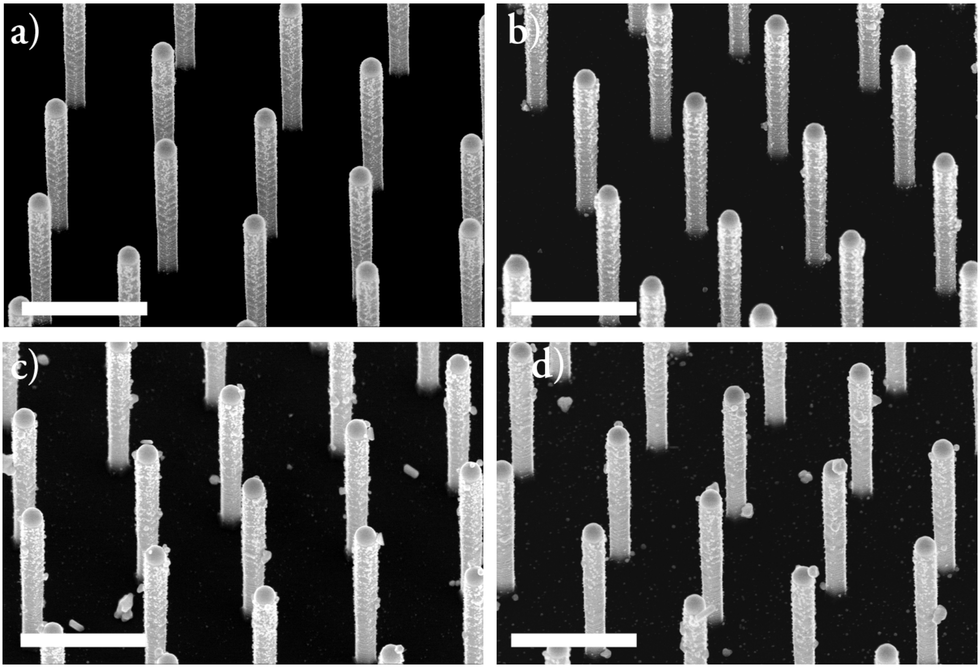

Figure 3.7: Representative SEM images of the time variation of the Au deposition. a) 1 s, b) 10 s, c) 2 min, d) 10 min. The scale bar is 1 µm.

As a last factor affecting the Au deposition in our system, we turn our attention to the age of the NWs, i.e. how long after the NW growth does the deposition take place. At first a parameter that is easy to overlook as NWs have shown very good long-term stability in device operation [39]. The experiments have shown that it is preferable for the deposition to be done immediately after NW growth. We tested the deposition on what we consider as aged NWs (>5 days after growth) which shows substantial differences in the results after the deposition of particles under the same conditions, compared to fresh NWs, as shown in Figure 3.8. There is a substantial decrease in the number of deposited particles along with an increased size of the particles on the aged NWs. We have attributed the reason for this behaviour to changes in the native oxide surrounding the NWs which alters the redox reaction and interaction with the Au-containing solution.

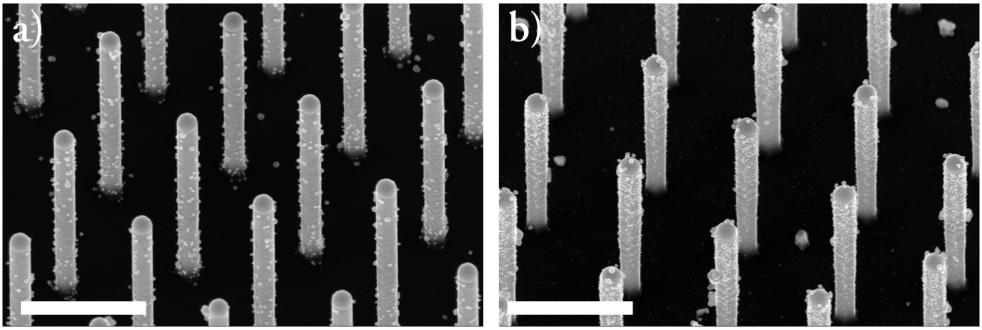

Figure 3.8: SEM images of the Au deposition comparison on the age of the NWs. a) Aged NWs, b) As-grown NWs. The scale bar is 1 μm.

3.4 Analysis of Nanowire Growth

3.4.1 SEM

In order to image nanoscale materials such as NWs, a higher resolution than the one provided by light microscopy is necessary. This is done by electron microscopy, which uses electrons as the source of imaging. Electrons have a shorter wavelength compared to photons, determined by the accelerating voltage. In the SEM used in this work, the electron beam is generated via a field emission gun, where a strong electric field is applied to pull electrons off the filament's tip. The electron beam is then focused on the sample and scanned with the help of electromagnets. The electron beam-sample interaction produces a variety of signals such as secondary electrons (electrons which are emitted from the sample), backscattered electrons (coming from the original beam) and X-rays. A detector in the SEM collects the secondary electrons produced by scanning the electron beam and constructs the image. The SEM is a very powerful tool to do post growth inspection of the sample, where one can obtain information about the NW length, diameter, quality of pattern preservation, and crystal structure.

3.4.2 TEM

Similarly to the SEM, a transmission electron microscope (TEM) uses electrons to image a sample. However, the complexity of the equipment is much higher, and in a TEM, the accelerating voltage is about 200 times higher than in an SEM, resulting in electrons with a much lower wavelength and higher resolution. While in an SEM a detector measures scattered electrons, in a TEM one measures the electrons that go through the sample with little to no interaction. As such it is very important that samples measured in a TEM are thin enough to minimise the interaction volume to obtain atomic resolution. The TEM has been used in this work to image the branches and obtain insights regarding their crystal structure, their connection to the core NWs and their composition. The composition is measured by operating the TEM in scanning TEM mode and performing energy dispersive X-ray spectroscopy (EDX). Previously, we mentioned that one of the signals produced by the beam-sample interaction is X-rays. When the high energy electrons interact with the sample, electrons from the inner shells of the material can be excited and removed from it. The vacancy left behind is then filled with an electron from a higher shell. This transition releases an X-ray, the energy of which is characteristic of the specific material. Since in a TEM the interaction volume is small, one can obtain very high spatial resolution maps of the composition.

3.4.3 XRD

When growing ternary structures, it is of interest to investigate their composition directly after growth to further optimise it. X-ray diffraction (XRD) is a measurement technique which is routinely used for such purposes. XRD relies on a constructive interference effect when X-rays are reflected from the lattice planes of a crystalline material, the condition for which is given by Bragg's law:

$$2dsin\theta = n\lambda \tag{3.5}$$

where d is the distance between the lattice planes, θ is the angle between the lattice plane and the beam of X-rays and λ is the wavelength of the X-rays which is similar to the distance between the lattice planes. The result of the XRD can be used alongside Vegard's law in equation 2.7 to find the composition of the ternary compound. During the measurement, the θ angle is scanned and the measurement is reported as the X-ray intensity with respect to the 2θ angle.

3.5 Nanotree Structures

Sample preparation for branch growth

Before continuing to grow the branches, an intermediate step is done to remove the Au seed particle from the core NWs. If this step is not done, during branch growth the cores will also grow and compete with the branches for precursor material as shown in Figure 3.9. The sample is thus coated with a photoresist. Since the aim is to remove the seed particles in the entire substrate, a short 1 s UV flood exposure is performed to uncover the tips of the cores [154]. After the tips are exposed, the sample is immersed in a buffered oxide etch (BOE) (1:10) solution, to etch the native oxide around the Au seed particle for 25 s. It must be noted that even though the term "Au seed" is used, it is in fact an alloy since In is also found in it [155], and thus it is susceptible to oxidation.

To etch the Au particle the sample is then immersed in potassium iodide (KI) for 25 s and then flushed in DI H_2O. The photoresist is finally removed by using Microposit Remover 1165 and the samples are flushed for 5 min in DI H_2O to make sure that no organic residues remain on the sample.

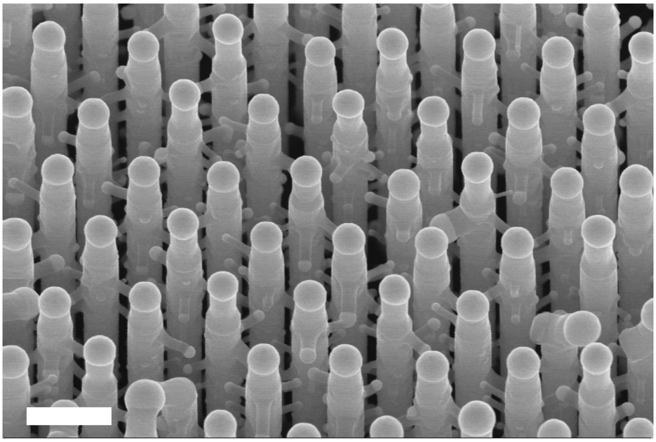

Figure 3.9: SEM image of core growth alongside branch growth when the Au seed particle is not removed from the cores prior to branch growth. The scale bar is 500 nm.

3.5.1 Homostructure trees

The results in Paper I report apart from the successful Au deposition, also the successful growth of InP branches on InP cores. As this material combination provides the simplest architecture to find the growth parameter space, it facilitates us to obtain the proof of concept needed to show that branch growth is possible in a high density. Figure 3.10 (a)-(e) shows a top view of the branches grown using Au-deposited samples at different concentrations. The growth results are strongly affected by the concentration of the solution since it influences both the size and number of particles deposited. The cores have a 3-fold symmetry [148], making the branches grow in the three symmetry related ⟨111⟩B directions. The presence of twin planes in the cores causes a rotation of the crystal structure with 60° which results in 6 downward pointing ⟨111⟩B growth directions [147, 148, 156]. However, the growth direction of the branches as we shall shortly discuss is not always in the ⟨111⟩B direction. Looking at Figure 3.10 (a), when the concentration of the solution is the lowest, it results in branches grown aligned to one another, with little spreading along the growth axis, making the apparent 6-fold symmetry visible.

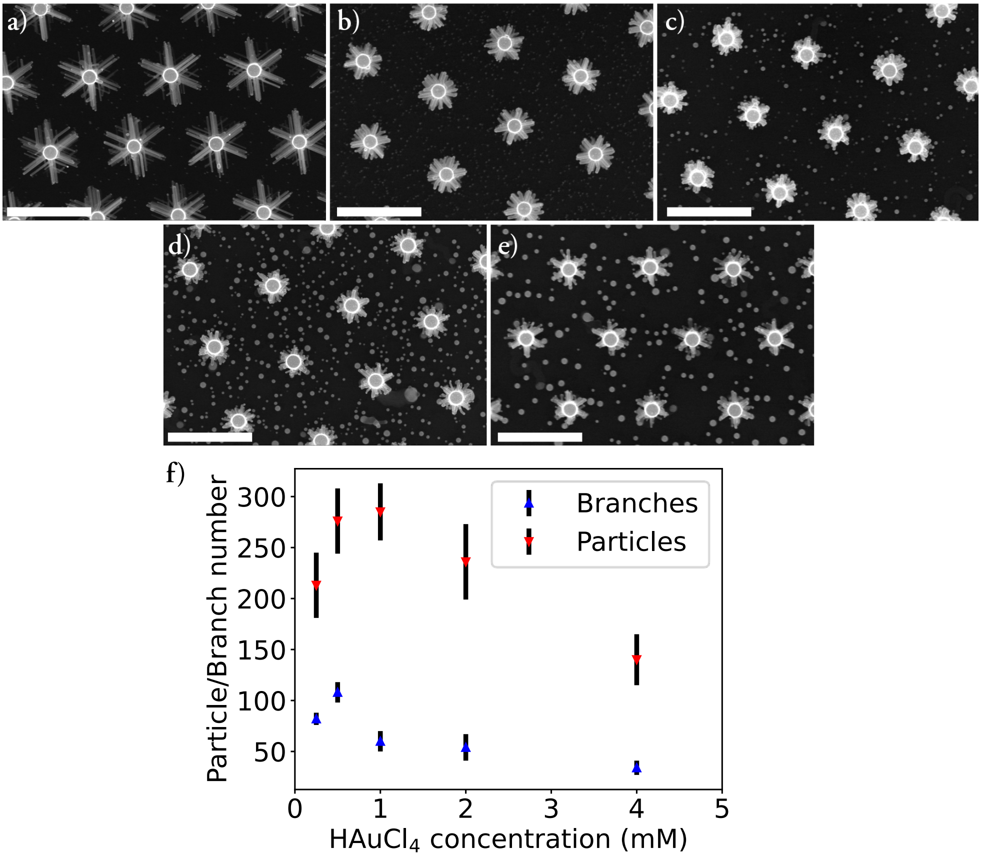

Figure 3.10: Top view SEM images of InP branches grown on InP cores using different concentrations of the Au solution. a) 0.25 mM, b) 0.5 mM, c) 1 mM, d) 2 mM, e) 4 mM. The scale bar is 1 µm. f) A plot with the average number of particles deposited on the cores (red) and the average number of branches grown (blue) with respect to the concentration of the solution.

Another distinct feature of these branches is the narrow distribution of the length and diameter between different branches. The results from an increase in concentration show that the branches have a broader distribution in diameter and that the branches are not perfectly aligned along the facets of the cores.

The larger size of the Au particles deposited on the substrate when increasing the concentration leads to a substantial parasitic NW growth on the substrate. These Au particles compete for the precursors with Au particles on the sidewalls of the core NWs. In Figure 3.10 (f), a plot of the average number of particles deposited and branches grown with respect to the solution concentration is shown. The plot shows that the number of particles measured before growth is several times higher than the number of branches counted after growth. This indicates that before branch nucleation occurs the Au particles move along the NW and coalesce to form bigger Au droplets. The coalescence leads to fewer branches with a larger diameter compared to the original Au particle size.

To inspect the branches further we have taken cross-section SEM images of the samples, shown in Figure 3.11 (a)-(d). The images show the branch growth on samples where the Au deposition was carried out for different time durations. The results show that instead of the expected $\langle 111 \rangle$B growth direction, the branches have a preferential growth in the $\langle 110 \rangle$ direction for the shortest deposition time of 1 s, and $\langle 111 \rangle$B grown branches occur for longer deposition times. Figure 3.11 (e) presents a plot to visualise the occurrence of branches grown in the $\langle 110 \rangle$ and $\langle 111 \rangle$B with the deposition time. The number of $\langle 111 \rangle$B directed branches increases for depositions up to 2 min. Then a constant ratio close to 0.1 is reached, meaning that on average for every 10 branches grown in the $\langle 111 \rangle$B direction, there is one branch grown in the $\langle 110 \rangle$ direction. A similar result was discussed in Chapter 3.3 regarding the saturation of particle deposition after the first 2 min. While research has shown that the growth direction of NWs can be tuned by changing their diameter [157], this is not the case in our results as we do not observe such a dependence. We have attributed the reason for this behaviour to the Au-containing solution. During the deposition process the redox reaction proceeds by dissociating the $AuCl_4^-$ ions into Au^{3+} and 4 Cl^- where the Au^{3+} is then reduced to Au^0. The Cl^- ions can etch the native oxide surrounding the cores. Furthermore, H^+ and Cl^- can interact and form hydrochloric acid (HCl) which is known to etch InP [158]. We have raised the hypothesis that during the Au deposition the native oxide is being etched. During short deposition times (<2 min), the etching of the oxide is partial. Once the samples are reinserted into the growth reactor and heated to the growth temperature, the Au particles start migrating around the core and form bigger Au particles by agglomeration. However, the migration length is not expected to be long as the particles are located very close to each other. When the Au migrates on the core NWs, it can desorb the native oxide underneath [159] while still being surrounded by the native oxide that remained after the deposition was terminated. Because the Au particles are trapped by an oxide surrounding them, it forces the branches to grow in the $\langle 110 \rangle$ direction [160, 161]. When the deposition is done for longer times (> 2 min), the etching process continues for a longer time as well, and the Au particles do not become trapped by an oxide during branch growth anymore. We speculate that this then causes the growth to proceed mostly in the expected $\langle 111 \rangle$B direction.

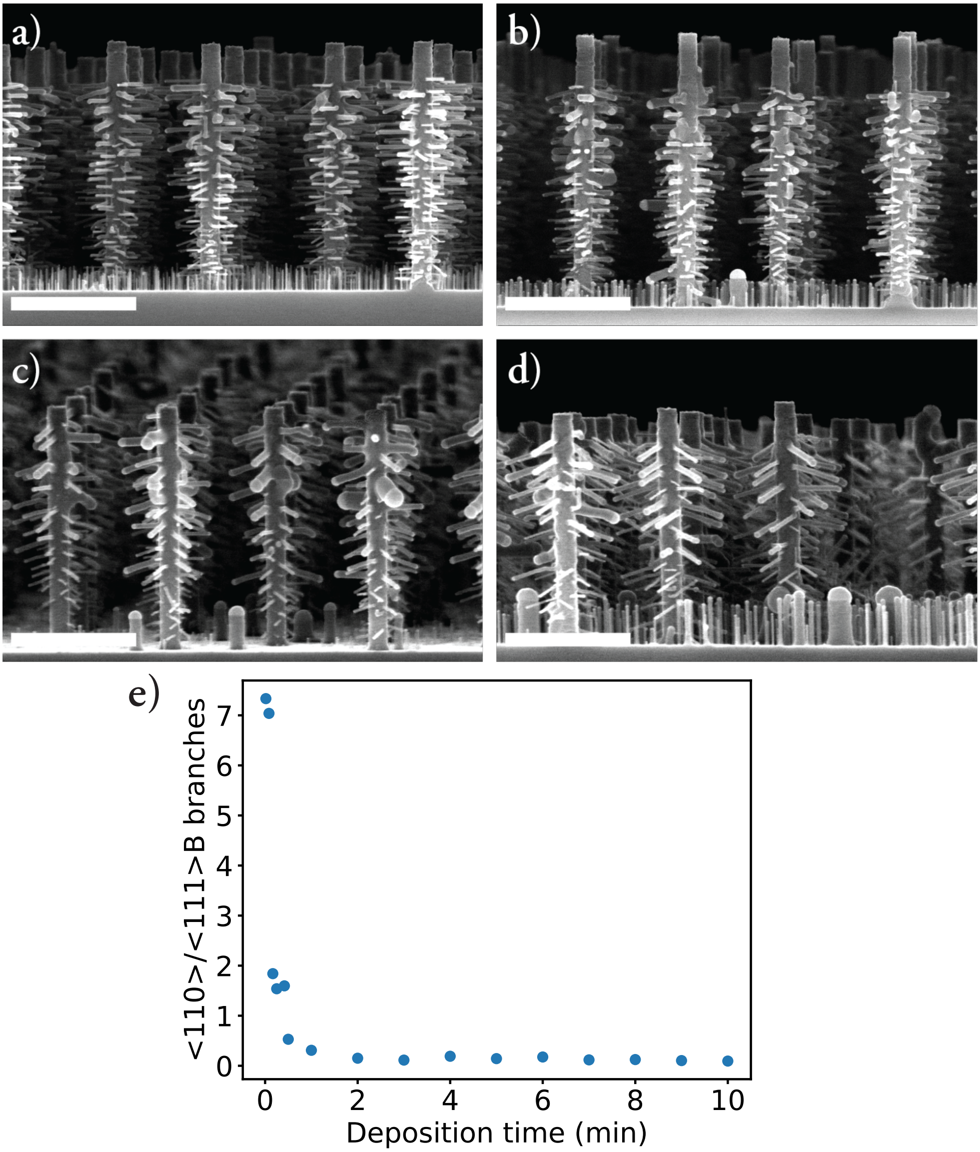

Figure 3.11: Cross-section SEM images of InP branches grown on samples with a Au deposition time of: a) 1 s, b) 15 s, c) 2 min, d) 10 min. The scale bar is 1 μm. e) The ratio of branches growing in the ⟨110⟩ and ⟨111⟩B direction for different Au deposition times.

3.5.2 Heterostructure trees

The development of homostructure trees explored the feasibility of the growth method, but to make CCDI LEDs, heterostructures need to be implemented where the core and the branches have a different bandgap. We have demonstrated the growth of heterostructures on $Ga_xIn_{1-x}P$-$Ga_yIn_{1-y}P$ where x>y. To grow the ternary combination, TEGa was used as the precursor for Ga. The branches have a typical diameter between 10 to 50 nm. The ternary $Ga_xIn_{1-x}P$, where x denotes the amount of Ga content and (1-x) the In content, has a tuneable bandgap. In the case of pure InP, where x = 0, the bandgap is 1.34 eV and it can be increased up to 2.25 eV where x = 1 and the structure is pure GaP. To grow the structures, we aimed towards high Ga content cores but without going over the indirect bandgap transition, such that both cores and branches have a direct bandgap. Figure 3.12 (a) shows a plot of the XRD measurements from the array of core NWs. The peak at 26.28° comes from the InP substrate in which the array is grown and the two peaks at 27.34° and 27.53° originate from the *in*- and *p*-segment of GaInP, respectively. This resulted in $Ga_xIn_{1-x}P$ with a composition between x = 50 to x = 60. Having a high Ga content in the cores provided a high degree of freedom in the parameter space of the branches. We have grown branches of different compositions by varying χ_{TEGa} (Paper II) and n-doped branches with a fixed χ_{TEGa} and variable dopant χ (Paper III). The precursor used for doping was hydrogen sulphide (H_2S). In Figure 3.12 (b)-(c) a representative SEM image of intrinsic branches is shown for the lowest and highest χ_{TEGa} used and in Figure 3.12 (d)-(e) a representative SEM image of doped branches is shown for the lowest and highest χ_{H2S}. In Figure 3.12 (b), InP branches were grown. The growth conditions for these branches were not optimal, leading to a poor surface and very few grown branches. Growth of InP on GaP is known to be difficult leading to kinked NWs [162]. The doping of the branches strongly influences the growth dynamics [33, 163]. In Figure 3.12 (f) a TEM micrograph of the connection between a core and branch is shown. A noticeable feature is the propagation of the lattice planes from the cores to the branches, signifying that the branches are grown epitaxially [156].

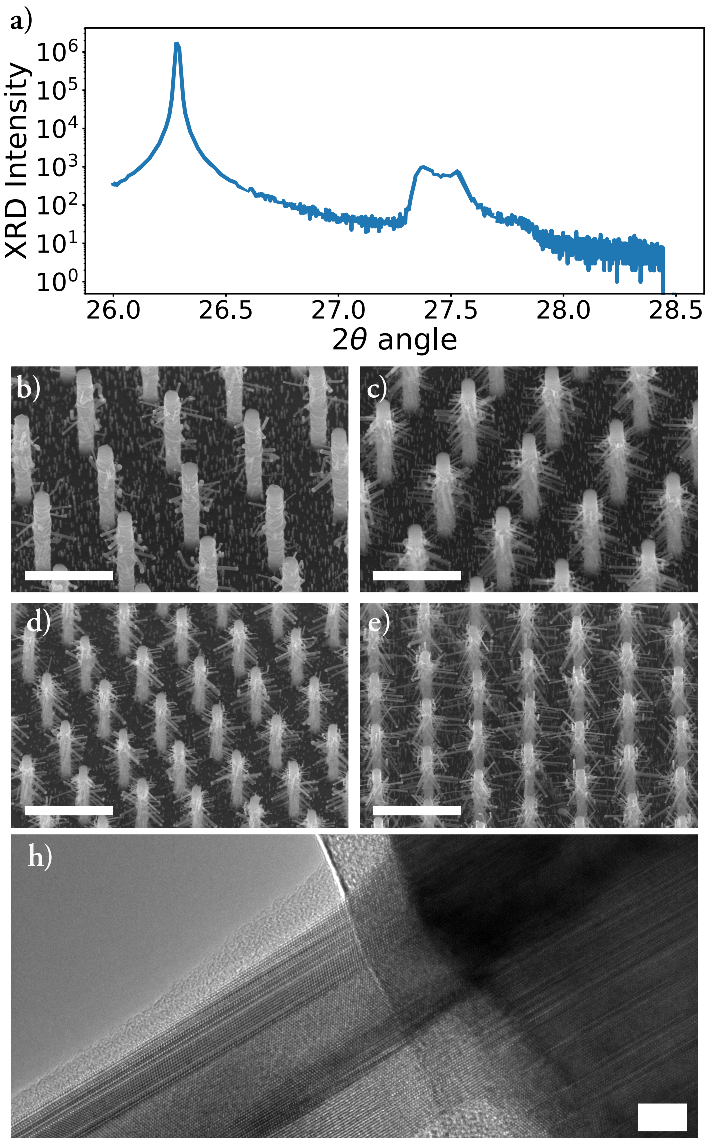

Figure 3.12: a) XRD intensity as a function of the 2θ scattering angle of the GaInP cores. The peak at 26.28° corresponds to the InP substrate and the peak from 27.34° to 27.53° corresponds to the GaInP cores. b)-c) GaInP branches grown with χ_{TEGa} of 0 and $5.97 \cdot 10^{-5}$, respectively. d)-e) n-doped GaInP branches grown with χ_{H_2S} of $3.17 \cdot 10^{-7}$ and $1.47 \cdot 10^{-6}$, respectively. The scale bar is 1 µm. f) TEM image of the connection between the core and a branch showing the propagation of lattice planes. The scale bar is 6 nm.

4 Processing and Characterisation of Nano-Tree LEDs

Let there be $\partial_\mu \partial^\mu F^{\alpha\beta} = 0$

This chapter brings to fruition the work initiated in Chapter 3. The chapter starts by introducing a detailed workflow of fabricating NW devices of different sizes. The finished devices are characterised by several methods to extract quantitative information. Each method is presented with a short introduction to the tool coupled with device measurement results and analysis.

4.1 Device Fabrication

Growing the structure is the first aspect of making an LED, but to be able to characterise and evaluate the performance of the developed structure, devices must be processed and measured. We have already touched upon the fact that we want to connect thousands of NWs to make devices. A single NW, albeit it can emit light, is impractical as the light emitted from it is not sufficient. To start with as-grown NWs and finish with devices where thousands of NWs are connected, several fabrication steps are needed. The samples are processed by using standard nanofabrication techniques in the cleanroom. The end purpose of fabricating a device is to put electrical contacts to afterwards bias the device. In our case, only the top contact is necessary to be fabricated, as the back side of the sample serves as the other contact. The processing steps described below make it possible to have many devices of different active region areas in a single sample. To help the reader follow the process, Figure 4.1 presents in three columns a schematic of the most important processing steps along with two SEM images, one in top view and the other in a cross-section view.

The first step (Figure 4.1 (a)-(c)) is to coat the NWs with a protective layer of an insulating material. This protective layer serves to prevent NW damage throughout the processing steps and separate the top and bottom contact such that there is no short circuit. The insulating layer is ~30 nm of silicon oxide (SiO_x) which is deposited using atomic layer deposition (ALD). The precursors used in the reaction are trimethylaluminium (TMAl) and tri(tert-butoxy)silanol (TTBS). The presence of TMAl leads to trace amounts of Al being incorporated in the SiO_2, which results in a not entirely stoichiometric composition, hence we use the abbreviation SiO_x [164]. A secondary intended effect of using SiO_x is to passivate the surface of the NWs and reduce the nonradiative recombination [165].

To be able to contact the tips of the NWs, the SiO_x needs to be removed selectively. This is done by first embedding the NWs in S1818 photoresist. At first, the photoresist fully covers the NWs. To reveal only the tips, a UV flood exposure is done, followed by the development of the photoresist and hard baking to ensure that the photoresist is not removed in subsequent processing steps. The SiO_x is then removed via RIE. Figure 4.1 (d)-(f) illustrates the sample after SiO_x etching.

The next processing steps rely heavily on UV lithography. UV lithography was mentioned above and in the previous chapter in the context of performing a flood exposure on the sample. UV lithography however is much more versatile than a simple flood exposure. The technique is of high importance in the semiconductor industry, where one can mention the world leader in UV lithography, ASML, which dominates the market with its lithography machines. A physical mask made of chromium is patterned with the desired structure to fabricate. Since fabrication steps consist of using several masks, alignment markers are also designed in each mask to ensure the correct overlapping of the features. The tool utilised for this type of UV lithography is called a mask aligner. In each UV lithography step, the sample is embedded in a new layer of photoresist prior to exposure. Photoresists can be classified largely into two main categories: positive and negative photoresist. When using a mask to perform UV lithography, the exposed area of the photoresist by UV light changes its properties. A positive photoresist will become soluble in a developer and dissolve, while a negative photoresist goes through a process called cross-linking, becoming harder to dissolve. The device processing in this work (Paper II & III) consists of three lithography exposures. After opening the tips of the NWs, we proceed with the device area definition in the first lithography step. Within the device area, the active region is located. The sample is embedded in S1828, exposed, and developed. Finally, it undergoes a hard baking process to preserve the pattern. Figure 4.1 (g)-(i) illustrates the process of defining the device area. In Figure 4.1 (g), the schematic illustrates a NW of the device area embedded in photoresist, and the NW adjacent to it which is part of the active region is exposed. Figure 4.1 (h) shows the top view of a device area and its active region of 100×100 μm^2. In Figure 4.1 (i), the cross-section SEM image shows the interface between the exposed NWs of the active region and the NWs of the device area embedded in S1828.

The next step is to coat the sample with a conductive material such that the NWs within the active region are all connected. The conductive material cannot be a metal however, as it would reflect the emitted photons. We use indium tin oxide (ITO) instead, which is a transparent conductive oxide. The ITO is deposited on the sample via sputtering. The sputtering process covers the entire sample in ITO, even the regions outside the device areas. To separate the devices from each other, the ITO needs to be removed in the areas between the devices. This is done in the second lithography step. The sample is embedded in S1813 and after UV lithography, the photoresist is developed and the areas outside of the devices are exposed. ITO is then etched in a mixture of $HCl:H_2O$ (1:2). Figure 4.1 (j) and (k) show a schematic after ITO sputtering and top view SEM image of a device after ITO etching, while in Figure 4.1 (l) and (m) we can observe in cross-section SEM images the NWs of the active region covered in ITO and the NWs outside the device area where the ITO has been etched away, respectively. The remainder of S1813 is dissolved in acetone after ITO etching.

The last step is to define the top metal contact (Figure 4.1 (n)-(p)). A mixture of titanium (Ti) and Au is used as a top contact and is evaporated on top of the ITO. For the UV lithography step to define the contacts a negative photoresist is used. A negative resist provides the advantage of an easier lift-off procedure after metal evaporation because of its undercut profile. Similarly to the previous two lithography steps, the sample is embedded in the negative photoresist, ma-N 490 in this work, is exposed with UV light and developed. An electron-beam evaporator is used for the metal contact. The method provides a uniform covering of the sample with metal. However, we are only interested in having Ti/Au on top of the devices. To remove the excessive metal, we finish the processing with a lift-off step. During lift-off, the photoresist is dissolved in acetone, which also causes the excess metal to be removed. The top and side view of a finished device are presented in the SEM images of Figure 4.1 (o) and (p). To get a better view, in Figure 4.2 (a) the active region, ITO and Au contact are highlighted in one of the fabricated devices. Figure 4.2 (b) shows the full sample, which is divided into four quadrants, each of them having several devices with active regions of 100×100, 200×200, 400×400, and 800×800 μm^2.

Apart from relying on a mask aligner to perform UV lithography, a new method that is picking up speed in industry is the maskless aligner, or laser writer (not to be confused with electron beam lithography which is also another type of maskless lithography). Compared to standard UV lithography, it offers the possibility to design and tweak effortlessly the schematics. Instead of having to fabricate a new physical mask every time a variation is made in the schematic, one can simply use a computer-aided design (CAD) software to draw the schematic, feed it to the machine and print the desired structure. We have used the maskless aligner MLA-150 which has a resolution of ~1 μm to test several new designs. Figure 4.3 illustrates two designs that have been tested. In Figure 4.3 (a), a photograph of the sample after finishing the fabrication procedure is shown. The variations that we have performed are to fabricate devices with an active region smaller than 100×100 μm^2 and define the Au contact all around the device area to compare the performance with the devices that have the Au contact only on one side. Figure 4.3 (b) shows an SEM image of the device with the smallest active region of 10×10 μm^2. In Figure 4.3 (c), a photograph of the second sample after fabrication is shown. In this configuration, the purpose is to utilise the entire sample as one LED. The sample is divided into smaller cells of 100×100 μm^2 active regions, all connected via Au metallisation. Figure 4.3 (d) shows an optical microscope image of the sample where several interconnected cells are noticeable.

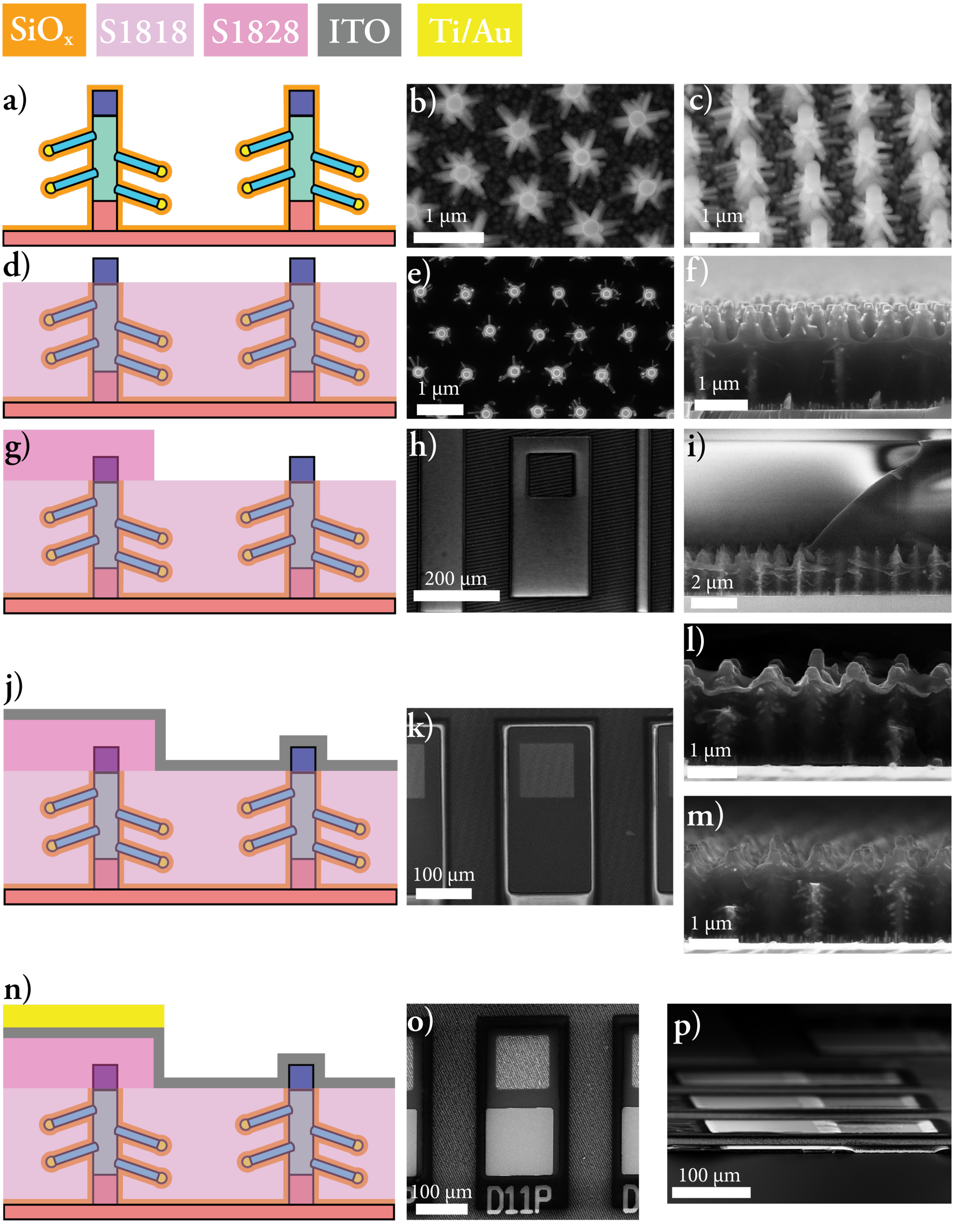

Figure 4.1: a) ALD coating with SiO$_x$ of the nanotrees. b)-c) Top and 30° tilt SEM images of the nanotrees after coating with SiO$_x$, respectively. d) Selective SiO$_x$ etching from the tips of the nanotrees. e)-f) Top and cross-section SEM images of the nanotrees after SiO$_x$ etching, respectively. g) Device area definition. h)-i) Top and cross-section SEM images after defining the device area, respectively. j) The device after ITO sputtering. k) Top view SEM image of a device after etching the ITO outside the device area. l)-m) Cross-section SEM images of the nanotrees inside the device area covered in ITO, and the ones outside where the ITO is etched, respectively. n)-p) Contact metal evaporation, top and cross-section SEM images of a device, respectively.

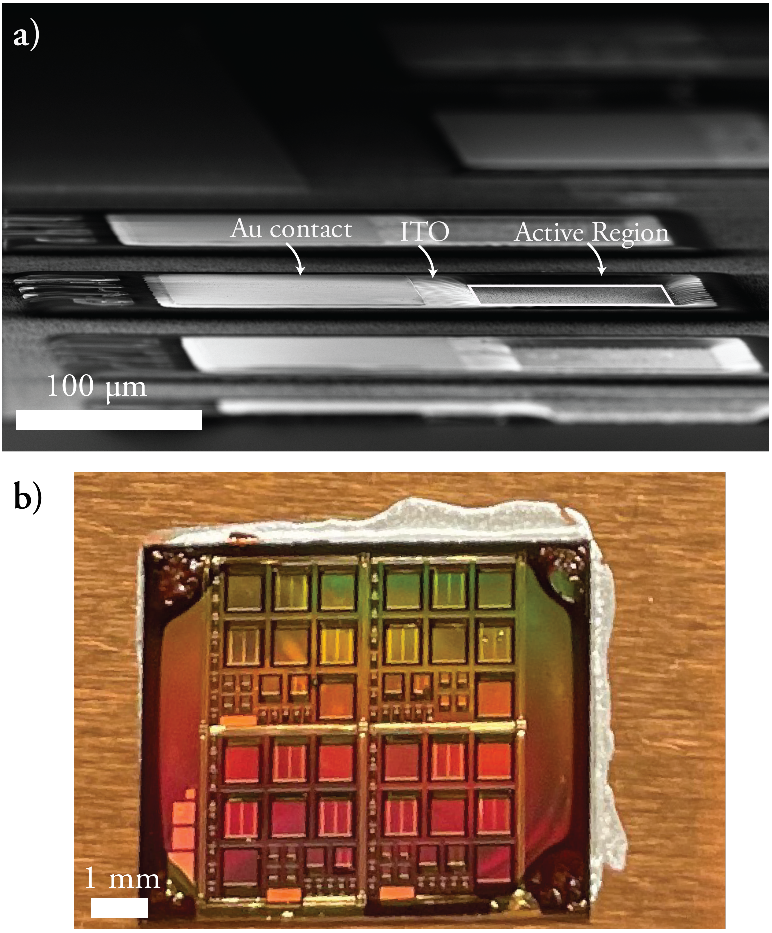

Figure 4.2: a) SEM image of a finished sample where the active region, ITO and Au contact are highlighted for illustration. b) Photograph of a finished sample, fixed by silver paste onto a Cu plate prior to characterisation measurements. Devices with different active region areas can be recognised in the photograph.

4.2 Electrical and Optical Characterisation

The device performance is initially verified by performing current-voltage (I-V) measurements. The sample is fixed on a Cu plate as shown in Figure 4.2 (b), where the Cu plate is connected to the back side of the sample. The measurement is performed in a probe station using a two-probe configuration, one for the back contact and the other probe is contacted to the evaporated metal contact on top of the device. Figure 4.4 shows an I-V curve measurement of a 100×100 µm^2 device, which has approximately 11500 NWs connected in parallel, showing an exponential relationship which is a clear diode behaviour. It must be noted that the reported current density in the plot is with respect to the total area of the active region and not only the fraction covered by the NWs. To evaluate the ideality factor n of the diode a fitting is done to the ideal diode equation:

$$n = \frac{e}{kT}\left(\frac{d(\ln I)}{dV}\right)^{-1} \tag{4.1}$$

The inset in Figure 4.4 shows a semilog plot of the I-V relationship used to extract the ideality factor. The ideality factor of the device is about 2.82. Above current densities of 0.1 mA/cm^2 we can observe a deviation from the exponential behaviour. This is indicative of the onset of resistive losses. Substantial contribution to the high resistive losses is attributed to the poor contact with ITO and its high sheet resistance. As we shall see below, there is significant non-uniformity in the light emission of the devices because of the ITO's sheet resistance. Another factor to consider is to take into account the high current applied to the device. For example, a 30 mA current corresponds to 2.6 µA of current flowing through every NW or a current density of 13 kA/cm^2, which leads to heating of the NWs and an increase in resistive losses.

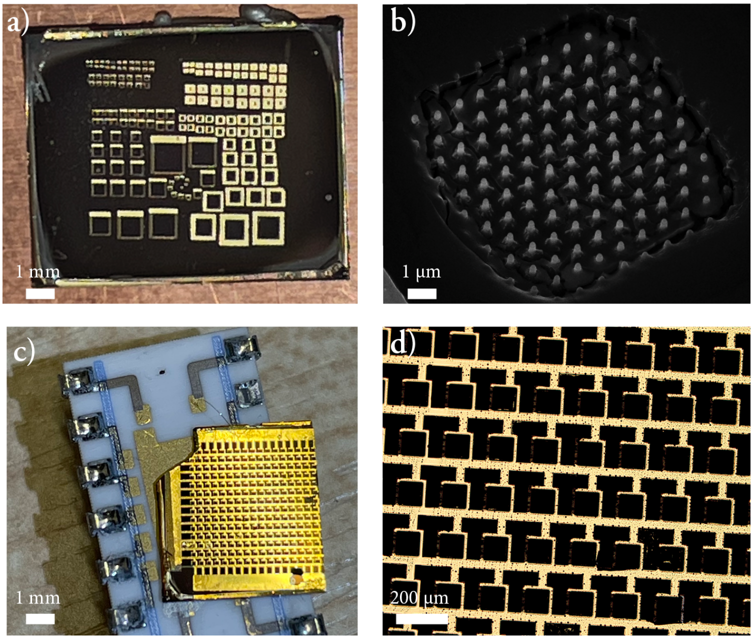

Figure 4.3: a) Photograph of a fabricated sample using MLA with varying active region areas from 10×10 µm^2 to 1×1 mm^2. Half of the sample has devices with a metal contact only on one side of the device area, and the other half has the metal contact defined all around the device area. b) An SEM image of the smallest device with an active region of 10×10 µm^2. c) Photograph of the fabricated sample containing a plurality of 100×100 µm^2 active region area devices connected together. d) An optical microscope image showing a zoomed-in image of c).

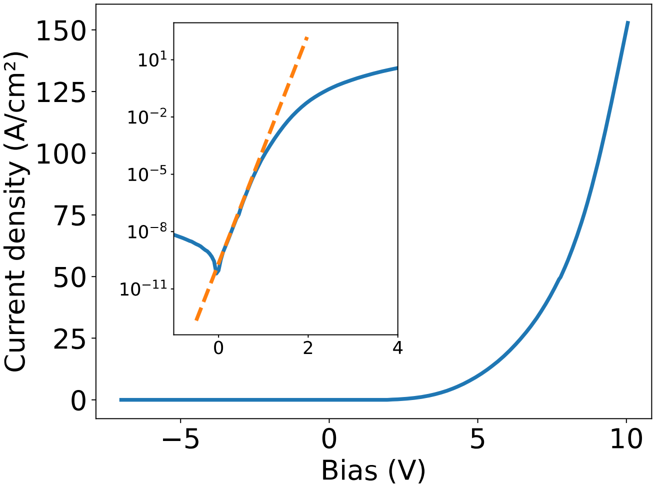

Figure 4.4: The I-V characteristic of a nanotree LED device. The device shows a rectifying behaviour. The inset shows a semi-log plot of the I-V curve to extract the ideality factor. The region fitted is shown with the dashed orange line.

We now turn our focus to the optical characterisation of our devices. Apart from obtaining working diodes, we want to demonstrate that the concept of CCDI LEDs is feasible in NWs. To show proof of concept we rely on electroluminescence (EL) measurements. The setup comprises of a stage where the Cu plate with devices is placed on and two probes to bias the devices. Above the stage, there is a microscope lens connected to an optical fiber which is used to collect the light and send it to a spectrometer. In Paper II, we fabricated a reference sample with only core NWs and five nanotree samples with varying χ_{TEGa} in the branches. Figure 4.5 shows the EL spectra of the reference and nanotree devices and Figure 4.6 highlights several pictures of the devices under operation showcasing the light emission. A common trend for all the devices is that illumination is observable to the eye only above an applied bias of ~5 V (Figure 4.6 (a)), which further supports the result that we suffer from high resistive losses. Additionally, as shown in Figure 4.6 (b)-(f) we have observed in an optical microscope that when biasing a device, the illumination is not uniform throughout it. There is a clear gradient in the emission, it being stronger near the interface with the Au contact. This is caused by the high sheet resistance of the ITO. In Figure 4.5 (a) we measured the spectrum of the reference device under different current bias ranging from 3 mA to 30 mA. We can observe a single peak at 1.91 eV coming from the core NWs. The energy of the emission agrees with the XRD results shown in Figure 3.12 (a), with the cores having a composition of approximately $Ga_{0.52}In_{0.48}P$. In Figure 4.5 (b) a representative EL spectrum under different applied bias of a nanotree device is shown. We can distinguish the appearance of two main peaks, one at 1.51 eV and one at 1.91 eV. The peak at 1.91 eV emerges from the core NWs similar to the reference sample, but the peak at lower energy originates from the branches, demonstrating the proof of concept of CCDI LEDs in the nanotree structure. Under a small current bias of 5 mA, the emission from the branches is higher than the cores, and with an increased bias the core peak starts to dominate. We can distinguish several other features in the spectra. In comparison to the core peak which has a narrow full-width half maximum, indicating uniform composition, the peak from the branches is much broader. The broadness of the branch peak indicates a larger composition variation among the branches. As they are distributed along the NW core, their composition can greatly vary. One could measure their composition in TEM-EDX, but being that transferring the NWs to a TEM grid is a destructive method, many of the branches break, making it difficult to precisely ascertain their composition. By increasing the current bias from 5 to 30 mA, we have observed that the core peak broadens and forms a shoulder leading to light emission in higher energies. The broadening extends to energies above 2.5 eV, which signifies that our complete emission spectrum encompasses the full visible spectrum and that we obtain white light. The white emission can be seen in the microscope images of Figure 4.6 (b)-(f) and a photograph of four LED devices in operation in Figure 4.6 (g) showcasing bright white light. The most plausible explanation for achieving white emission is state filling and population of higher conduction bands.

Figure 4.5 (c) shows the plot of the normalised EL spectra, focused only on the energy range of the branch emission. By increasing χ_{TEGa} the branch peak shifts to higher energies, enabling the possibility to tune the emission wavelength by tuning the growth parameters. As we have shown in Paper II, the strength of the EL intensity of the branches is stronger the larger the difference in bandgaps between the cores and branches because the diffusion force is stronger. Another reason that could explain the decrease of the branch EL intensity is the increment of deep trap states with higher Ga concentration [166].

A question that may naturally arise to the reader is how do we know that the diffusion principle actually works? Perhaps part of the photons emitted from the cores are absorbed in the branches and re-emitted as lower energy photons. To provide further proof of the CCDI LEDs we have grown nanotrees with GaInP cores where the Ga content is above the indirect bandgap transition. Figure 4.5 (d) shows the EL spectrum of the indirect-direct material combination, where we can distinguish a single emission peak, corresponding to the branches.

To further study the nanotree emission characteristics, in Paper III we have introduced doping in the branches. We have n-doped the branches with H_2S and varied χ_{H_2S} for a fixed branch composition. We fixed the χ_{TEGa} to be $3.73 \cdot 10^{-5}$, which is the same molar fraction as the best-performing device from the undoped branches that we discussed above. In Figure 4.5 (e) a representative spectrum from the series of doped branches is shown. A prominent feature that is still present in this structure is the appearance of white light. In Figure 4.5 (f), we have plotted the branch peak energy with increasing χ_{H_2S}. We observe that the peak does not significantly shift to higher energies with doping, unlike what should be expected for this level of χ_{H2S}. Compared to previous research, the amount of χ_{H2S} used should have led to degenerate doping and the Fermi level being pushed into the conduction band, causing a Burstein-Moss shift [40, 167].

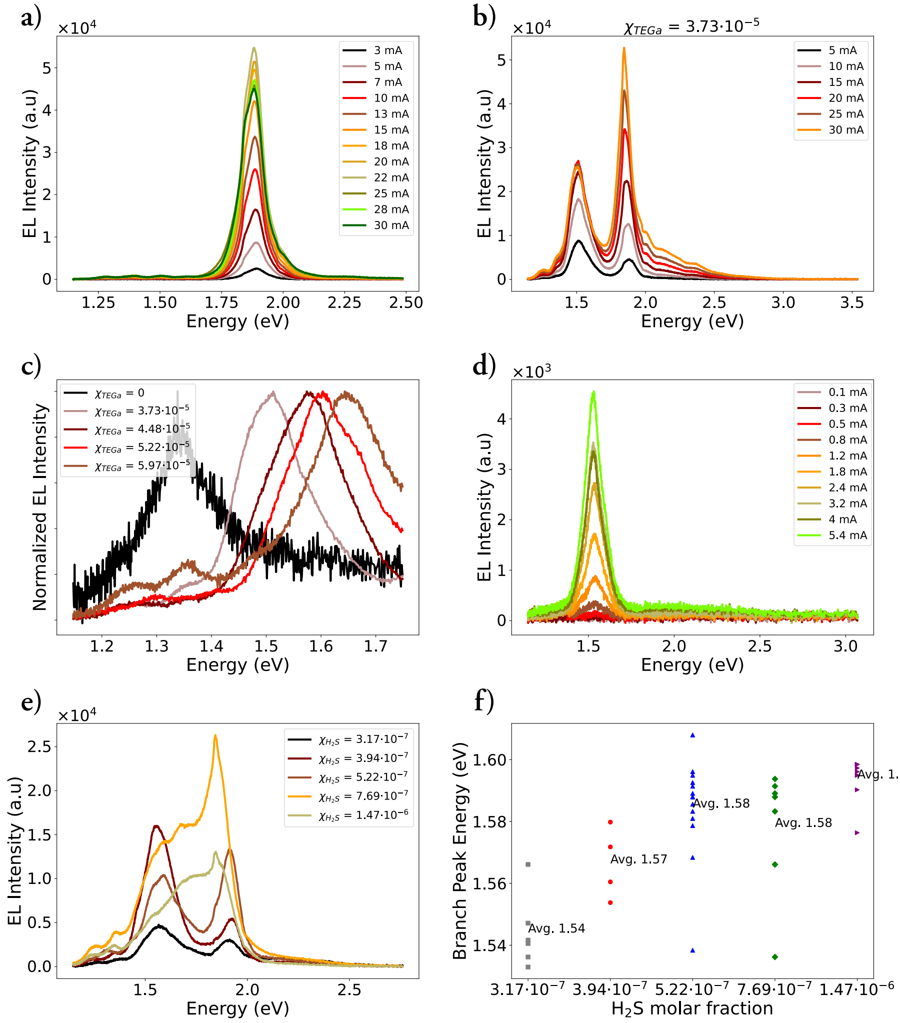

Figure 4.5: a) The EL spectrum of the reference device with only core NWs for different injected currents. b) The EL spectrum of a nanotree device with branches grown under $\chi_{TEGa} = 3.73 \cdot 10^{-5}$ for different injected currents. c) Normalised EL intensity of nanotree devices where the branches are grown under different χ_{TEGa}. d) The EL spectrum of a nanotree device where the cores have an indirect bandgap and the branches have a direct bandgap. A single peak of emission stemming from the branches is observed. e) The EL spectrum of nanotree devices with different χ_{H2S} in the branches. f) Branch peak energy under different χ_{H2S}. The inscribed numbers indicate the average peak energy in eV.

Lastly, to conclude this section, in Figure 4.6 (h), a photograph of the sample presented in Figure 4.3 (c) under operation is shown. It glows a bright red light under operation and opens the possibility of processing large area devices to make bigger LEDs for general lighting applications.

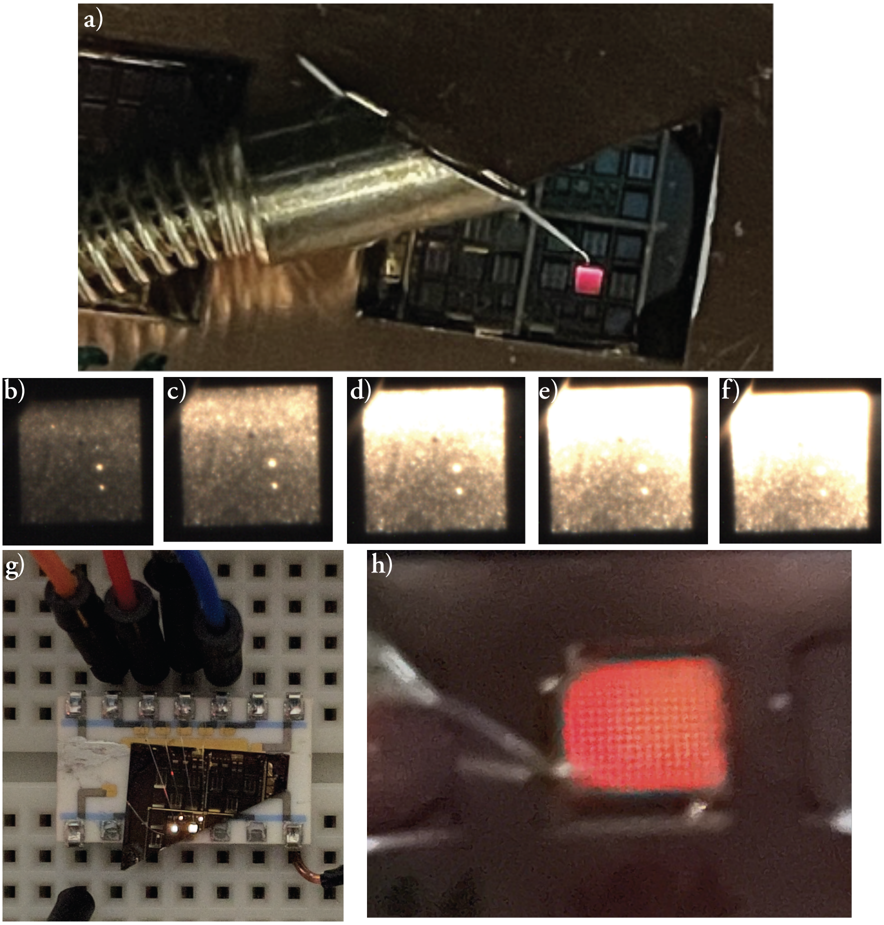

Figure 4.6: a) An 800×800 μm^2 nanotree device emitting red light under an applied bias. b)-f) Microscope images of a 200×200 μm^2 device with increased applied bias. The EL is not uniform throughout the device highlighting the problems with the ITO sheet resistance. g) 4 nanotree devices operating at the same time and emitting a bright white light. h) EL from a large sample with a plurality of 100×100 μm^2 active region area devices connected together to form an emissive area of 8×6 mm^2.

4.3 EQE, Radiometric & Photometric Characterisation

Integrating spheres are one the most common methods used to perform LED measurements and evaluate the performance of the device. Integrating spheres are hollow on the inside and are coated with a highly reflective material, such as barium sulphate or Teflon. The integrating sphere used in this work has a Teflon coating with 99% reflectance in the 300-1250 nm wavelength range [168]. The coating also ensures that the sphere acts as a diffusive Lambertian reflector and distributes the light homogeneously inside the sphere. Depending on the measurement protocol and construction of the sphere, the two variations of performing a measurement are called 4π and 2π. In a 4π setup, the device under test (DUT) is placed at the centre of the integrating sphere, while in a 2π setup there is an entrance port on the surface of the sphere to mount the DUT. Devices such as the one fabricated in this thesis are best measured in a 2π configuration since they also emit in a hemisphere, while light bulbs for example that are commonly found at home are best measured in a 4π configuration since they emit in all directions [169]. Figure 4.7 (a) illustrates a schematic of an integrating sphere. Light entering the integrating sphere undergoes multiple diffusive reflections, resulting in a constant irradiance inside the sphere. Given that the coating is not completely reflective, a fraction of the light is absorbed, which should be taken into account when evaluating the irradiance of the sphere. A final element that should be considered is the fact that the entrance and detector ports are physical openings, and the reflective properties are different as there is no coating present. As a rule of thumb, the total area of the ports should not exceed 5% of the sphere's area. The above considerations can be summarised together in an equation for the irradiance inside the integrating sphere [170]:

$$E = \frac{\Phi}{A_S} \frac{\rho}{[1 - \rho(1 - \sum_i f_i) + \sum_i \rho_i f_i]} \tag{4.2}$$

where Φ is the radiant flux of the DUT, A_S is the area of the integrating sphere, ρ is the reflection coefficient of the sphere, f_i is the fractional area of port i and ρ_i is the reflection coefficient of port i.

Although the surface of the sphere should perform as a perfect Lambertian reflector, in reality there will always be a small fraction of specular reflection occurring. More advanced setups than the one used in this work utilise components called baffles, which are placed in front of the detectors to prevent the effect of specular reflection and the direct beam from the DUT impinging on the detector. Our setup has a nozzle at the entrance port where the DUT is located to prevent direct light impingement. To mount the sample on the integrating sphere we designed a printed circuit board (PCB) that can be screwed at the entrance port (Figure 4.7 (b)-(c)). The sample is glued with a silver paste on a dual in-line (DIL) holder and wire bonded to the PCB pads.

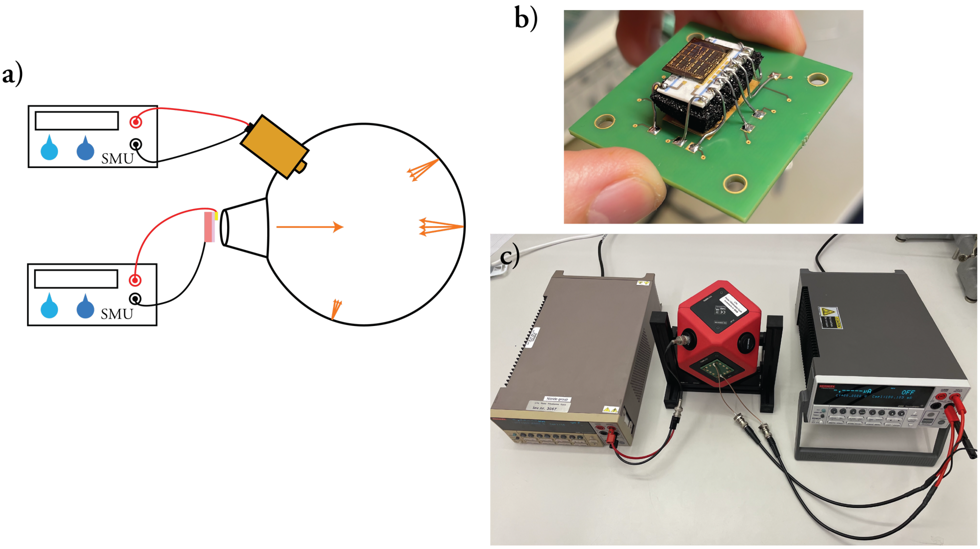

Figure 4.7: a) A schematic of the integrating sphere. The sample is placed at the entrance port and connected to a source measure unit (SMU) to bias it. A photodetector is located on one of the openings of the sphere and connected to an SMU to measure the photocurrent. b) The sample is bonded on a DIL holder and fixed on top of a PCB. c) A photograph of the setup. The PCB is screwed at the entrance port of the integrating sphere and connected to an SMU. The photodiode is connected to another SMU.

The EQE is calculated with the help of the integrating sphere. In the setup, it is not the EQE itself that is measured, but it is instead calculated, steps of which we will see below. According to equation 2.6, to calculate the EQE we need to know the radiant power of the LED, the photon energy, and the electron number. What we measure in the integrating sphere is the photocurrent generated in the photodiode. Because the photodiode is calibrated together with the sphere, the measured photocurrent correlates to the total amount of light emitted by the LED. The photocurrent (I_{PD}) is related to the detected power by the equation:

$$I_{\mathrm{PD}} = R \cdot \Phi \tag{4.3}$$

where R is the responsivity of the photodiode measured in A/W and is wavelength dependent, and Φ is the radiant power. If the source has a very narrow linewidth of emission, then equation 4.3 can be directly used. As we have seen in the previous section however, the spectra of the LEDs are very broad and instead of radiant power, one needs to use spectral radiant power $\phi(\lambda)$ measured in W/nm. Equation 4.3 then transforms into:

$$I_{\mathrm{PD}} = \int_{\lambda} R(\lambda)\phi(\lambda)d\lambda \tag{4.4}$$

$\phi(\lambda)$ is an unknown quantity to us since the spectrometer only gives the results in counts instead of W/nm, but we can derive a relation between the spectral radiant power and the radiant power by relying on the measured spectrum. We can construct a normalisation factor $P(\lambda)$, such that:

$$\int_{\lambda} P(\lambda) d\lambda = 1 \tag{4.5}$$

and

$$\phi(\lambda) = \Phi \cdot P(\lambda) \tag{4.6}$$

The normalisation factor is given as the ratio of the emission counts at wavelength λ ($S(\lambda)$), to the total emission counts (spectrum area). Hence:

$$P(\lambda) = \frac{S(\lambda)}{\int_{\lambda} S(\lambda) d\lambda} \tag{4.7}$$

By substituting equation 4.6 into equation 4.4, we can find the radiant power of the LED as:

$$\Phi = \frac{I_{\mathrm{PD}}}{\int_{\lambda} R(\lambda) P(\lambda) d\lambda} \tag{4.8}$$

Now that we have a relation to find the radiant power, we can derive a similar equation to find the average photon energy E_{γ}. We will use the same normalisation factor to weigh the wavelength of emission λ:

$$E_{\gamma} = \frac{hc}{\bar{\lambda}} = \frac{hc}{\int_{\lambda} \lambda P(\lambda) d\lambda} \tag{4.9}$$

By dividing equation 4.8 to 4.9 and substituting for $P(\lambda)$, we arrive at the formula for the generated photon number:

$$N_{\gamma} = \frac{\Phi}{E_{\gamma}} = \frac{I_{\mathrm{PD}}}{hc} \cdot \frac{\int_{\lambda} \lambda S(\lambda) d\lambda}{\int_{\lambda} R(\lambda) S(\lambda) d\lambda} \tag{4.10}$$

Now that we have derived equation 4.10, finding the EQE is simply dividing the photon number by the electron number N_{e}. The final equation thus reads:

$$EQE = \frac{N_{\gamma}}{N_{\mathrm{e}}} = \frac{I_{\mathrm{PD}} e}{hc I_{\mathrm{e}}} \cdot \frac{\int_{\lambda} \lambda S(\lambda) d\lambda}{\int_{\lambda} R(\lambda) S(\lambda) d\lambda} \tag{4.11}$$

Figure 4.8 (a)-(d) highlights the results from the undoped branches. In Figure 4.8 (a) the dependency of EQE with respect to the current density per NW (J/NW) in devices with an active region of 100×100 μm^2 for different χ_{TEGa} is shown. We can notice that the EQE is very low in all of our devices, on the order of $3 \cdot 10^{-4}$ %. With an increase in current density, we can also observe the effect of droop, which is typical in III-N for example once the injected current is high and Auger recombination starts to play a role [171, 172]. Among the different devices, the one with $\chi_{TEGa} = 3.73 \cdot 10^{-5}$ shows the highest EQE. Further investigating this device, in Figure 4.8 (b) we have shown the EQE-J/NW relationship by comparing the devices with different active region areas. The inset in Figure 4.8 (b) shows the EQE dependency with respect to the total injected current in the device for different active region areas. We can conclude that the larger the device area, the worse performing is the device. A big active region suffers more from the lower quality ITO compared to a small active region. As a comparison, current NW LEDs have demonstrated EQE values above 8% [173]. The detrimental effect of the ITO can also be observed in Figure 4.8 (c) where we have plotted the dependency of the input power to the radiant power for different branch compositions. A prominent feature is that the input power is on the order of a fraction of a Watt, but radiated power is around 100 nW, which for the moment is very little output power. In Figure 4.8 (d), we compare the radiant power with respect to the input power for different active region areas. The results support that the sizes of interest for further work should be 100×100 μm^2 and below.

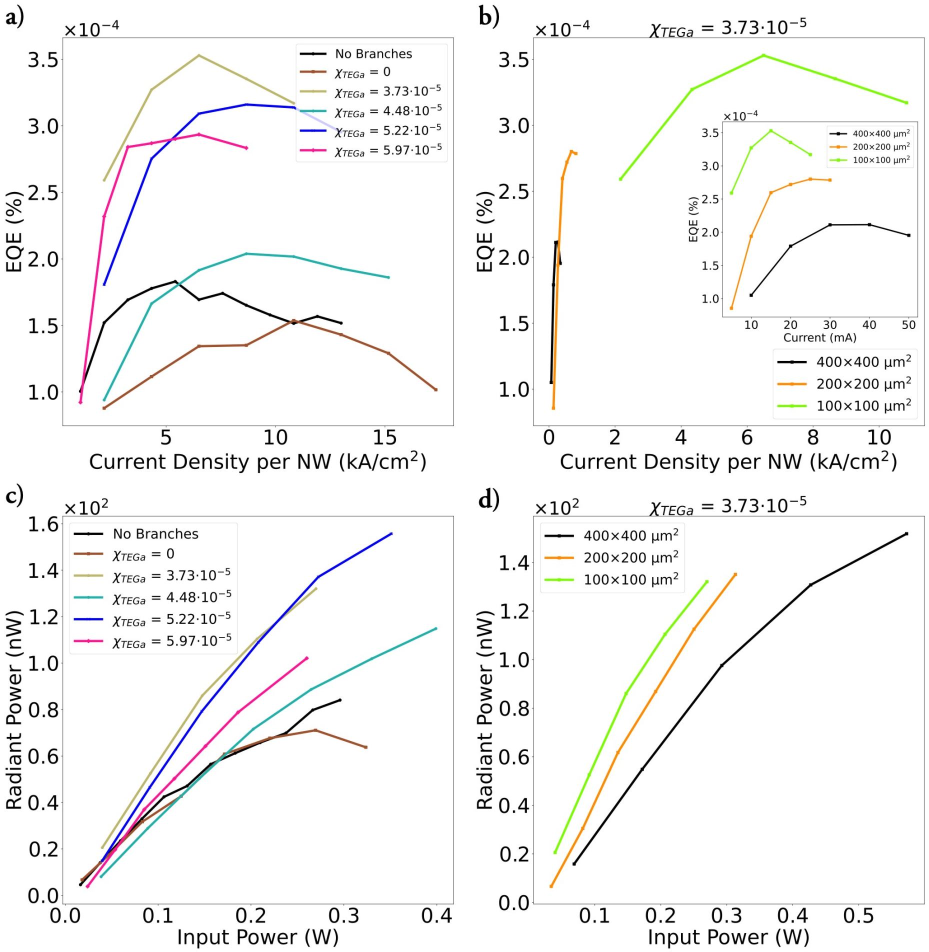

Figure 4.8: a) EQE-J/NW relationship of 100×100 μm² devices without branches and with different χ_{TEGa} grown branches. b) EQE-J/NW relationship for different active region areas, where χ_{TEGa}=3.73·10^{-5}. The inset compares the devices with respect to the total injected current. c) Radiant Power – Input Power relationship of 100×100 μm² devices without branches and with different χ_{TEGa} grown branches. d) Radiant Power – Input Power relationship for different active region areas, where χ_{TEGa} = 3.73·10^{-5}.

Similarly, in Figure 4.9 (a)-(d) we highlight results from the n-doped branches. The current results do not show any improvement in the efficiency or amount of emitted light. Comparing Figures 4.8 and 4.9, the average EQE between the differently doped samples is similar to the undoped samples. Apart from the lowest doped branches, there is a trend of the devices having a lower radiant power with increased doping concentration. One of the possible reasons for this behaviour is a deterioration of the branch quality with increased doping concentration. The growth conditions alongside the processing might need to be further improved to increase the amount of radiated power.

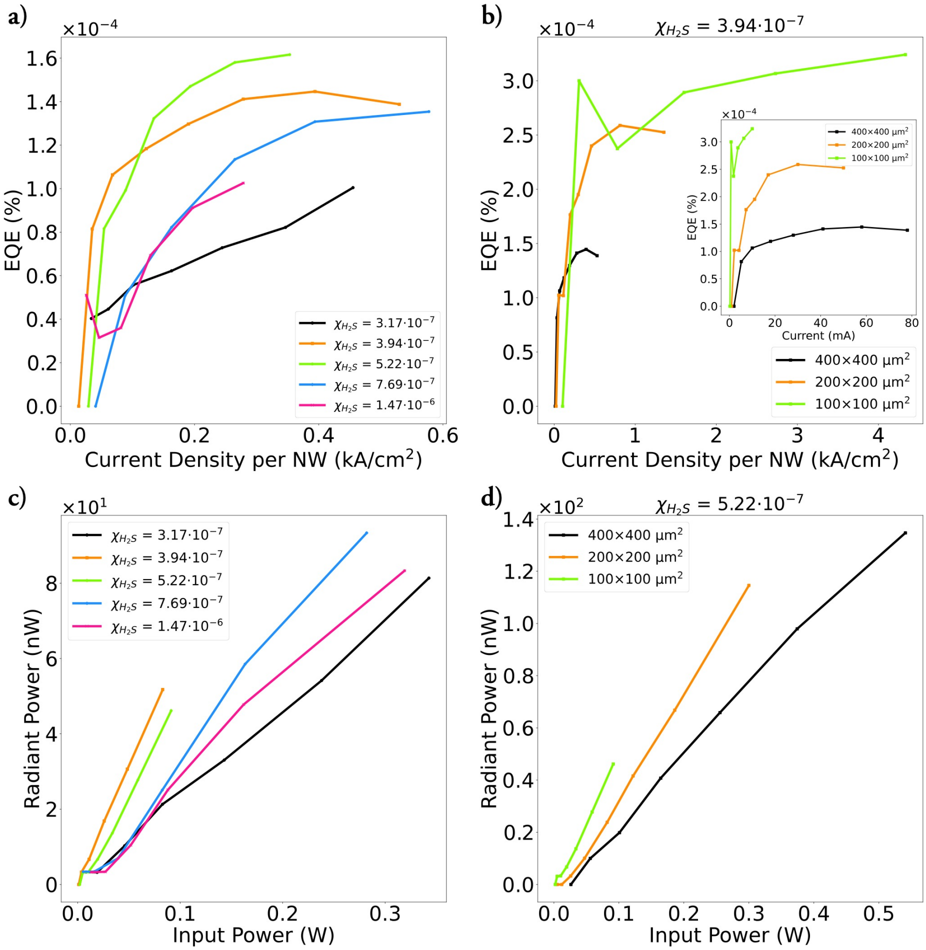

Figure 4.9: a) EQE-J/NW relationship of 400×400 μm^2 devices with a varying χ_{H2S}. b) EQE-J/NW relationship for different active region areas, where $\chi_{H2S} = 3.94 \cdot 10^{-7}$. The inset compares the devices with respect to the total injected current. c) Radiant Power – Input Power relationship of 100×100 μm^2 devices with a varying χ_{H2S}. d) Radiant Power – Input Power relationship for different active region areas, where $\chi_{H2S} = 5.22 \cdot 10^{-7}$.

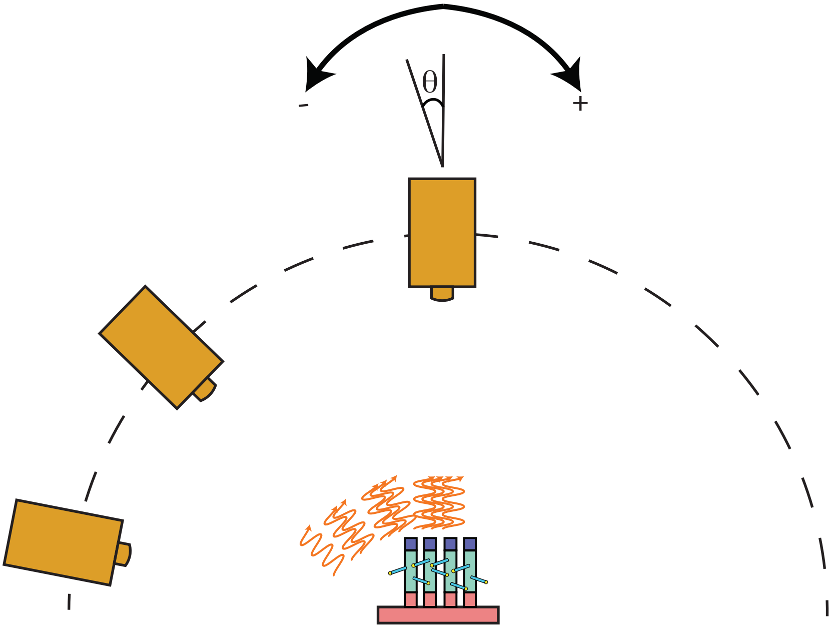

Figure 4.10: A schematic of the goniometer setup. The sample is placed at the centre of rotation of the photodiode. The photodiode is moved from -90° to +90° to collect the light at different angles and measure the radiation pattern.

After evaluating the EQE of our structures, we can continue to quantify information such as the radiance and luminance of the LEDs. Radiance and luminance strongly depend on the radiation pattern of the device. The common case for solid state LEDs is that they emit in a Lambertian pattern, where the radiant intensity changes with cosθ with respect to the forward direction. By implementing different designs, such as the integration of an aluminium (Al) light reflector on a substrate with NWs [174], one can tailor the radiation pattern to have light focused more in the forward direction. OLEDs for example are a typical case where the radiation pattern deviates from being Lambertian [175, 176].

To characterise the radiation pattern of the LEDs we built a simple goniometer setup, a schematic of which is shown in Figure 4.10. In our goniometer setup, a photodiode is mounted on a moving handle while the sample is kept fixed on a stage and centred on the axis of rotation of the photodiode. The radiation pattern is scanned from -90° to +90° in steps of 5° by moving the photodiode. We measured the produced photocurrent and normalised the data with respect to the measured photocurrent at 0°, perpendicular to the device. In Figure 4.11 we can observe the radiation pattern of our devices with and without branches and how they compare to the Lambertian radiation pattern. The data points closely match a Lambertian radiation pattern.

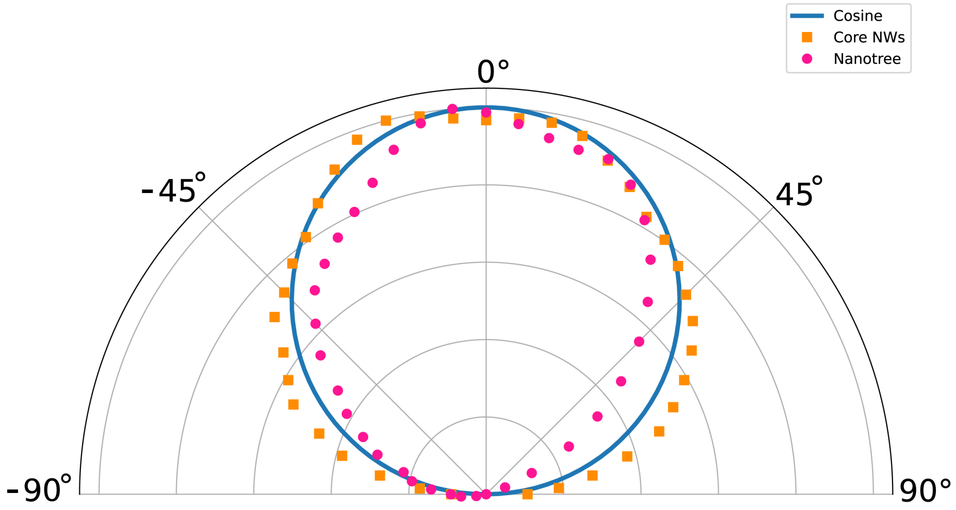

Figure 4.11: The measured radiation pattern of devices with only core NWs (orange) and nanotree devices (pink). The blue solid line represents the theoretical Lambertian cosine radiation pattern.

Other types of goniometer setups include the replacement of the photodiode with a photometer instead and coupled with a complementary spectrometer to perform high quality gonio-spectroradiometric measurements. In such a setup the irradiance is measured as a function of the spherical coordinate angles θ and φ and integrated to find the total radiant power. It is the most accurate measurement that can be performed but it is on the other hand very time-consuming [105]. In the case of a Lambertian emitter, the radiant power is given by:

$$\Phi = \int I_0 cos\theta d\Omega = \int I_0 cos\theta sin\theta d\theta d\phi = \iint_{0\,0}^{2\pi\,\pi} I_0 cos\theta sin\theta d\theta d\phi = \pi I_0 \tag{4.12}$$

where I_0 is the radiant intensity in the perpendicular direction. By using the equation for radiance from Table 2.1 and equation 4.12, we can derive the radiance of a Lambertian source as:

$$R = \frac{I(\theta)}{Acos\theta} = \frac{I_0}{A} = \frac{\Phi}{\pi A} \tag{4.13}$$

Because of the very good agreement between our radiation pattern and the Lambertian radiation pattern we can make use of equation 4.13 to calculate the radiance of our devices, but to find the luminance we have to instead rely on the spectral radiance because of the broad emission spectrum. By applying equation 2.9, we can find the luminous power and the luminance of the source. Below we are going to derive the equations used in practice to evaluate these quantities. The luminous power is given by:

$$\Phi_{\mathrm{v}} = 683 \int \phi(\lambda) V(\lambda) d\lambda = 683 \cdot \Phi \int_{\lambda_{visible}} P(\lambda) V(\lambda) d\lambda \tag{4.14}$$

and the luminance:

$$L = \frac{\Phi_{\mathrm{v}}}{\pi A} = \frac{683 \cdot \Phi \int_{\lambda_{visible}} P(\lambda) V(\lambda) d\lambda}{\pi A} \tag{4.15}$$

Now that we have the set of formulas to evaluate the radiance and luminance, we can calculate the EQE-L, EQE-R and Φ_{v}-J. In Figure 4.12 (a)-(b), the EQE-R and EQE-L results are presented for undoped branches. Although the dependency between luminance and radiance differs only by a factor, the emission spectrum contains a bigger portion pertaining to the visible spectrum the higher the Ga concentration in the branches, so it is useful to evaluate both quantities. Comparing for example the results from the device with $\chi_{\mathrm{TEGa}} = 3.73 \cdot 10^{-5}$ and $\chi_{\mathrm{TEGa}} = 5.22 \cdot 10^{-5}$, the highest measured radiance is about 5 W/sr·m^2, while the luminance is 250 cd/m^2 and 430 cd/m^2, respectively. For comparison, the luminance of a standard dynamic range TV display is around 100 cd/m^2, that of a high dynamic range display between 1000-4000 cd/m^2, and state of the art µLEDs can go upwards of 10 million cd/m^2 [177]. Since luminance is a quantity that depends on the area of the device, we have calculated the luminous power and in Figure 4.12 (c) we have plotted the Φ_{v}-J results. On average, the devices emit around 10 µlm. The results further highlight the necessity to improve the device performance, since for general lighting applications the luminous power required is on the order of several hundred lm.

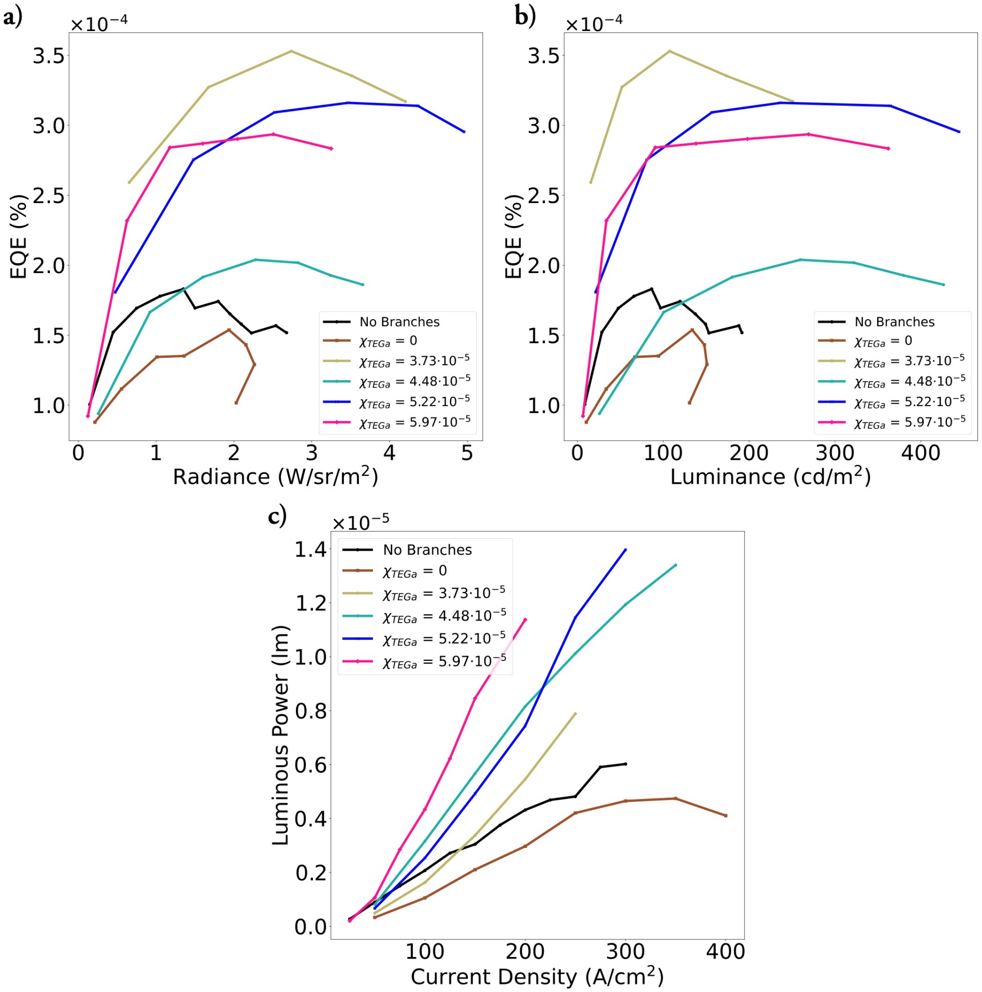

Figure 4.12: a) EQE-R relationship of 100×100 μm^2 devices without branches and with different χ_{TEGa} grown branches. b) EQE-L relationship of 100×100 μm^2 devices without branches and with different χ_{TEGa} grown branches. c) Luminous Power-J relationship of 100×100 μm^2 devices without branches and with different χ_{TEGa} grown branches.

5 Conclusions and Outlook

Punë, punë natë e ditë,
që të shohim pakëz dritë!
– Naim Frashëri

The work carried out in this thesis is a stepping stone to a brighter and better future. III-V NWs are an excellent platform for LEDs and the nanotree structures provide an alternative to realising high-efficiency and low-cost lighting fixtures.

In Paper I, we took an alternative route to aerosol particle deposition to supply the necessary Au seed particles on the core NW array for branch growth. We utilised an aqueous solution containing Au particles and made use of electroless deposition to realise a cost-effective deposition method. We explored the parameter space to tune the density and size of Au particles by varying the temperature and concentration of the solution, and the deposition time of particles. We explored the feasibility of growing branches by combining the same material (InP) as the core and branch material. It allowed us to examine the feasibility of the chosen Au deposition method. We demonstrated that branches can be grown along the entire NW length, with a high density of branches as compared to other methods, such as with aerosol Au particles. By varying the deposition time and then growing branches, we have observed a change in the growth direction of the branches from the normally occurring $\langle 111 \rangle$B direction in NWs to the $\langle 110 \rangle$ direction. We have attributed this change to the Cl^- ions that are present in the solution which can etch the native oxide around the core NWs.

To make LED devices with the nanotrees, we developed the growth of high bandgap GaInP cores and continued growing GaInP branches. We successfully showed in Paper II the first demonstration of CCDI LEDs in nanotrees, where two clear EL peaks could be distinguished corresponding to the cores and branches. We have shown peak shifting in the branches by tuning the Ga content in the branches. By increasing the applied bias, we could make the LEDs emit a bright white colour. This creates the possibility of producing white light emission without phosphor down-conversion within a single device. The field of phosphor-free white LEDs is relatively still in its infancy [178], and this architecture could be a new method to make white LEDs for general lighting.
We used an integrating sphere to calculate the EQE of the LEDs and although the value is very low, we have concluded that the underlying reason stems from contacting problems. In our LEDs, EL is detectable by the naked eye above 5 V of applied bias. This high value of bias needed to observe EL is attributed to the contact losses, where ITO is the most problematic contact, because of its high sheet resistance which leads to non-uniform current spreading in the NW array.

Lastly, in Paper III, we have taken the structure one step further and have started exploring the influence of doping the branches. The performance and efficiency of the devices is similar to the case of undoped branches, suggesting an immediate necessity to focus on improving contact resistance.

The future of this work contains many interesting possibilities. One key aspect of the nanotrees is that the structure can easily be applied to many different material combinations. This makes the concept very attractive to be adopted in III-N LEDs where it can be used in display applications. InGaN has already shown superior performance in the red compared to AlGaInP when the size of the device goes below 20×20 µm^2 [179]. Full solid state devices provide substantial advantages over phosphor colour conversion as they do have the capabilities to provide the high luminance required for applications involving µLED [180].

Two key challenges for the future of this work will be the improvement of contact resistance and the surface passivation of the nanotrees. As NWs have a high surface-to-volume ratio, this can lead to an increase in the nonradiative surface recombination rate. Future work will be focused on growing passivating shells in-situ using MOVPE to improve the surface quality of the active layer, make devices without a photoresist spacer to increase the LEE, and explore the possibility of changing the transparent conductive oxide from ITO to zinc oxide.

References

[1] BP. "Statistical Review of World Energy." https://www.energyinst.org/statistical-review (accessed 25/12/2023).

[2] U. Nations. "“The Paris Agreement”." https://unfccc.int/process-and-meetings/the-paris-agreement (accessed 25/12/2023).

[3] Z. I. Alferov, "The semiconductor revolution in the 20th century," *Russian Chemical Reviews,* vol. 82, no. 7, pp. 587-596, 2013.

[4] A. Nardelli, E. Deuschle, L. D. de Azevedo, J. L. N. Pessoa, and E. Ghisi, "Assessment of Light Emitting Diodes technology for general lighting: A critical review," *Renewable and Sustainable Energy Reviews,* vol. 75, pp. 368-379, 2017.

[5] G. Zissis, P. Bertoldi, and T. Serrenho, "Update on the Status of LED-Lighting world market since 2018," *Publications Office of the European Union: Luxembourg,* 2021.

[6] U. S. D. o. Energy. "Life-Cycle Assessment of Energy and Environmental Impacts of LED Lighting Products." https://www1.eere.energy.gov/buildings/publications/pdfs/ssl/lca_factsheet_apr2013.pdf (accessed 25/12/2023).

[7] C. Weisbuch, M. Piccardo, L. Martinelli, J. Iveland, J. Peretti, and J. S. Speck, "The efficiency challenge of nitride light-emitting diodes for lighting," *Physica status solidi (a),* vol. 212, no. 5, pp. 899-913, 2015.

[8] Signify. "Signify introduces Philips LED’s most energy-efficient A-class bulbs." https://www.signify.com/global/our-company/news/press-releases/2021/20210830-signify-introduces-philips-leds-first-most-energy-efficient-a-class-bulbs (accessed 25/12/2023).

[9] Z. Chen, S. Yan, and C. Danesh, "MicroLED technologies and applications: characteristics, fabrication, progress, and challenges," *Journal of Physics D: Applied Physics,* vol. 54, no. 12, 2021.

[10] Y. L. Chen, Z. T. Ye, W. Lai, C. C. Chiu, K. W. Lin, and P. Han, "Application of Mini-LEDs with Microlens Arrays and Quantum Dot Film as Extra-Thin, Large-Area, and High-Luminance Backlight," *Nanomaterials,* vol. 12, no. 6, 2022.

[11] T. Wu *et al.*, "Mini-LED and Micro-LED: Promising Candidates for the Next Generation Display Technology," *Applied Sciences,* vol. 8, no. 9, 2018.

[12] L.-D. Yuan, H.-X. Deng, S.-S. Li, S.-H. Wei, and J.-W. Luo, "Unified theory of direct or indirect band-gap nature of conventional semiconductors," *Physical Review B,* vol. 98, no. 24, 2018.

[13] S. Han *et al.*, "AlGaInP-based Micro-LED array with enhanced optoelectrical properties," *Optical Materials,* vol. 114, 2021.

[14] S. Zhao, H. P. T. Nguyen, M. G. Kibria, and Z. Mi, "III-Nitride nanowire optoelectronics," *Progress in Quantum Electronics,* vol. 44, pp. 14-68, 2015.

[15] F. K. Yam and Z. Hassan, "Innovative advances in LED technology," *Microelectronics Journal,* vol. 36, no. 2, pp. 129-137, 2005.

[16] S. N. S. Nakamura, "GaN growth using GaN buffer layer," *Japanese Journal of Applied Physics,* vol. 30, no. 10A, p. L1705, 1991.

[17] R. E. Algra *et al.*, "Twinning superlattices in indium phosphide nanowires," *Nature,* vol. 456, no. 7220, pp. 369-72, Nov 20 2008.

[18] R. E. Algra *et al.*, "The Role of Surface Energies and Chemical Potential during Nanowire Growth," *Nano Letters,* vol. 11, no. 3, pp. 1259-1264, 2011.

[19] E. Barrigón, L. Hrachowina, and M. T. Borgström, "Light current-voltage measurements of single, as-grown, nanowire solar cells standing vertically on a substrate," *Nano Energy,* vol. 78, 2020.

[20] A. Berg *et al.*, "Growth and characterization of wurtzite GaP nanowires with control over axial and radial growth by use of HCl in-situ etching," *Journal of Crystal Growth,* vol. 386, pp. 47-51, 2014.

[21] A. Berg, F. Lenrick, N. Vainorius, J. P. Beech, L. R. Wallenberg, and M. T. Borgström, "Growth parameter design for homogeneous material composition in ternary GaxIn1−xP nanowires," *Nanotechnology,* vol. 26, no. 43, 2015.

[22] M. T. Borgström, G. Immink, B. Ketelaars, R. Algra, and E. P. A. M. Bakkers, "Synergetic nanowire growth," *Nature Nanotechnology,* vol. 2, no. 9, pp. 541-544, 2007.

[23] M. T. Borgström *et al.*, "Precursor evaluation for in situ InP nanowire doping," *Nanotechnology,* vol. 19, no. 44, 2008.

[24] V. Dagyte, M. Heurlin, X. Zeng, and M. T. Borgstrom, "Growth kinetics of Ga(x)In((1-x))P nanowires using triethylgallium as Ga precursor," *Nanotechnology,* vol. 29, no. 39, p. 394001, Sep 28 2018.

[25] K. A. Dick, J. Bolinsson, B. M. Borg, and J. Johansson, "Controlling the Abruptness of Axial Heterojunctions in III–V Nanowires: Beyond the Reservoir Effect," *Nano Letters,* vol. 12, no. 6, pp. 3200-3206, 2012.

[26] L. Hrachowina, N. Anttu, and M. T. Borgström, "Wafer-Scale Synthesis and Optical Characterization of InP Nanowire Arrays for Solar Cells," *Nano Letters,* vol. 21, no. 17, pp. 7347-7353, 2021.

[27] J. Johansson *et al.*, "Structural properties of 〈111〉 B -oriented III–V nanowires," *Nature Materials,* vol. 5, no. 7, pp. 574-580, 2006.

[28] H. J. Joyce, J. Wong-Leung, Q. Gao, H. H. Tan, and C. Jagadish, "Phase Perfection in Zinc Blende and Wurtzite III–V Nanowires Using Basic Growth Parameters," *Nano Letters,* vol. 10, no. 3, pp. 908-915, 2010.

[29] S. Lehmann, J. Wallentin, D. Jacobsson, K. Deppert, and K. A. Dick, "A General Approach for Sharp Crystal Phase Switching in InAs, GaAs, InP, and GaP Nanowires Using Only Group V Flow," *Nano Letters,* vol. 13, no. 9, pp. 4099-4105, 2013.

[30] S. Lehmann *et al.*, "Simultaneous Growth of Pure Wurtzite and Zinc Blende Nanowires," *Nano Letters,* vol. 19, no. 4, pp. 2723-2730, Apr 10 2019.

[31] F. Lindelöw *et al.*, "Doping evaluation of InP nanowires for tandem junction solar cells," *Nanotechnology,* vol. 27, no. 6, 2016.

[32] E. K. Mårtensson, S. Lehmann, K. A. Dick, and J. Johansson, "Effect of radius on crystal structure selection in III–V nanowire growth," *Crystal Growth & Design,* vol. 20, no. 8, pp. 5373-5379, 2020.

[33] G. Otnes, M. Heurlin, X. Zeng, and M. T. Borgström, "InxGa1–xP Nanowire Growth Dynamics Strongly Affected by Doping Using Diethylzinc," *Nano Letters,* vol. 17, no. 2, pp. 702-707, 2017.

[34] L. Samuelson *et al.*, "Semiconductor nanowires for 0D and 1D physics and applications," *Physica E: Low-dimensional Systems and Nanostructures,* vol. 25, no. 2-3, pp. 313-318, 2004.

[35] M. Scheffler, S. Nadj-Perge, L. P. Kouwenhoven, M. T. Borgström, and E. P. A. M. Bakkers, "Diameter-dependent conductance of InAs nanowires," *Journal of Applied Physics,* vol. 106, no. 12, 2009.

[36] R. Sjökvist, M. Tornberg, M. Marnauza, D. Jacobsson, and K. A. Dick, "Observation of the Multilayer Growth Mode in Ternary InGaAs Nanowires," *ACS Nanoscience Au,* vol. 2, no. 6, pp. 539-548, 2022.

[37] M. Tornberg, C. B. Maliakkal, D. Jacobsson, K. A. Dick, and J. Johansson, "Limits of III–V Nanowire Growth Based on Droplet Dynamics," *The Journal of Physical Chemistry Letters,* vol. 11, no. 8, pp. 2949-2954, 2020.

[38] R. T. Velpula, B. Jain, H. Q. T. Bui, and H. P. T. Nguyen, "Full-Color III-Nitride Nanowire Light-Emitting Diodes," *Journal of Advanced Engineering and Computation,* vol. 3, no. 4, 2019.

[39] J. Wallentin *et al.*, "InP nanowire array solar cells achieving 13.8% efficiency by exceeding the ray optics limit," *Science,* vol. 339, no. 6123, pp. 1057-1060, 2013.

[40] J. Wallentin *et al.*, "Probing the Wurtzite Conduction Band Structure Using State Filling in Highly Doped InP Nanowires," *Nano Letters,* vol. 11, no. 6, pp. 2286-2290, 2011.

[41] J. Wallentin *et al.*, "Degenerate p-doping of InP nanowires for large area tunnel diodes," *Applied Physics Letters,* vol. 99, no. 25, 2011.

[42] M. Borg *et al.*, "Vertical III–V Nanowire Device Integration on Si(100)," *Nano Letters,* vol. 14, no. 4, pp. 1914-1920, 2014.

[43] K. Tomioka, M. Yoshimura, E. Nakai, F. Ishizaka, and T. Fukui, "Integration of III-V nanowires on Si: From high-performance vertical FET to steep-slope switch," in *2013 IEEE International Electron Devices Meeting*, 2013: IEEE, pp. 4.1. 1-4.1. 4.

[44] L. Hrachowina, Y. Chen, E. Barrigón, R. Wallenberg, and M. T. Borgström, "Realization of axially defined GaInP/InP/InAsP triple-junction photovoltaic nanowires for high-performance solar cells," *Materials Today Energy,* vol. 27, p. 101050, 2022.

[45] H. Jeddi, B. Witzigmann, K. Adham, L. Hrachowina, M. T. Borgström, and H. Pettersson, "Spectrally Tunable Broadband Gate-All-Around InAsP/InP Quantum Discs-in-Nanowire Array Phototransistors with a High Gain-Bandwidth Product," *ACS Photonics,* 2023.

[46] H. Jeddi *et al.*, "Gain and bandwidth of InP nanowire array photodetectors with embedded photogated InAsP quantum discs," *Nanoscale,* vol. 13, no. 12, pp. 6227-6233, 2021.

[47] M. Karimi *et al.*, "Intersubband Quantum Disc-in-Nanowire Photodetectors with Normal-Incidence Response in the Long-Wavelength Infrared," *Nano Letters,* vol. 18, no. 1, pp. 365-372, 2017.

[48] M. Asad, R. Wang, Y.-H. Ra, P. Gavirneni, Z. Mi, and W. S. Wong, "Optically invariant InGaN nanowire light-emitting diodes on flexible substrates under mechanical manipulation," *npj Flexible Electronics,* vol. 3, no. 1, 2019.

[49] H. P. T. Nguyen *et al.*, "Breaking the Carrier Injection Bottleneck of Phosphor-Free Nanowire White Light-Emitting Diodes," *Nano Letters,* vol. 13, no. 11, pp. 5437-5442, 2013.

[50] E. Lai, W. Kim, and P. Yang, "Vertical nanowire array-based light emitting diodes," *Nano Research,* vol. 1, no. 2, pp. 123-128, 2008.

[51] S. Li and A. Waag, "GaN based nanorods for solid state lighting," *Journal of Applied Physics,* vol. 111, no. 7, 2012.

[52] F. Glas, "Critical dimensions for the plastic relaxation of strained axial heterostructures in free-standing nanowires," *Physical Review B,* vol. 74, no. 12, 2006.

[53] E. Ertekin, P. A. Greaney, D. Chrzan, and T. D. Sands, "Equilibrium limits of coherency in strained nanowire heterostructures," *Journal of Applied Physics,* vol. 97, no. 11, 2005.

[54] L. Riuttanen, P. Kivisaari, O. Svensk, J. Oksanen, and S. Suihkonen, "Electrical injection to contactless near-surface InGaN quantum well," *Applied Physics Letters,* vol. 107, no. 5, 2015.

[55] F. Schubert, *Light Emitting Diodes - 4th Ed.* E. Fred Schubert, 2023, p. 592.

[56] H. J. Round, "A note on carborundum," *Electrical World,* vol. 19, p. 309, 1907.

[57] O. V. Losev, "Luminous carborundum [silicon carbide] detector and detection with crystals," *Telegrafiya i Telefoniya bez Provodov,* vol. 44, pp. 485-494, 1927.

[58] Z. Alferov, "Heterostructures for Optoelectronics: History and Modern Trends," *Proceedings of the IEEE,* vol. 101, no. 10, pp. 2176-2182, 2013.

[59] G. Wolff, R. Hebert, and J. Broder, "Electroluminescence of GaP," *Physical Review,* vol. 100, no. 4, p. 1144, 1955.

[60] O. Folberth, "Mischkristallbildung Bei Aiii Bv-Verbindungen," *Zeitschrift für Naturforschung A,* vol. 10, no. 6, pp. 502-503, 1955.

[61] H. Amano, M. Kito, K. Hiramatsu, and I. Akasaki, "P-type conduction in Mg-doped GaN treated with low-energy electron beam irradiation (LEEBI)," *Japanese journal of applied physics,* vol. 28, no. 12A, p. L2112, 1989.

[62] A. I. Zhmakin, "Enhancement of light extraction from light emitting diodes," *Physics Reports,* vol. 498, no. 4-5, pp. 189-241, 2011.

[63] Z. Bi, Z. Chen, F. Danesh, and L. Samuelson, "From nanoLEDs to the realization of RGB-emitting microLEDs," in *Semiconductors and Semimetals*, vol. 106: Elsevier, 2021, pp. 223-251.

[64] Z. Bi, A. Gustafsson, and L. Samuelson, "Bottom-up approaches to microLEDs emitting red, green and blue light based on GaN nanowires and relaxed InGaN platelets," *Chinese Physics B,* vol. 32, no. 1, p. 018103, 2023.

[65] T. Taki and M. Strassburg, "Review—Visible LEDs: More than Efficient Light," *ECS Journal of Solid State Science and Technology,* vol. 9, no. 1, 2019.

[66] S. M. Sze, Y. Li, and K. K. Ng, *Physics of semiconductor devices*. John wiley & sons, 2021.

[67] U. W. Pohl, *Epitaxy of semiconductors*. Springer, 2020.

[68] Y. Peter and M. Cardona, *Fundamentals of semiconductors: physics and materials properties*. Springer Science & Business Media, 2010.

[69] D. Neamen, *Semiconductor physics and devices*. McGraw-Hill, Inc., 2002.

[70] L. N. Quan, J. Kang, C.-Z. Ning, and P. Yang, "Nanowires for photonics," *Chemical reviews,* vol. 119, no. 15, pp. 9153-9169, 2019.

[71] E. M. T. Fadaly *et al.*, "Direct-bandgap emission from hexagonal Ge and SiGe alloys," *Nature,* vol. 580, no. 7802, pp. 205-209, 2020.

[72] P. Kivisaari, J. Oksanen, and J. Tulkki, "Effects of lateral current injection in GaN multi-quantum well light-emitting diodes," *Journal of Applied Physics,* vol. 111, no. 10, 2012.

[73] S. L. Chuang, *Physics of photonic devices*. John Wiley & Sons, 2012.

[74] w. lighting. "SimpleColor™ Green LED Strip Lights." https://store.waveformlighting.com/products/simplecolor-green-led-strip-lights (accessed 10/01/2024).

[75] S. O. Kasap, *Optoelectronics and photonics*. Pearson Education UK, 2013.

[76] S. Nakamura and M. R. Krames, "History of Gallium–Nitride-Based Light-Emitting Diodes for Illumination," *Proceedings of the IEEE,* vol. 101, no. 10, pp. 2211-2220, 2013.

[77] Y. Narukawa, M. Ichikawa, D. Sanga, M. Sano, and T. Mukai, "White light emitting diodes with super-high luminous efficacy," *Journal of physics D: Applied physics,* vol. 43, no. 35, p. 354002, 2010.

[78] H. Ding *et al.*, "Full spectrum core–shell phosphors under ultraviolet excitation," *Chemical Communications,* vol. 55, no. 81, pp. 12188-12191, 2019.

[79] N. M. Ravindra, P. Ganapathy, and J. Choi, "Energy gap–refractive index relations in semiconductors – An overview," *Infrared Physics & Technology,* vol. 50, no. 1, pp. 21-29, 2007.

[80] T. Fujii *et al.*, "Cone-shaped surface GaN-based light-emitting diodes," *physica status solidi (c),* vol. 2, no. 7, pp. 2836-2840, 2005.

[81] C.-S. Wu, T.-C. Liang, H. Kuan, and W.-C. Cheng, "Output power enhancement of GaN-based light-emitting diodes using circular-gear structure," *Japanese Journal of Applied Physics,* vol. 50, no. 3R, p. 032101, 2011.

[82] C.-H. Hsu *et al.*, "Study of GaN-based LEDs with hybrid SiO 2 microsphere/nanosphere antireflection coating as a passivation layer by a rapid convection deposition," *IEEE Transactions on Electron Devices,* vol. 64, no. 3, pp. 1134-1139, 2017.

[83] X.-l. Hu, R.-l. Wen, Z.-y. Qi, and H. Wang, "III-nitride ultraviolet, blue and green LEDs with SiO2 photonic crystals fabricated by UV-nanoimprint lithography," *Materials Science in Semiconductor Processing,* vol. 79, pp. 61-65, 2018.

[84] K. McGroddy *et al.*, "Directional emission control and increased light extraction in GaN photonic crystal light emitting diodes," *Applied physics letters,* vol. 93, no. 10, 2008.

[85] L. Feng, N. Zhang, J. Wang, and J. Li, "Effect of photonic crystals on the light extraction of GaN-based LED for different polarization modes of spontaneous radiation," *Results in Physics,* vol. 15, p. 102632, 2019.

[86] L. Tan, R. Yao, K. Wang, Z. Xie, and H. Wang, "Characteristics of Micro-Size Light-Emitting Diode With Pentagon-Type Structure," *IEEE Photonics Technology Letters,* vol. 33, no. 19, pp. 1077-1080, 2021.

[87] E. Homeyer *et al.*, "Enhanced light extraction from InGaN/GaN quantum wells with silver gratings," *Applied Physics Letters,* vol. 102, no. 8, 2013.

[88] K. Tomioka, K. Sugita, and J. Motohisa, "Enhanced Light Extraction of Nano-Light-Emitting Diodes with Metal-Clad Structure Using Vertical GaAs/GaAsP Core–Multishell Nanowires on Si Platform," *Advanced Photonics Research,* vol. 4, no. 7, 2023.

[89] Q. Zhou, M. Xu, Q. Li, and H. Wang, "Improved efficiency of GaN-based green LED by a nano-micro complex patterned sapphire substrate," *IEEE Photonics Technology Letters,* vol. 29, no. 12, pp. 983-986, 2017.

[90] Y. Zhang *et al.*, "Effects of inclined sidewall structure with bottom metal air cavity on the light extraction efficiency for AlGaN-based deep ultraviolet light-emitting diodes," *IEEE Photonics Journal,* vol. 9, no. 5, pp. 1-9, 2017.

[91] N. Anttu and H. Xu, "Coupling of light into nanowire arrays and subsequent absorption," *Journal of nanoscience and nanotechnology,* vol. 10, no. 11, pp. 7183-7187, 2010.

[92] R. Ding, M. H. An, J. Feng, and H. B. Sun, "Organic Single-Crystalline Semiconductors for Light-Emitting Applications: Recent Advances and Developments," *Laser & Photonics Reviews,* vol. 13, no. 10, 2019.

[93] L. Kinner, T. Dimopoulos, G. Ligorio, E. J. W. List-Kratochvil, and F. Hermerschmidt, "High performance organic light-emitting diodes employing ITO-free and flexible TiOx/Ag/Al:ZnO electrodes," *RSC Advances,* vol. 11, no. 28, pp. 17324-17331, 2021.

[94] R. Pode, "Organic light emitting diode devices: An energy efficient solid state lighting for applications," *Renewable and Sustainable Energy Reviews,* vol. 133, 2020.

[95] K. Alberi, B. Fluegel, M. Steiner, R. France, W. Olavarria, and A. Mascarenhas, "Direct-indirect crossover in GaxIn1-xP alloys," *Journal of Applied Physics,* vol. 110, no. 11, 2011.

[96] J. Wallentin *et al.*, "Single GaInP nanowire p-i-n junctions near the direct to indirect bandgap crossover point," *Applied Physics Letters,* vol. 100, no. 25, 2012.

[97] R. Logan, H. White, and W. Wiegmann, "Efficient Green Electroluminescence in Nitrogen-Doped GaP p-n Junctions," *Applied Physics Letters,* vol. 13, no. 4, pp. 139-141, 1968.

[98] D. Thomas and J. Hopfield, "Isoelectronic traps due to nitrogen in gallium phosphide," *Physical Review,* vol. 150, no. 2, p. 680, 1966.

[99] S. Assali *et al.*, "Direct Band Gap Wurtzite Gallium Phosphide Nanowires," *Nano Letters,* vol. 13, no. 4, pp. 1559-1563, 2013.

[100] A. Berg *et al.*, "Radial Nanowire Light-Emitting Diodes in the (AlxGa1–x)yIn1–yP Material System," *Nano Letters,* vol. 16, no. 1, pp. 656-662, 2015.

[101] H. Chui, N. Gardner, P. Grillot, J. Huang, M. Krames, and S. Maranowski, "High-Efficiency AlGalnP Light-Emitting Diodes," in *Semiconductors and semimetals*, vol. 64: Elsevier, 1999, pp. 49-128.

[102] M. Ochiai-Holcomb *et al.*, "High-power truncated-inverted-pyramid (AlxGa1-x) 0.5 In0. 5P light-emitting diodes," in *Light-Emitting Diodes: Research, Manufacturing, and Applications IV*, 2000, vol. 3938: SPIE, pp. 77-81.

[103] M. Á. Caro Bayo, "Theory of elasticity and electric polarization effects in the group-III nitrides," University College Cork, 2013.

[104] W. Davis and Y. Ohno, "Approaches to color rendering measurement," *Journal of Modern Optics,* vol. 56, no. 13, pp. 1412-1419, 2009.

[105] G. Leschhorn and R. Young, *Handbook of LED and SSL Metrology*. Pro Business, 2017.

[106] I. Kim, P. Kivisaari, J. Oksanen, and S. Suihkonen, "Diffusion-Driven Charge Transport in Light Emitting Devices," *Materials,* vol. 10, no. 12, 2017.

[107] L. Riuttanen, P. Kivisaari, O. Svensk, J. Oksanen, and S. Suihkonen, "Diffusion injection in a buried multiquantum well light-emitting diode structure," *IEEE Transactions on Electron Devices,* vol. 62, no. 3, pp. 902-908, 2015.

[108] H. F. Talbot, "LXXVI. Facts relating to optical science. No. IV," *The London, Edinburgh, and Dublin Philosophical Magazine and Journal of Science,* vol. 9, no. 56, pp. 401-407, 1836.

[109] H. H. Solak, C. Dais, and F. Clube, "Displacement Talbot lithography: a new method for high-resolution patterning of large areas," *Optics express,* vol. 19, no. 11, pp. 10686-10691, 2011.

[110] A. Isoyan *et al.*, "Talbot lithography: Self-imaging of complex structures," *Journal of Vacuum Science & Technology B: Microelectronics and Nanometer Structures Processing, Measurement, and Phenomena,* vol. 27, no. 6, pp. 2931-2937, 2009.

[111] P. J. P. Chausse, E. D. Le Boulbar, S. D. Lis, and P. A. Shields, "Understanding resolution limit of displacement Talbot lithography," *Optics Express,* vol. 27, no. 5, 2019.

[112] V. J. Gómez, M. Graczyk, R. J. Jam, S. Lehmann, and I. Maximov, "Wafer-scale nanofabrication of sub-100 nm arrays by deep-UV displacement Talbot lithography," *Nanotechnology,* vol. 31, no. 29, 2020.

[113] P.-M. Coulon *et al.*, "Displacement Talbot lithography for nano-engineering of III-nitride materials," *Microsystems & Nanoengineering,* vol. 5, no. 1, p. 52, 2019.

[114] K. Kim, J. K. Lee, S. J. Han, and S. Lee, "A Novel Top-Down Fabrication Process for Vertically-Stacked Silicon-Nanowire Array," *Applied Sciences,* vol. 10, no. 3, 2020.

[115] R. S. Wagner and W. C. Ellis, "Vapor-Liquid-Solid Mechanism of Single Crystal Growth," *Applied Physics Letters,* vol. 4, no. 5, pp. 89-90, 1964.

[116] G. Stringfellow, "Fundamental aspects of vapor growth and epitaxy," *Journal of crystal growth,* vol. 115, no. 1-4, pp. 1-11, 1991.

[117] E. P. Bakkers, M. Hocevar, R. E. Algra, L.-F. Feiner, and M. A. Verheijen, "III-Phospide Nanowires," ed: BENTHAM SCIENCE PUBLISHERS, 2012.

[118] H. J. Joyce *et al.*, "III–V semiconductor nanowires for optoelectronic device applications," *Progress in Quantum Electronics,* vol. 35, no. 2-3, pp. 23-75, 2011.

[119] B. A. Wacaser, K. A. Dick, J. Johansson, M. T. Borgström, K. Deppert, and L. Samuelson, "Preferential Interface Nucleation: An Expansion of the VLS Growth Mechanism for Nanowires," *Advanced Materials,* vol. 21, no. 2, pp. 153-165, 2009.

[120] S. Hiscocks and W. Hume-Rothery, "The equilibrium diagram of the system gold-indium," *Proceedings of the Royal Society of London. Series A. Mathematical and Physical Sciences,* vol. 282, no. 1390, pp. 318-330, 1964.

[121] H. Okamoto and T. Massalski, "The Au–P (gold-phosphorus) system," *Bulletin of Alloy Phase Diagrams,* vol. 5, no. 5, pp. 490-491, 1984.

[122] R. E. Algra *et al.*, "Formation of Wurtzite InP Nanowires Explained by Liquid-Ordering," *Nano Letters,* vol. 11, no. 1, pp. 44-48, 2010.

[123] P. Caroff, K. A. Dick, J. Johansson, M. E. Messing, K. Deppert, and L. Samuelson, "Controlled polytypic and twin-plane superlattices in iii–v nanowires," *Nature Nanotechnology,* vol. 4, no. 1, pp. 50-55, 2008.

[124] M. Mattila, T. Hakkarainen, M. Mulot, and H. Lipsanen, "Crystal-structure-dependent photoluminescence from InP nanowires," *Nanotechnology,* vol. 17, no. 6, p. 1580, 2006.

[125] S. Assali *et al.*, "Optical study of the band structure of wurtzite GaP nanowires," *Journal of Applied Physics,* vol. 120, no. 4, 2016.

[126] L. Gagliano *et al.*, "Pseudodirect to Direct Compositional Crossover in Wurtzite GaP/In x Ga1–x P Core–Shell Nanowires," *Nano letters,* vol. 16, no. 12, pp. 7930-7936, 2016.

[127] J. Wallentin, M. Ek, L. R. Wallenberg, L. Samuelson, K. Deppert, and M. T. Borgström, "Changes in Contact Angle of Seed Particle Correlated with Increased Zincblende Formation in Doped InP Nanowires," *Nano Letters,* vol. 10, no. 12, pp. 4807-4812, 2010.

[128] A. J. Bard, L. R. Faulkner, and H. S. White, *Electrochemical methods: fundamentals and applications*. John Wiley & Sons, 2022.

[129] C. A. Loto, "Electroless Nickel Plating – A Review," *Silicon,* vol. 8, no. 2, pp. 177-186, 2016.

[130] P. Sahoo and S. K. Das, "Tribology of electroless nickel coatings–a review," *Materials & Design,* vol. 32, no. 4, pp. 1760-1775, 2011.

[131] K. Chinchu, A. Riyas, M. A. Sha, C. Geethanjali, V. S. Saji, and S. Shibli, "ZrO2–CeO2 assimilated electroless Ni–P anti-corrosion coatings," *Surfaces and Interfaces,* vol. 21, p. 100704, 2020.

[132] Y. Okinaka and M. Hoshino, "Some recent topics in gold plating for electronics applications," *Gold Bulletin,* vol. 31, pp. 3-13, 1998.

[133] A. Wurtz, "On copper hydride (Translated from French)," *Cr Hebd Acad Sci,* vol. 18, pp. 702-704, 1844.

[134] A. Brenner and G. E. Riddell, "Nickel plating on steel by chemical reduction," *Journal of research of the National Bureau of Standards,* vol. 37, no. 1, p. 31, 1946.

[135] S. Djokić, *Fundamentals of electroless deposition* (Encyclopedia of interfacial chemistry: surface science and electrochemistry). 2018, pp. 161-173.

[136] V. G. Weizer and N. S. Fatemi, "The interaction of gold with gallium arsenide," *Journal of Applied Physics,* vol. 64, no. 9, pp. 4618-4623, 1988.

[137] E. Ruiz-Gomes *et al.*, "Electroless selective deposition of gold nano-array for silicon nanowires growth," *Nanofabrication,* vol. 1, no. 2014, pp. 1-7, 2013.

[138] L. Magagnin, R. Maboudian, and C. Carraro, "Gold deposition by galvanic displacement on semiconductor surfaces: effect of substrate on adhesion," *The Journal of Physical Chemistry B,* vol. 106, no. 2, pp. 401-407, 2002.

[139] S. Y. Sayed, B. Daly, and J. M. Buriak, "Characterization of the interface of gold and silver nanostructures on InP and GaAs synthesized via galvanic displacement," *The Journal of Physical Chemistry C,* vol. 112, no. 32, pp. 12291-12298, 2008.

[140] N. Takano, N. Hosoda, T. Yamada, and T. Osaka, "Mechanism of the chemical deposition of nickel on silicon wafers in aqueous solution," *Journal of the Electrochemical Society,* vol. 146, no. 4, p. 1407, 1999.

[141] J. G. A. Brito-Neto, S. Araki, and M. Hayase, "Synthesis and characterization of porous platinum layers deposited on highly doped n-type porous silicon by immersion plating," *Journal of The Electrochemical Society,* vol. 153, no. 11, p. C741, 2006.

[142] R. Zhang, M. Hummelgård, and H. Olin, "Simple and efficient gold nanoparticles deposition on carbon nanotubes with controllable particle sizes," *Materials Science and Engineering: B,* vol. 158, no. 1-3, pp. 48-52, 2009.

[143] S. Wang, K. Qian, X. Bi, and W. Huang, "Influence of speciation of aqueous HAuCl4 on the synthesis, structure, and property of Au colloids," *The Journal of Physical Chemistry C,* vol. 113, no. 16, pp. 6505-6510, 2009.

[144] Y. Shacham-Diamand, T. Osaka, Y. Okinaka, A. Sugiyama, and V. Dubin, "30 years of electroless plating for semiconductor and polymer micro-systems," *Microelectronic Engineering,* vol. 132, pp. 35-45, 2015.

[145] M. Cerruti, G. Doerk, G. Hernandez, C. Carraro, and R. Maboudian, "Galvanic Deposition of Pt Clusters on Silicon: Effect of HF Concentration and Application as Catalyst for Silicon Nanowire Growth," *Langmuir,* vol. 26, no. 1, pp. 432-437, 2009.

[146] L. A. Nagahara, T. Ohmori, K. Hashimoto, and A. Fujishima, "Effects of HF solution in the electroless deposition process on silicon surfaces," *Journal of Vacuum Science & Technology A: Vacuum, Surfaces, and Films,* vol. 11, no. 4, pp. 763-767, 1993.

[147] K. A. Dick, K. Deppert, M. W. Larsson, W. Seifert, L. R. Wallenberg, and L. Samuelson, "Height-controlled nanowire branches on nanotrees using a polymer mask," *Nanotechnology,* vol. 18, no. 3, 2007.

[148] K. A. Dick *et al.*, "Synthesis of branched 'nanotrees' by controlled seeding of multiple branching events," *Nature Materials,* vol. 3, no. 6, pp. 380-384, 2004.

[149] K. Bayer, K. A. Dick, T. J. Krinke, and K. Deppert, "Targeted deposition of Au aerosol nanoparticles on vertical nanowires for the creation of nanotrees," *Journal of Nanoparticle Research,* vol. 9, no. 6, pp. 1211-1216, 2007.

[150] T. J. Krinke, K. Deppert, M. H. Magnusson, F. Schmidt, and H. Fissan, "Microscopic aspects of the deposition of nanoparticles from the gas phase," *Journal of Aerosol Science,* vol. 33, no. 10, pp. 1341-1359, 2002.

[151] M. R. Hormozi Nezhad, M. Aizawa, L. A. Porter, A. E. Ribbe, and J. M. Buriak, "Synthesis and Patterning of Gold Nanostructures on InP and GaAs via Galvanic Displacement," *Small,* vol. 1, no. 11, pp. 1076-1081, 2005.

[152] P. L. Redmond, A. J. Hallock, and L. E. Brus, "Electrochemical Ostwald ripening of colloidal Ag particles on conductive substrates," *Nano letters,* vol. 5, no. 1, pp. 131-135, 2005.

[153] C. Carraro, R. Maboudian, and L. Magagnin, "Metallization and nanostructuring of semiconductor surfaces by galvanic displacement processes," *Surface Science Reports,* vol. 62, no. 12, pp. 499-525, 2007.

[154] Y. Zhang, Y. Chen, L. Hrachowina, C. Sundvall, I. Åberg, and M. Borgström, "UV exposure: a novel processing method to fabricate nanowire solar cells," in *2019 IEEE 46th Photovoltaic Specialists Conference (PVSC),* 2019: IEEE, pp. 2646-2648.

[155] K. Dick, K. Deppert, L. Karlsson, L. Wallenberg, L. Samuelson, and W. Seifert, "Role of the Au/III-V interaction in the Au-assisted growth of III-V branched nanostructures," in *International Conference on Indium Phosphide and Related Materials, 2005*, 2005: IEEE, pp. 487-490.

[156] L. S. Karlsson *et al.*, "Crystal structure of branched epitaxial III–V nanotrees," *Nano,* vol. 1, no. 02, pp. 139-151, 2006.

[157] V. Schmidt, S. Senz, and U. Gösele, "Diameter-dependent growth direction of epitaxial silicon nanowires," *Nano letters,* vol. 5, no. 5, pp. 931-935, 2005.

[158] M. T. Borgström *et al.*, "In situ etching for total control over axial and radial nanowire growth," *Nano Research,* vol. 3, no. 4, pp. 264-270, 2010.

[159] A. A. Zakharov *et al.*, "Manipulating the dynamics of self-propelled gallium droplets by gold nanoparticles and nanoscale surface morphology," *ACS nano,* vol. 9, no. 5, pp. 5422-5431, 2015.

[160] A. Mikkelsen, J. Eriksson, E. Lundgren, J. N. Andersen, J. Weissenreider, and W. Seifert, "The influence of lysine on InP(001) surface ordering and nanowire growth," *Nanotechnology,* vol. 16, no. 10, pp. 2354-2359, 2005.

[161] U. Krishnamachari *et al.*, "Defect-free InP nanowires grown in [001] direction on InP (001)," *Applied Physics Letters,* vol. 85, no. 11, pp. 2077-2079, 2004.

[162] K. A. Dick *et al.*, "The morphology of axial and branched nanowire heterostructures," *Nano letters,* vol. 7, no. 6, pp. 1817-1822, 2007.

[163] J. Wallentin and M. T. Borgström, "Doping of semiconductor nanowires," *Journal of Materials Research,* vol. 26, no. 17, pp. 2142-2156, 2011.

[164] D. Hausmann, J. Becker, S. Wang, and R. G. Gordon, "Rapid vapor deposition of highly conformal silica nanolaminates," *Science,* vol. 298, no. 5592, pp. 402-406, 2002.

[165] L. Hrachowina *et al.*, "Imaging the influence of oxides on the electrostatic potential of photovoltaic InP nanowires," *Nano Research,* vol. 14, no. 11, pp. 4087-4092, 2021.

[166] W. Zhang *et al.*, "Carrier Recombination Processes in Gallium Indium Phosphide Nanowires," *Nano Letters,* vol. 17, no. 7, pp. 4248-4254, 2017.

[167] D. Lindgren *et al.*, "Study of carrier concentration in single InP nanowires by luminescence and Hall measurements," *Nanotechnology,* vol. 26, no. 4, p. 045705, Jan 30 2015, doi: 10.1088/0957-4484/26/4/045705.

[168] ThorLabs. "4P3 - Ø100 mm Integrating Sphere with 3 Modular Faces, Light Measurement Configuration." https://www.thorlabs.com/thorproduct.cfm?partnumber=4P3 (accessed 03/03/2024).

[169] G. Optik. "Light Measurement." https://light-measurement.com/tutorials-on-light-measurement/tutorials.pdf (accessed 03/03/2024).

[170] K. Carr, "Integrating sphere theory and applications Part I: Integrating sphere theory and design," *Surface coatings international,* vol. 80, no. 8, pp. 380-385, 1997.

[171] G. Verzellesi *et al.*, "Efficiency droop in InGaN/GaN blue light-emitting diodes: Physical mechanisms and remedies," *Journal of Applied Physics,* vol. 114, no. 7, 2013.

[172] P. Tian *et al.*, "Temperature-dependent efficiency droop of blue InGaN micro-light emitting diodes," *Applied Physics Letters,* vol. 105, no. 17, 2014.

[173] A. Pandey *et al.*, "A red-emitting micrometer scale LED with external quantum efficiency> 8%," *Applied Physics Letters,* vol. 122, no. 15, 2023.

[174] Y. H. Ra and C. R. Lee, "Monolithic Light Reflector-Nanowire Light Emitting Diodes," *Advanced Materials Technologies,* vol. 6, no. 2, 2021.

[175] E. L. Hsiang, Z. Yang, Q. Yang, Y. F. Lan, and S. T. Wu, "Prospects and challenges of mini-LED, OLED, and micro-LED displays," *Journal of the Society for Information Display,* vol. 29, no. 6, pp. 446-465, 2021.

[176] E. Archer *et al.*, "Accurate Efficiency Measurements of Organic Light-Emitting Diodes via Angle-Resolved Spectroscopy," *Advanced Optical Materials,* vol. 9, no. 1, 2020.

[177] J. Shin *et al.*, "Vertical full-colour micro-LEDs via 2D materials-based layer transfer," *Nature,* vol. 614, no. 7946, pp. 81-87, 2023.

[178] Y.-H. Ra and C.-R. Lee, "Core–shell tunnel junction nanowire white-light-emitting diode," *Nano Letters,* vol. 20, no. 6, pp. 4162-4168, 2020.

[179] Z. Zhuang, D. Iida, M. Velazquez-Rizo, and K. Ohkawa, "630-nm red InGaN micro-light-emitting diodes (< 20 µm× 20 µm) exceeding 1 mW/mm 2 for full-color micro-displays," *Photonics Research,* vol. 9, no. 9, pp. 1796-1802, 2021.

[180] Z. Liu *et al.*, "Micro-light-emitting diodes with quantum dots in display technology," *Light: Science & Applications,* vol. 9, no. 1, 2020.

Printed by Media-Tryck, Lund 2024 NORDIC SWAN ECOLABEL 3041 0903

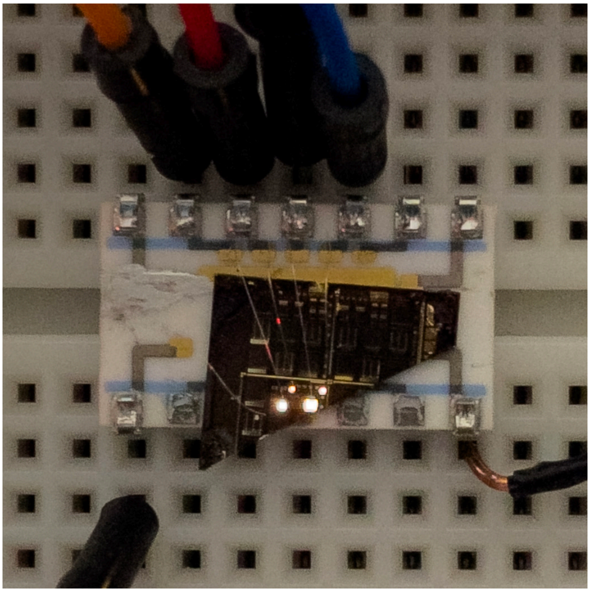

This thesis describes the development of novel light emitting diodes comprising thousands of vertically standing nanotrees and their subsequent characterisation. The photograph above demonstrates four devices with different active region areas connected in parallel and emitting bright white light.

Division of Solid State Physics
Department of Physics
Faculty of Engineering
Lund university
ISBN 978-91-8039-968-5